Additive Manufacturing of Fuel Injectors

Final Technical Report

Reporting Period: November 2014 – October 2017

Principal Authors: Dr. Alber Sadek, Dr. George Ritter, Charles Drews, Daniel Ryan (Solar Turbines)

Date Issued: October 2017

DOE Award No.: DE-FE0023974

EWI Project No. 55232GTH

Submitted by: EWI, 1250 Arthur E. Adams Drive, Columbus, OH 43221

DISCLAIMER

This report was prepared as an account of work sponsored by an agency of the United States Government. Neither the United States Government nor any agency thereof, nor any of their employees, makes any warranty, express or implied, or assumes any legal liability or responsibility for the accuracy, completeness, or usefulness of any information, apparatus, product, or process disclosed, or represents that its use would not infringe privately owned rights. Reference herein to any specific commercial product, process, or service by trade name, trademark, manufacturer, or otherwise does not necessarily constitute or imply its endorsement, recommendation, or favoring by the United States Government or any agency thereof. The views and opinions of authors expressed herein do not necessarily state or reflect those of the United States Government or any agency thereof.

Abstract

Additive manufacturing (AM), also known as 3D-printing, has been shifting from a novelty prototyping paradigm to a legitimate manufacturing tool capable of creating components for highly complex engineered products. An emerging AM technology for producing metal parts is the laser powder bed fusion (L-PBF) process; however, industry manufacturing specifications and component design practices for L-PBF have not yet been established. Solar Turbines Incorporated (Solar), an industrial gas turbine manufacturer, has been evaluating AM technology for development and production applications with the desire to enable accelerated product development cycle times, overall turbine efficiency improvements, and supply chain flexibility relative to conventional manufacturing processes (casting, brazing, welding).

Accordingly, Solar teamed with EWI on a joint two-and-a-half-year project with the goal of developing a production L-PBF AM process capable of consistently producing high-nickel alloy material suitable for high temperature gas turbine engine fuel injector components. The project plan tasks were designed to understand the interaction of the process variables and their combined impact on the resultant AM material quality.

The composition of the high-nickel alloy powders selected for this program met the conventional cast Hastelloy X compositional limits and were commercially available in different particle size distributions (PSD) from two suppliers. Solar produced all the test articles and both EWI and Solar shared responsibility for analyzing them. The effects of powder metal input stock, laser parameters, heat treatments, and post-finishing methods were evaluated. This process knowledge was then used to generate tensile, fatigue, and creep material properties data curves suitable for component design activities. The key process controls for ensuring consistent material properties were documented in AM powder and process specifications. The basic components of the project were:

- Powder metal input stock: Powder characterization, dimensional accuracy, metallurgical characterization, and mechanical properties evaluation.
- Process parameters: Laser parameter effects, post-printing heat-treatment development, mechanical properties evaluation, and post-finishing technique.
- Material design curves: Room and elevated temperature tensiles, low cycle fatigue, and creep rupture properties curves generated.
- AM specifications: Key metal powder characteristics, laser parameters, and heat-treatment controls identified.

Table of Contents

Page

List of Tables

List of Figures

Abbreviated Terms

2D	two-dimensional
3D	three-dimensional
AFM	abrasive flow machining
AM	additive manufacturing
CCT	continuous cooling transformation
CIP'ing	cold isostatic processing
CMM	coordinate measuring machine
CT	computed tomography
DOE	Design of Experiments
EB	electron beam
ECT	equi-cohesive temperature
EDM	electrical discharge machining
EDS	energy-dispersive x-ray spectroscopy
HCF	high cycle fatigue
HIP'ing	host isostatic processing
HT	heat treatment
J	Joules
LCF	low cycle fatigue
LOF	lack of fusion
L-PBF	laser powder bed fusion
MMP	micro-machining process
NIST	National Institute of Standards and Technology
PMC	polymer matric composites
PSD	particle-sized distribution
Ra	2D arithmetic mean height
RA	reduction in area
RT	radiographic testing
S1	Supplier 1

S1-C	S1-coarse
S1-F	S1-fine
S1-F(P)	NIST test artifact with s2-f powder before removal from plate
S2	Supplier 2
S2-C	S2-coarse
S2-F	S2-fine
Sa	3D arithmetic mean height
SEM	scanning electron microscope
TCP	topologically close packed
UTS	ultimate tensile strength
UV	ultraviolet
XRD	x-ray diffraction
YS	yield strength

Executive Summary

Solar teamed with EWI on a joint two-and-a-half-year project with the goal of developing a production laser powder bed fusion (L-PBF) additive manufacturing (AM) process capable of consistently producing AM material suitable for high-temperature gas turbine engine components. Throughout the execution of the four following project tasks, key AM process risks were identified and corresponding process solutions were developed.

1. Powder Metal Input Stock: A powder particle size distribution (PSD) and powder chemistry were identified which are compatible with the 3D printer and capable of producing sound material.
2. Process Parameters: A heat treatment process was identified which resulted in improved ductility and fatigue performance of the AM material.
3. Material Design Curves: Material properties curves were generated that will enable designers to assess durability and performance of AM component designs.
4. AM Specifications: Key process controls for ensuring consistent material properties were specified.

The process and properties knowledge gained through this project have played a significant role in Solar's journey from the AM prototyping paradigm to AM component serial production. Implementation of the process controls identified in this project have contributed to Solar's capability to produce high quality AM material for high temperature gas turbine components.

1.0 Introduction

Solar teamed with EWI to gain a better understanding of the different variables unique to L-PBF AM processing. The goal was to understand the interaction of the process variables and their combined impact on the quality of the finished part. Variables studied included the powder size and supplier, L-PBF processing parameters, heat treatment methods, and post-finishing methods. The main objective was to find the optimum combination to yield the best quality parts based on a target application of fuel injectors in turbines.

Evolving AM technology is now at the point where some turbine components can be additively manufactured for both development and production purposes. Any new application requires an evaluation program to qualify the process and the components to ensure they meet current quality and design standards for parts produced conventionally. In this case, the incumbent parts are produced using casting and machining operations.

Solar was specifically interested in producing components using high-nickel alloys. This report covers work done over a three-year period specific to the development of fuel injectors.

1.1 Additive Manufacturing

AM, also known as 3D-printing, has rapidly grown from a novelty to a legitimate manufacturing tool that is being used to produce production parts daily. The earliest AM techniques originated in the 1980s using polymers and ultraviolet (UV) light to produce conceptual models of parts that would then be produced in quantity by conventional means. Within the last fifteen years, AM processes have matured to being readily adaptable methods for genuine production.

A principal advantage to AM techniques is they enable new designs and the ability to produce components that are too difficult or impossible to produce otherwise. They may contain hidden features or channels. The design may call for complex curves that are difficult to machine or cast at reasonable cost.

AM parallels traditional polymer matrix composites (PMC) development in several ways. Like PMC, AM methods produce the material as the part is produced. In the case of AM, there are no molds – the part is produced as a free-standing entity. Like PMCs, AM parts are prone to porosity and variable density, depending on location within the part. Consequently, frequent post-processing is required in the forms of heat treatments, hot isostatic pressing (HIP'ing), and possibly cold isostatic pressing (CIP'ing). Post-finishing is often required to remove "flash" or loose materials. However, the most consistent similarity to PMCs is AM parts often show directional anisotropy in performance and material properties. This requires attention in the

manufacturing process to ensure the parts will have the required performance along the necessary load paths and that these properties are reproducible, part to part.

1.2 Laser Powder Bed Fusion

There are many AM processes available and selection depends on the materials being processed. A popular method for producing metal parts from powders is L- PBF. Closely allied is another process based on using electron beam (EB) equipment. In the L-PBF process, a layer of powder is uniformly deposited onto a work bed. A laser beam is then directed in patterns onto the bed of powder to weld/fuse the particles together. Another layer of powder is deposited and the process repeats. The added thickness of each layer depends on the particle size distribution of the powder and on the settings of the deposition squeegee.

It is possible to produce several parts at once by having replicates scanned into the bed. Typically, these are small parts. One large part might be produced. Work beds are now ranging into multiple cubic feet of produced material. While it may take days to produce parts, these are parts that might take weeks or months to produce using traditional preforming and subtractive methods, if they can be produced conventionally at all. There is also the opportunity for parts consolidation that reduces machining time and joining complexity. When the fabrication is complete, the parts are harvested from the surrounding unused powder.

L-PBF requires no molds and enables inclusion of outcroppings, overhangs, internal channels, bosses, depressions, and other features that are created as the scanned design is implemented. Thus, it is possible to produce very complex structures as monoliths and in multiple replicates. There are now many alloy powders on the market for aluminum, titanium, nickel-based, and other metals. Because of the versatility of the materials-process combinations, it is possible to design parts for AM production that were unthinkable in terms of materials or design even five years ago. Today, most AM parts are designed specifically to take advantage of the method(s), without resorting to a copy-cat mentality for parts that can be produced traditionally. The exception to that is if the AM parts can be produced at lower cost or better quality than the traditional ones.

The laser equipment is typically based on fiber or YAG lasers operating at about 1060 or 1064 nm, respectively. Power levels are in the 200-1000 W range, which is adequate for fast scanning of the powder beds. Scan rates upwards of 5000 mm/s are attainable. The exposed powders are blanketed under argon, since the presence of air would result in oxidation during the welding/fusion processing. Processing is completely computer-controlled and industrial-scale production is run using multiple machines, operating simultaneously in AM “farms”.

1.3 Relevance and Impact for This Program

Solar has been evaluating AM printers for the development and production of industrial gas turbine components. Some of these components have historically been investment cast and then machined, a process that is expensive and time consuming. In addition, many of these components are subject to very high temperatures and stresses during operation, requiring high performance alloys to be used that can be difficult to cast and machine. These components may also have complex geometries that make it challenging to cast and meet the design and dimensional requirements.

1.3.1 Current Status

Solar is currently considering the L-PBF AM process for select turbine components. They recently had two fuel injector parts made on two separate L-PBF AM machines with reasonable results. The quality of the parts was promising, but occurrences of porosity, micro-cracking, voids, and lack of fusion remain a concern. There were also concerns with the surface finish. These AM development parts were made with Alloy X powder that is a high-nickel alloy similar to Hastelloy X.

Solar's business has grown over the last 20 years with primary markets in industrial power generation and oil & gas. Solar is in a unique situation where 100 percent of new gas turbine products are assembled in the U.S. and as much as three-quarters of the units are shipped outside the U.S.

Solar is currently the world's largest producer of industrial gas turbines from 1 to 25 MW. However, there is stiff foreign competition from Japanese and German turbine manufacturers that are also developing high performance and low-cost products. Solar continues to look for innovative ways to increase production output with minimal capital investment while meeting customers' cost, performance, and delivery time requirements. AM is an innovative solution that can help achieve these goals, keep Solar's business growing, and create jobs in the U.S.

Solar is focusing on two specific areas to improve with AM. First is in improving the product development process and second is in improving production costs, lead times, and quality.

1.3.2 Potential for Future Product Development

Solar has been an innovative manufacturer of industrial gas turbines for over 60 years. Major new product engine programs can take up to five years with development costs exceeding $100M. Several of the higher technology risk components like fuel injectors and turbine airfoils can take years to design and to produce with traditional design and manufacturing processes.

If not designed or manufactured properly, there can be significant delays in the product development and introduction.

Solar spends significant resources and funds during the development process to ensure the design is correct. AM has the potential to play a vital role in reducing procurement time and costs allowing the engineers more time to iterate and evaluate the design. This in turn can lead to reduced product development lead times, lower development costs, and getting the product to market faster. It also could reduce the risk of quality or product issues during commercialization.

1.3.3 Technical Barriers and Plans for Commercial Production

Additive manufacturing is a viable alternative to investment casting. A computer-aided design (CAD) file is used to print parts with good initial reproducibility. However, L-PBF-specific heat treatment and finishing requirements need to be developed. Material property databases are not readily available for the high temperature materials used in gas turbines. In addition, an AM process needs to be developed based on the material, design, and application.

This project focused on understanding the variables in the L-BPF process and their impact on material properties. These, along with the dimensional and AM material quality, need to be defined to take the next step toward commercial production. Solar estimates that changing from the current casting and assembly process to an AM process could save nearly $1M in product cost annually for the fuel injector tip component alone.

1.4 Program Definition and Content

The conceptual pathway to the finished commercial component is shown in Figure 1.

Fuel Injector Component Model 3D Systems Printer Finished Fuel Injector Component

Figure 1. AM Conceptual Path to Component

The chosen alloy for this program is similar in composition to Hastelloy X and is commercially available in different particle size distributions from two suppliers, designated as Supplier1 (S1) and Supplier2 (S2). Solar and EWI created the design and Solar produced all the test articles. Both organizations shared responsibility for analyzing the test articles. The overarching goals were to define the materials and processing specifications necessary to produce the parts. The basic components of the study were:

- Select and characterize powders from two sources.
- Characterize their LBP-F processibility.
- Analyze the components for porosity, dimensional accuracy, compositional accuracy, and mechanical performance.
- Define post-processing consolidation techniques.
- Evaluate post-finishing techniques for surface uniformity and surface finish compared with the incumbent production methods.
- Develop specifications for the powder and processing to produce fuel injectors.

1.4.1 Objectives

The overall objective of the work was to develop and qualify the mechanical performance of Alloy X fuel injectors made using L-PBF. Based on preliminary work, effort was necessary in developing the required microstructure and properties for the alloy, as well as the required dimensional and surface finish requirements for the component. Objectives by task are described in the following paragraphs.

1.4.1.1 Task 1.0 – Project Management and Planning

The objective of Task1 was to ensure suitable contingencies for resource availability, both in terms of human and equipment resources, to meet technical and financial milestones.

1.4.1.2 Task 2.0 – Powder Sensitivity

The objective of the work regarding powder sensitivity was to determine the effect of powder fines on surface finish, dimensional accuracy, and material properties.

1.4.1.3 Task 3.0 – Component Geometry and Surface Finish

The objective of the work on component geometry and surface finish was to examine the effect of L-PBF build parameters on the final build geometry and to quantify surface finish in different

areas of the build. This process would define what can be built and used in the as-built geometry and which features need subsequent post-build finishing.

Experience has shown that for efficient development, the post-build heat treatment needs to be optimized early in the process, so the additional objective of this task was to optimize this thermal cycle. The primary objective was to improve ductility of the material produced using L-PBF processing and post-process finishing.

1.4.1.4 Task 4.0 – Material Properties

The objective of the work on materials properties was to provide quantitative data on tensile, creep, and low-cycle fatigue (LCF) for the material built on the L-PBF machine. This data could then be compared to design requirements against the current cast part. All these results were measured at temperatures up to 1500°F to provide fundamental information on component life at temperature.

1.4.1.5 Task 5.0 – Specifications

The objective of the work on specifications was to develop and provide specifications governing the powder, the process, and the material involved in the production of components. The goal was to allow sufficient control to deliver the required quality of the components in a manufacturing context.

1.4.2 Scope of Work and Tasks

Solar recently purchased a 3D Systems (formerly Phenix) L-PBF AM machine with the plan to start manufacturing production hardware within a year of purchase. However, they have limited experience with AM of specific high-temperature gas turbine components.

Gas turbine components require very specific design and material considerations. Dimensional tolerances need to be met, along with the material and metallurgical properties. These components operate in very high temperature and stress environments, so the margin for design and manufacturing error is very narrow. Most industrial gas turbine components need to last over 60,000 hours before replacement. This makes them unique to other turbine components currently being additively manufactured, specifically in aero turbines.

Solar and EWI evaluated the impact of several variables for the AM of a fuel injector component. These variables included evaluating different types of powder material from various suppliers, developing AM parameters, heat-treat sensitivity, and post-process finishing.

Solar and EWI evaluated several materials and chose Alloy X as the baseline material. Solar wanted to develop material properties and attendant design curves. This section provides a summary of the approach to this project.

1.4.2.1 Task 1.0 – Project Management and Planning

Management teams were implemented both at EWI and at Solar. Resourcing and staffing were arranged.

1.4.2.2 Task 2.0 – Powder Sensitivity

This task defined the impacts of powder particle size on part quality. Powder used for preliminary work with 3D Systems has a high occurrence of very fine particles (~1 to 10 µm), causing the powder to have less than desirable handling characteristics. This has implications for both machine operation reliability and build quality. Small satellite particles increase the surface area to volume ratio and thus, the oxygen content of the powder. Increased oxygen content is known to affect material properties, with potential for reduced ductility and fatigue properties and/or increased strength. The presence of small particles affects powder layer packing characteristics and thus, may affect laser melting characteristics. This can result in increased potential for porosity and cracking. Finally, small particles add an additional scale of surface roughness that must be addressed during finishing.

This task evaluated the effect of removal of fine particles from the powder used in the 3D Systems ProX 300 L-PBF process, using equipment at Solar. (Both suppliers could provide the requested materials.) Experiments were designed by EWI and executed at Solar. EWI made suitable visits to Solar for performance and discussion of technical scope and L-PBF builds. Effects on dimensional capability, material defects, and mechanical properties (mostly through tensile testing) have been evaluated.

The development work was conducted using trial builds of the National Institute of Standards and Technology (NIST) test artifact (Figure 2). These build trials were used to determine the effect on porosity, surface finish, dimensional accuracy, and tensile material properties. Also, quantitative chemical analysis of each powder and AM sample was performed. The data produced have been used to generate powder specifications to control powder particle size and composition.

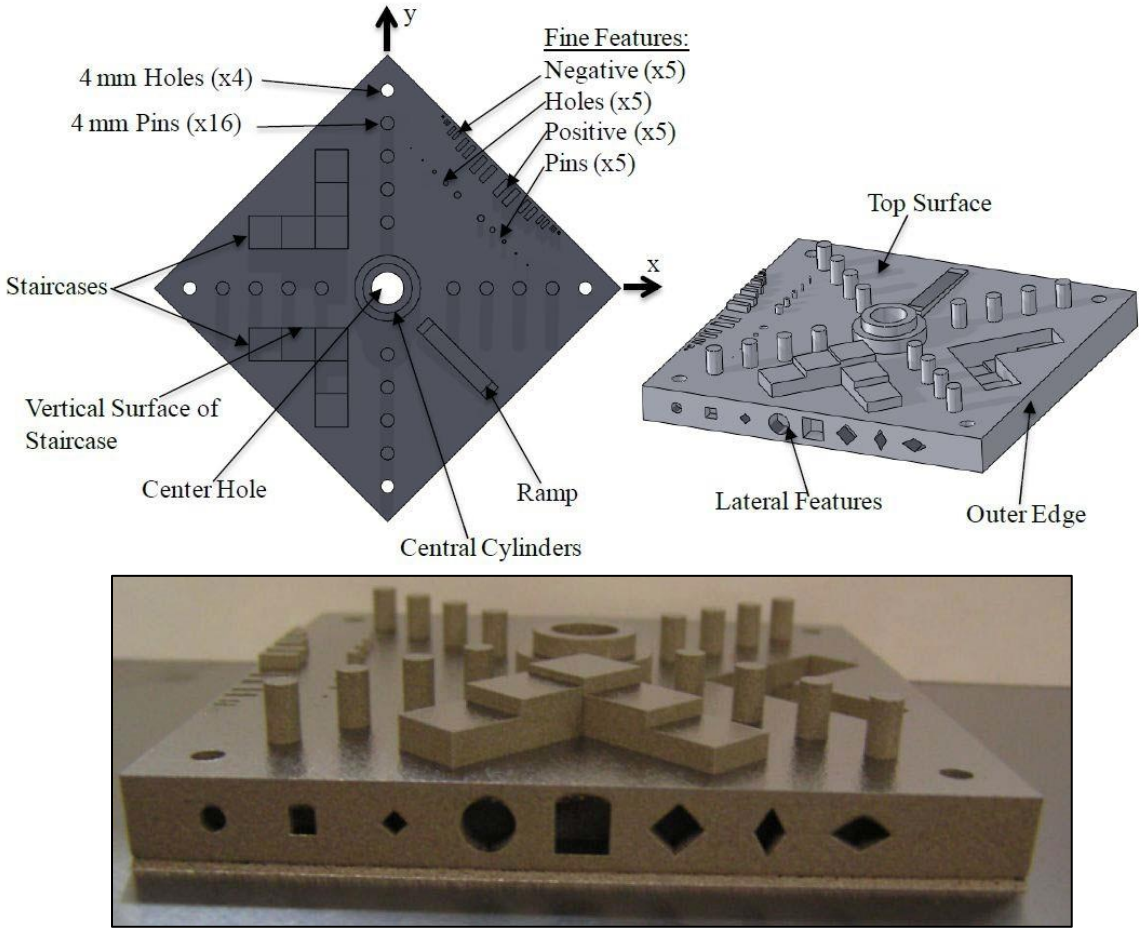

Figure 2. NIST Test Article for AM Build Geometry Assessment

1.4.2.3 Task 3.0 – Component Geometry and Surface Finish

The results from Task 2.0 were used to down select a preferred powder size range and samples from two vendors. These powders were used in Task 3.0 to examine the effects on component geometry and surface finish. This task included quantitative examination of the effects of post processing to improve surface finish.

1.4.2.3.1 Subtask 3.1 – Geometry, Modeling, and Parameter Development. Preliminary work had shown that the surface finish of AM-built parts is rougher than that of castings. The orientation of the various faces has a direct impact on surface finish with downward facing surfaces showing increased roughness compared to upward facing surfaces. The complex injector design has many surfaces in numerous orientations relative to the build orientation.

JMatPro was used to predict carbide fraction versus temperature and the continuous cooling transformation (CCT) curves of Hastelloy X. Based on this information, the proper post-build

heat treatment parameters, including heating rate, temperature, and cooling rate, were selected to achieve the optimal material properties. Heat treatment optimization was used to increase grain size and optimize carbide distribution for elevated temperature service.

Build parameters were combined with effects of part orientation relative to the build axes, the effect of support structure, and the scanning parameters of the laser.

1.4.2.3.2 Subtask 3.2 – Post Processing. Post processing involves both the optimization of heat treatment (grain size, carbides) and the use of finishing technologies to achieve the required surface finish on the components. Results from JMatPRO were used to suggest heat treatment trials to optimize mechanical properties, especially ductility. Six post-processing finishing techniques were examined to quantitatively rate their respective effects on improving the surface finish of as-built components.

1.4.2.4 Task 4.0 – Material Properties

In Task 4.0, materials properties were quantified. Mechanical tests for tensile, creep, and LCF were collected for the materials built on the L-PBF machine. The preferred material properties ultimately were derived from all aspects of the powder, material, and processing used in the build and the critical selection of optimized post-build thermal treatment. Emphasis was placed on the undesirability of low ductility stemming from the combination of powder type and processing. Ductility is a major factor in part lifetime and reliability. Other important considerations were the orientation effect (vertical/horizontal), support structure effect, geometry effect (thick/thin sections), and laser scan parameter sensitivity.

1.4.2.5 Task 5.0 – Specifications

The work developed and provided specifications governing the powder, the process, and the material involved in the production of components, such that these can be controlled sufficiently to deliver the required quality of the components in a manufacturing context. Input powder quality, morphology, production process route, and particle size range have a very important impact on the quality of the final part built during the AM process. Both the process used and the material produced have been described and controlled to produce a consistent outcome in a manufacturing context. The degree of interconnectivity between the process and the material produced is such that a combined material and process specification has been established.

1.5 Deliverables

1.5.1 Task 1.0 –Project Management and Planning

Deliverables: Provide staffing at both EWI and Solar. The periodic, topical, and final reports were prepared and submitted in accordance with “Federal Assistance Reporting Checklist”.

1.5.2 Task 2.0 – Powder Sensitivity

Deliverables: CMM data from measurement of NIST Test Artifact builds.

1.5.3 Task 3.0 – Component Geometry and Surface Finish

Deliverables: Optimized post-processing heat-treatment parameters, L-PBF parameters for builds in Task 4.0. Selection of optimized process parameters for post-processing finishing.

1.5.4 Task 4.0 – Material Properties

Deliverables: The results of the testing for tensile creep and low cycle fatigue.

1.5.5 Task 5.0 – Specifications

Deliverables: Develop and provide specifications for powder and processing based on the work above.

2.0 Experimental

There were five major components to the experimental workflow. Throughout the program, these components were used iteratively with a goal of continuous improvement. The types of experimentation described below are indicative of the overall approach. The experimental approach was:

- Selection and characterization of powders.
- Development of process parameters for each powder.
- Production of test specimens.
- Characterization of test specimens for dimensional accuracy, microstructure, and mechanical performance at room temperature and elevated temperatures:
  - Tensile, yield, elongation, reduction of area
  - Creep
  - LCF.
- Development of heat treat procedures.
- Development of final cleaning and machining processes.

2.1 Characterization of Powders

Hastelloy-type, high-nickel powders were the target materials for development of the fuel injector component. S1 and S2 were identified as potential suppliers. They provided powders having both “fine” and “coarse” particle distribution. The nominal information on these powders is given in Table 1 below.

Table 1. Updated Powder Cost Matrix

Vendor	Powder Type	Min. Desired Size (µm)	Max. Desired Size (µm)	Fine (%)	Coarse (%)	Cost Comparison per lb (350 lb order)
S1	Fine	5	38	0.1% < 5 um	0.8% > 38 um	132%
	Coarse	20	45	4.2% < 20 um	0.5% > 45 um	100%
S2	Fine	5	38	2% < 5.5 um	1 > 38 um	195%
	Coarse	16	45	1% < 16 um	1% > 45 um	190%

Powder size distribution was determined at Solar. Chemical analyses were performed at EWI, using a LECO ignition method or energy-dispersive x-ray spectroscopy (EDS). An outside contractor provided analyses by x-ray diffraction (XRD). Metallurgical analyses were performed at EWI; results are described in Section 3.

2.2 Process Parameter Development for Each Powder

The four powders processed differently, requiring initial and then refined process parameters to be developed for each. As the program progressed, some of the powders fell out of contention for use in the final fuel injector article. Overall this was an iterative process of build, test, refine parameter space, rebuild, re-test.

Solar used a ProX300 machine in their facility. An example of the types of parametric studies performed is given in Table 2 and Table 3. This is specific to the S1-Coarse (S1-C) and the S1-Fine (S1-F) powders. Similar studies were performed for each of the powders, S2-Fine (S1-F) and S2-Coarse (S2-C).

Table 2. Parametric Study for S1-C and S1-F Powder

Laser Power (%)	Laser Power (W)	Scan Speed (mm/s)	Hatch Spacing (mm)	Layer Thickness (mm)	Heat Input (J/mm^3)	Heat Input (J/mm^2)
98%	490	2500	0.07	0.04	70.00	2.8
93%	465	2500	0.07	0.04	66.43	2.7
88%	440	2500	0.07	0.04	62.86	2.5
83%	415	2500	0.07	0.04	59.29	2.4
78%	390	2500	0.07	0.04	55.71	2.2
73%	365	2500	0.07	0.04	52.14	2.1
68%	340	2500	0.07	0.04	48.57	1.9
63%	315	2500	0.07	0.04	45.00	1.8
58%	290	2500	0.07	0.04	41.43	1.7
53%	265	2500	0.07	0.04	37.86	1.5
48%	240	2500	0.07	0.04	34.29	1.4
43%	215	2500	0.07	0.04	30.71	1.2
38%	190	2500	0.07	0.04	27.14	1.1
70%	350	3700	0.07	0.04	33.8	1.4
70%	350	3500	0.07	0.04	35.7	1.4
70%	350	3300	0.07	0.04	37.9	1.5
70%	350	3100	0.07	0.04	40.3	1.6
70%	350	2900	0.07	0.04	43.1	1.7
70%	350	2700	0.07	0.04	46.3	1.9
70%	350	2500	0.07	0.04	50.0	2.0
70%	350	2300	0.07	0.04	54.3	2.2
70%	350	2100	0.07	0.04	59.5	2.4
70%	350	1900	0.07	0.04	65.8	2.6
70%	350	1700	0.07	0.04	73.5	2.9
70%	350	1500	0.07	0.04	83.3	3.3

Table 3. Parametric Study for S2 Coarse and Fine Powder

Laser Power (%)	Laser Power (W)	Scan Speed (mm/s)	Hatch Spacing (mm)	Layer Thickness (mm)	Heat Input (J/mm^3)	Heat Input (J/mm^2)
78%	390	2500	0.05	0.04	78.00	3.1
73%	365	2500	0.05	0.04	73.00	2.9
68%	340	2500	0.05	0.04	68.00	2.7
66%	330	2500	0.05	0.04	66.00	2.6
63%	315	2500	0.05	0.04	63.00	2.5
61%	305	2500	0.05	0.04	61.00	2.4
58%	290	2500	0.05	0.04	58.00	2.3
56%	280	2500	0.05	0.04	56.00	2.2
53%	265	2500	0.05	0.04	53.00	2.1
51%	255	2500	0.05	0.04	51.00	2.0
48%	240	2500	0.05	0.04	48.00	1.9
43%	215	2500	0.05	0.04	43.00	1.7
38%	190	2500	0.05	0.04	38.00	1.5
35%	172.5	2500	0.03	0.04	57.50	3-4
80%	400	2500	0.07	0.04	57.14	3-5
35%	172.5	1500	0.05	0.04	57.50	4-1
80%	400	3500	0.05	0.04	57.14	4-2

Later in the program, The S1-F powder was down selected for advanced process evaluation to explore the effects of parameter changes on geometric features. The parameters used in that work are given below in Tables 4 and 5. The series represented in Table 4 used constant hatch spacing and varied power and scan speed. That in Table 5 includes variances in hatch spacing.

Table 4. Design of Experiment (DOE) Developed for Studying the Effect of Laser Power at Three Levels of Scanning Speed and a Constant Hatch Spacing

ID	DOE Category	Speed (mm/s)	Heat Input (J/mm^2)	Hatch Spacing (mm)	Power (W)	Heat Input (J/mm)
L-1	Series-L	1200	2.5	0.05	150	12.5
L-2	Series-L	1200	2.9	0.05	174	14.5
L-3	DOE-L	1200	3.3	0.05	198	16.5
L-4	Series-L	1200	3.7	0.05	222	18.5
L-5	Series-L	1200	4.1	0.05	246	20.5
L-6	DOE-L	1200	4.5	0.05	270	22.5
M-1	Series-M	1750	2.5	0.05	219	12.5
M-2	Series-M	1750	2.8	0.05	245	14.0
M-3	DOE-M	1750	3.1	0.05	271	15.5

ID	DOE Category	Speed (mm/s)	Heat Input (J/mm^2)	Hatch Spacing (mm)	Power (W)	Heat Input (J/mm)
M-4	Series-M	1750	3.4	0.05	298	17.0
M-5	Series-M	1750	3.7	0.05	324	18.5
M-6	DOE-M	1750	4.0	0.05	350	20.0
H-1	Series-H	2500	2.0	0.05	250	10.0
H-2	Series-H	2500	2.3	0.05	288	11.5
H-3	Series-H	2500	2.6	0.05	325	13.0
H-4	DOE-H	2500	2.9	0.05	363	14.5
H-5	Series-H	2500	3.2	0.05	400	16.0
H-6	DOE-H	2500	3.5	0.05	438	17.5

Table 5. DOE Developed for Studying the Effect of Hatch Spacing and Scanning Speed

ID	DOE Category	Speed (mm/s)	Heat Input (J/mm^2)	Hatch Spacing (mm)	Power (W)	Heat Input (J/mm)
HL-1	DOE-L	1200	4	0.02	96	8.0
HL-2	DOE-L	1200	5	0.02	120	10.0
HL-3	DOE-L	1200	6	0.02	144	12.0
HL-4	DOE-L	1200	2	0.1	240	20.0
HL-5	DOE-L	1200	2.8	0.1	330	27.5
HL-6	DOE-L	1200	3.5	0.1	420	35.0
HM-1	DOE-M	1750	5.3	0.02	184	10.5
HM-2	DOE-M	1750	6.1	0.02	214	12.3
HM-3	DOE-M	1750	7	0.02	245	14.0
HM-4	DOE-M	1750	1.7	0.1	298	17.0
HM-5	DOE-M	1750	2.1	0.1	374	21.4
HM-6	DOE-M	1750	2.6	0.1	450	25.7
HH-1	DOE-H	2500	5	0.02	250	10.0
HH-2	DOE-H	2500	6.0	0.02	300	12.0
HH-3	DOE-H	2500	7	0.02	350	14.0
HH-4	DOE-H	2500	1.5	0.1	375	15.0
HH-5	DOE-H	2500	1.7	0.1	413	16.5
HH-6	DOE-H	2500	1.8	0.1	450	18.0

2.3 Test Article Builds and Configurations

Several test article configurations were produced throughout the program. The earliest was the NIST Test Artifact (following that published by Moylan[1] in 2012). Figure 3 below shows the article and some of its features and Figure 4 shows a finished article.

Test articles developed by Solar to represent relevant features of a fuel injector swirler geometry were used for heat treatment and geometry evaluations.

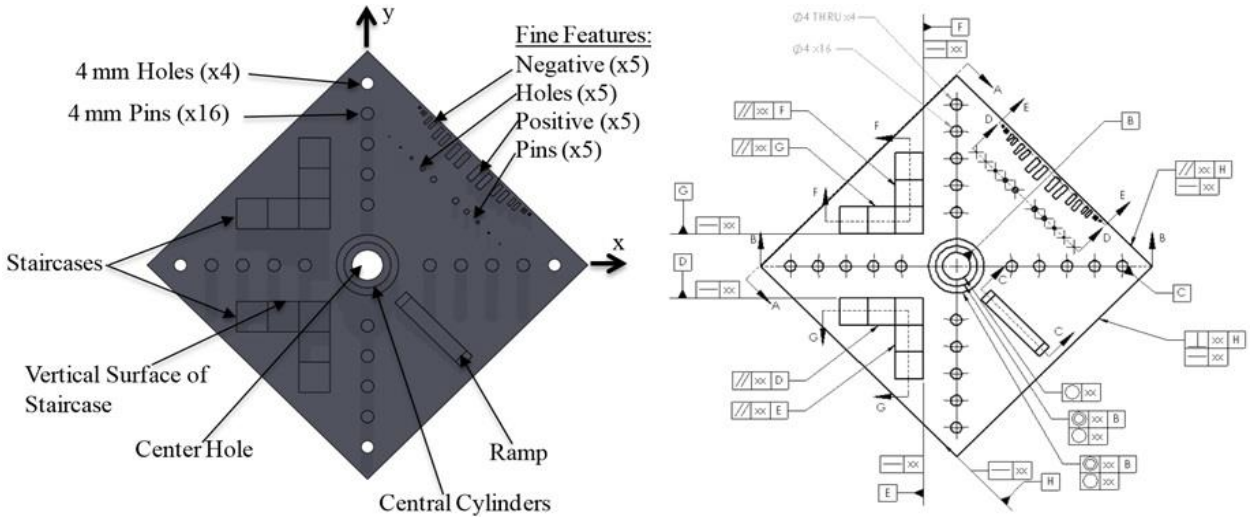

Figure 3. Design of the NIST Test Artifact with the Corresponding Features [1]

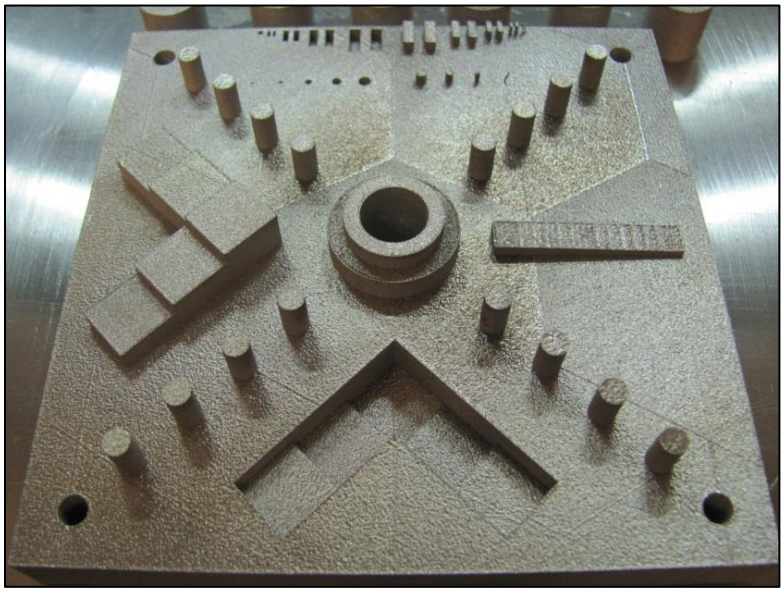

Figure 4. NIST Test Artifact Fabricated at Solar by using S1-F Powder

Figure 5 depicts the layout for the standard mechanical test specimen used throughout the program. Examples of broken specimens, produced with fine and coarse powders, are shown in Figure 6.

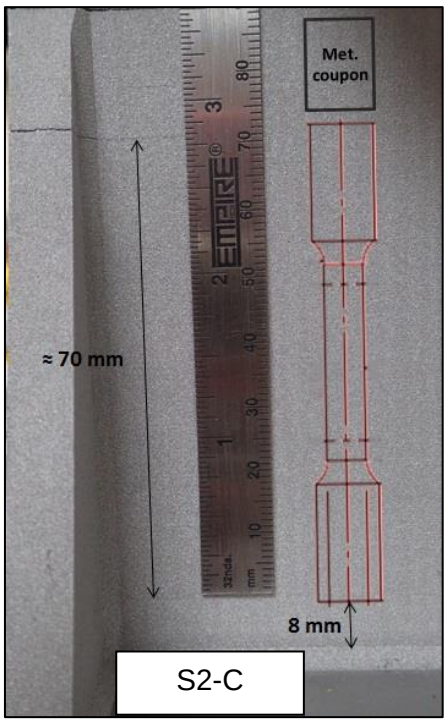

Figure 5. Layout for Electrical Discharge Machining (EDM) Cut of Mechanical Testing Specimens, per ASTM E8-09, Specimen 3

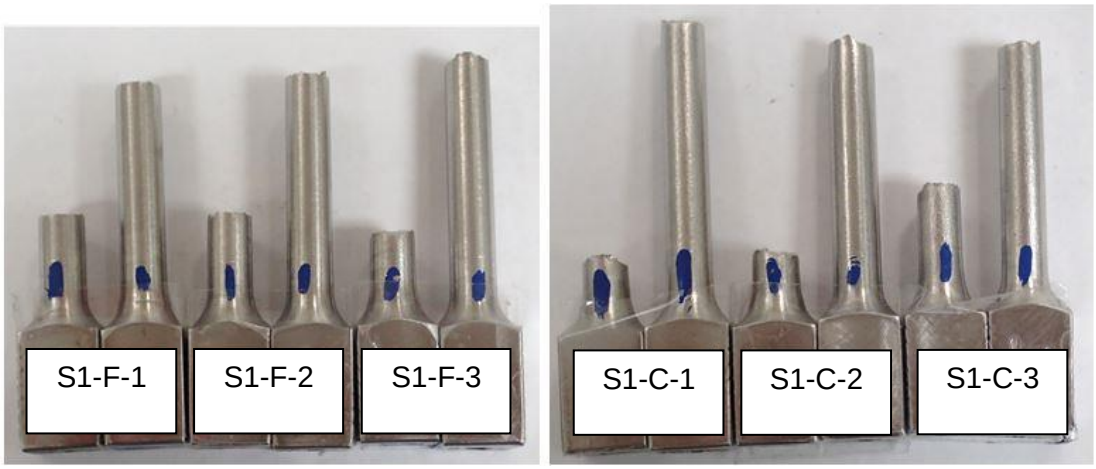

Figure 6. Broken Mechanical Test Specimens

In the later stages of the program, special designs were adopted to look specifically at overhangs, outcroppings, and undercuts. An example of one of those plate builds, based on the S1-F powder, is shown in Figure 7.

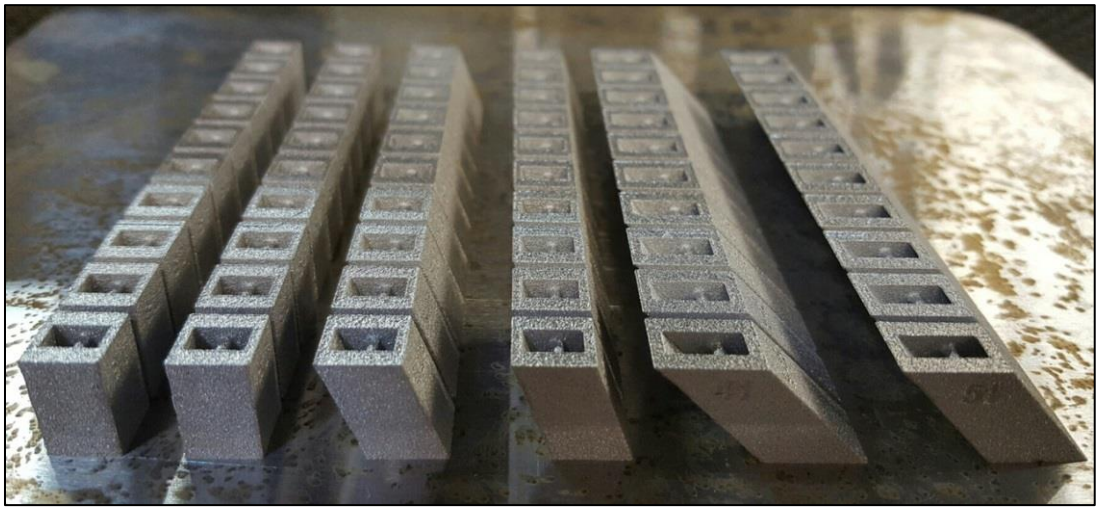

Figure 7. Test Plate Produced with Three Inclination Angles of 0, 20, and 45 Degrees (two each, left to right)

Other specimens were produced for analysis of dimensional accuracy and to be used as heat treat coupons (Figures 8 and 9).

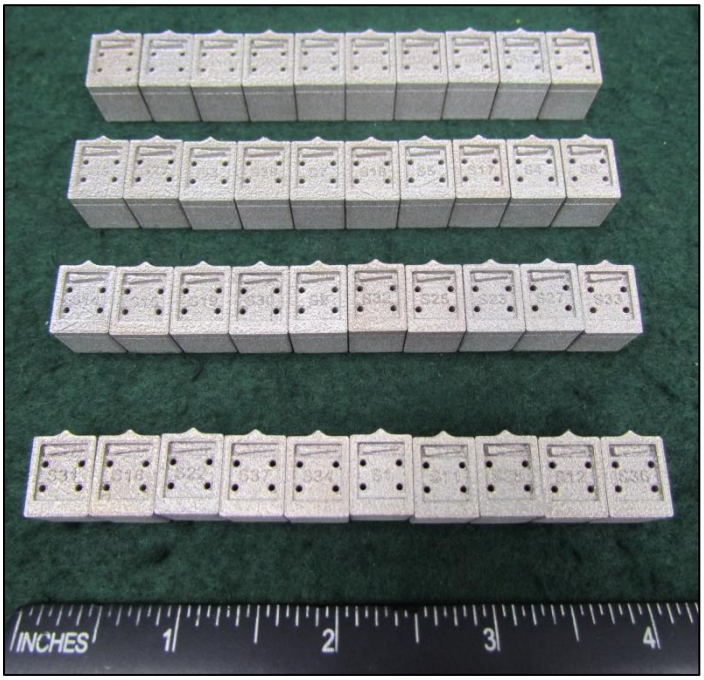

Figure 8. Heat Treatment Coupons Produced with the S1-F Powder

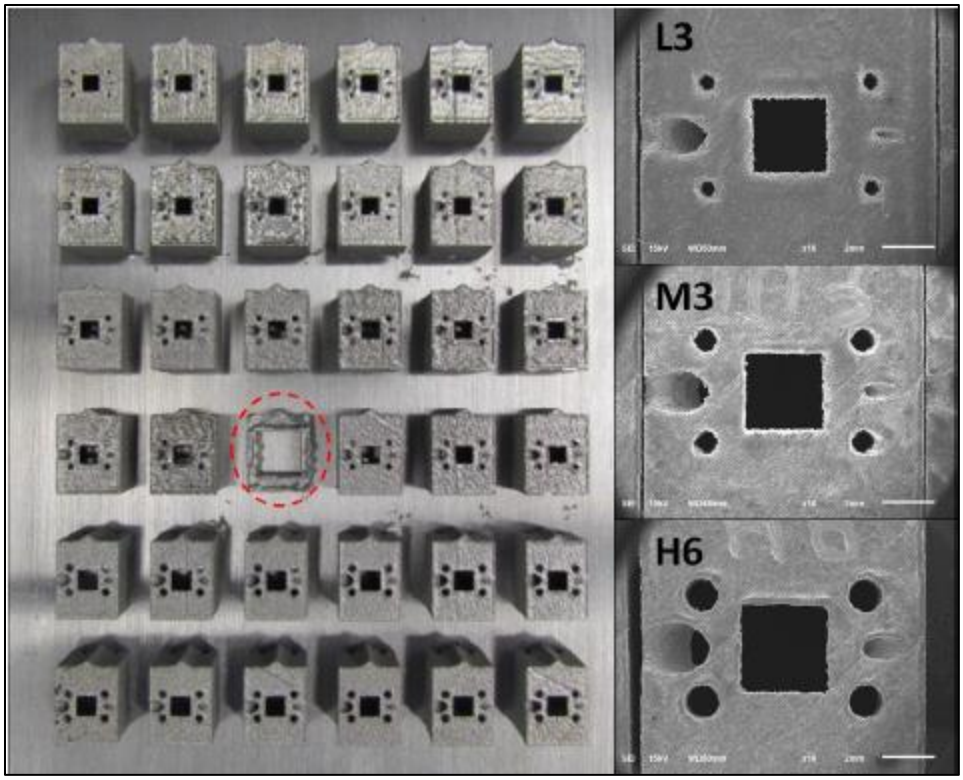

Figure 9. Coupons for Evaluation of the Effect of Parameters on Geometric Features

Another configuration was produced for use in a few creep and fatigue specimens (Figure 10).

Figure 10. Mechanical Test Walls Produced for the Fabrication of Creep and LCF Specimens along the X-Y Direction (normal to the buildup direction)

2.4 Mechanical Testing

The three major types of mechanical testing were: tensile, creep, and LCF tests. They were used routinely throughout the program. The main specimen type used was the ASTM E8-09

type shown in Figures 5 and 6 above. Elevated temperature specimens were soaked at temperature for at least 20 minutes prior to testing. These tests were used throughout to monitor changes in mechanical performance after build parameter changes and heat treatment cycles.

Tensile specimens were tested at room temperature or elevated temperature (ASTM E21). Specimens had a gauge diameter of 0.25 in. and were tested at a loading rate of 0.05 ipm. The mechanical properties derived were tensile strength, 0.2%-yield, elongation, and reduction of area.

Creep testing was undertaken by Solar through a subcontractor (Joliet Metallurgical). Typically, three, 0.25-in. gauge diameter specimens were tested at 1500°F at 15 ksi static load. Hours to rupture and elongation at rupture were reported.

LCF testing was also performed by Solar through a subcontractor, Element Cincinnati, using the 0.25-in. gauge diameter specimens. A sinusoidal waveform was used with strain range and stress ratio set to 0.6% and -1, respectively. Cycles to initiation and cycles to failure were reported.

2.5 Heat Treat Cycles

Many heat treat cycles were examined including some used in combination. This examination was also an iterative process of broad experimentation followed by selective elimination of methods and concentration on others. Tables 6-8 show this evolving process which spanned several months of the program. Procedures 3-5 in Table 6 below were subsequently abandoned, as shown in Table 7.

Seven initial heat treatment screening trials (Table 7) were performed on coupons and evaluated using standard metallographic techniques. Based on the metallographic screening results, four heat treatments (Table 8) were down-selected for full mechanical testing trials.

Table 6. Heat Treatment (HT) Procedures Developed for the Hastelloy X

HT Procedure	Sample ID	Solution Annealing			HIP				Aging					
		Temp. (°F)	Time	Post Cooling	Temp. (°F)	Pressure (MPa)	Time (hr)	Post Cooling	Temp._1 (°F)	Time_1 (min)	Post Cooling	Temp._2 (°F)	Time_2 (hr)	Post Cooling
1-a	2 & 3	2150	15 min.	ArC	---	---	---	ArC	---	---	---	---	---	---
1-b	4 & 5	2150	40 min.	ArC	---	---	---	ArC	---	---	---	---	---	---
1-c	6 & 7	2150	1 hr	ArC	---	---	---	ArC	---	---	---	---	---	---
2		---	---	---	2150	100	4	ArC	---	---	---	---	---	---

HT Procedure	Sample ID	Solution Annealing			HIP				Aging					
		Temp. (°F)	Time	Post Cooling	Temp. (°F)	Pressure (MPa)	Time (hr)	Post Cooling	Temp._1 (°F)	Time_1 (min)	Post Cooling	Temp._2 (°F)	Time_2 (hr)	Post Cooling
3		2150	TBD*	ArC	2150	100	4	ArC	---	---	---	---	---	---
4		2150	TBD*	ArC	---	---	---	ArC	1400	4*	ArC	1100	3*	AC
5		1950	TBD*	ArC	---	---	---	ArC	1400	100*	ArC	---	---	---
6	8 & 9	2150	4 hr	ArC	---	---	---	ArC	---	---	---	---	---	---
7	10 & 11	2150	8 hr	ArC	---	---	---	ArC	---	---	---	---	---	---
8	12 & 13	2200	1 hr	ArC	---	---	---	ArC	---	---	---	---	---	---

ArC: Argon Cooling
**Trial abandoned.*

Table 7. Heat Treatment Procedures Developed for the Hastelloy X

HT Procedure	Solution Annealing			HIP				Aging					
	Temp. (°F)	Time	Post Cooling	Temp. (°F)	Pressure (MPa)	Time (hr)	Post Cooling	Temp._1 (°F)	Time_1 (hr)	Post Cooling	Temp._2 (°F)	Time_2 (hr)	Post Cooling
1-a	2150	15 min.	ArC	---	---	---	ArC	---	---	---	---	---	---
1-b	2150	40 min.	ArC	---	---	---	ArC	---	---	---	---	---	---
1-c	2150	1 hr	ArC	---	---	---	ArC	---	---	---	---	---	---
2	---	---	---	2150	100	4	ArC	---	---	---	---	---	---
6	2150	4 hr	ArC	---	---	---	ArC	---	---	---	---	---	---
7	2150	8 hr	ArC	---	---	---	ArC	---	---	---	---	---	---
8	2200	1 hr	ArC	---	---	---	ArC	---	---	---	---	---	---

ArC: Argon Cooling

Table 8. Down-Selected HT Procedures for Hastelloy X

HT Procedure	Solution Annealing			HIP			Solution Annealing		
	Temp. (°F)	Time (hr)	Post Cooling	Temp. (°F)	Pressure (MPa)	Time (hr)	Temp. (°F)	Time (hr)	Post Cooling
R1	2150	1	ArC	---	---	---	---	---	---
R2	---	---	---	2150	100	4	---	---	---
R3	---	---	---	2150	100	4	2150	1	AC
R4	2150	4	ArC	---	---	---	---	---	---

ArC: Argon Cooling

2.6 Post Fabrication Methods

Post finishing treatment is necessary to provide the required surface finish and to eliminate any residual fines or particles from the surfaces. The following methods were examined:

- Grit blasting
- Tumbling
- Extrude hone/abrasive flow machining (AFM)
- Micro-machining process (MMP) technology
- Hybrid DECI duo
- Electropolish

Each method is described briefly below. Some of the methods were deemed proprietary by the vendors and no further detail is provided.

2.6.1 Grit Blast – Solar

Grit blasting is a relatively common finishing technique in a variety of industries. In this technique, an abrasive media is typically directed using compressed gas and impinges a component surface. The impacts smooth the surface and can introduce a layer of sub-surface compression depending on the media and blasting parameters. Media types range from walnut shell particles to alumina and silicon carbide. For this work, the media was Barton HPA 80 Garnet, with air pressure of 105 psi. It was performed manually in an industrial grit-blast cabinet.

2.6.2 Tumbling – Solar

Tumbling is another common surface finishing technique that rolls components in a horizontal barrel along with a dry media and, in some cases, a liquid or a chemical compound. Both the wet and dry versions of this technique employ gravity-driven impacts between components and media to smooth the surface of the components. As with grit blasting, a compression layer typically forms during this process. Unlike many of the techniques evaluated, this technique can process multiple parts simultaneously with relatively low effort from an operator. The tumbling equipment used was a Burr King VibraKing Chamber Model 25. The media employed was Tristar (AC3s) Ceramic with a tumbling time of four hours.

2.6.3 Abrasive Machining – Extrude Hone/Abrasive Flow Machining (AFM)

AFM utilizes abrasive particles suspended in a media, typically with the consistency of clay, but available over a large range of viscosity, to wear down and smooth surfaces. Custom tooling is

typically designed for each component and the abrasive media is pushed through and around the various component features. Media flow rate, pressure, temperature, and viscosity, and abrasive particle size, and particle concentration can be altered to tune the technique to a specific application. This process is commonly used for internal passages, but exterior surfaces are possible with appropriate tooling. One set of demonstration parts each was processed using high and low media flow rates. The vendor report from this method was not included with the parts.

2.6.4 MMP Technology® – MicroTek Finishing

MMP Technology® is a proprietary technique described as a mechanical-physical-catalyst surface treatment. The technique utilizes a small-scale mechanical cutting process that takes place in a tank and is reported to selectively remove those frequent ranges of roughness identified by the customer. The process parameters and finishing details were not provided by the vendor. The process is considered proprietary.

2.6.5 Hybrid DECI Duo – PostProcess Technologies

The hybrid DECI Duo system utilizes a combination of user-operated and automated surface finishing methods to improve surface finish of a component. Patent-pending “agitation algorithms” are used in combination with detergents and media in this system. Process parameters and finishing details were not provided as the technique is considered proprietary.

2.6.6 Electro-polish – Able Electro-Polishing

Electro-polishing is accomplished by attaching the component to the positive side of a power source via a rack made of titanium, copper, or bronze. The rack and separate, negative side of the power source are immersed in a chemical bath. Metal ions leave the part and are drawn towards the cathode, effectively removing material and polishing the component surface. The process parameters and finishing details were not provided as the technique is considered proprietary.

2.7 Modeling with JMatPro

JMatPro is a well-known materials-based software that can be used to predict mechanical and thermomechanical behavior based on inputted metallurgical compositions. It was used along with the derived chemical composition studies to predict behavior in and around features, such as holes, undercuts, outcroppings, and the like.

This program was executed over a period of three years. During that time, several builds were made using the four powders. As lessons were learned, efforts became more focused on specific elements of improvement moving towards the goal of being able to produce fuel injectors.

The first results were centered on obtaining and characterizing the four powders. They were identified as S1-C, S1-F, S2-C, and S2-F. Next, four builds were produced using each of the powders, in turn based on the NIST Test Artifact.[(1)] These were characterized for dimensional accuracy and overall quality. Test bars were produced based on ASTM E08-09 for mechanical testing of strength, creep, and LCF. Heat treat and post-processing methods were investigated along with their effects on performance. Throughout, chemistry and metallurgy were examined. That information was used, in some cases, as inputs to JMatPro analysis software to begin correlating predicted and found properties.

3.0 Results and Discussion

3.1 Powder Characterization

Powder size distribution analyses were performed at Solar and compared with those provided by the suppliers. The supplier information is summarized in Table 9. The results from the Solar analyses are given in Figure 11. A particle size distribution plot for the S1-F material is given in Figure 12. Pictorial representations are in Figure 13.

Table 9. Powder Analyses Compiled from Suppliers

Vendor	Type	Min. Desired Size (µm)	Max. Desired Size (µm)	Fine (%)	Coarse (%)
S1	Fine	5	38	0.1% < 5 µm	0.8% > 38 µm
S1	Coarse	20	45	4.2% < 20 µm	0.5% > 45 µm
S2	Fine	5	38	2% < 5.5 µm	1 > 38 µm
S2	Coarse	16	45	1% < 16 µm	1% > 45 µm

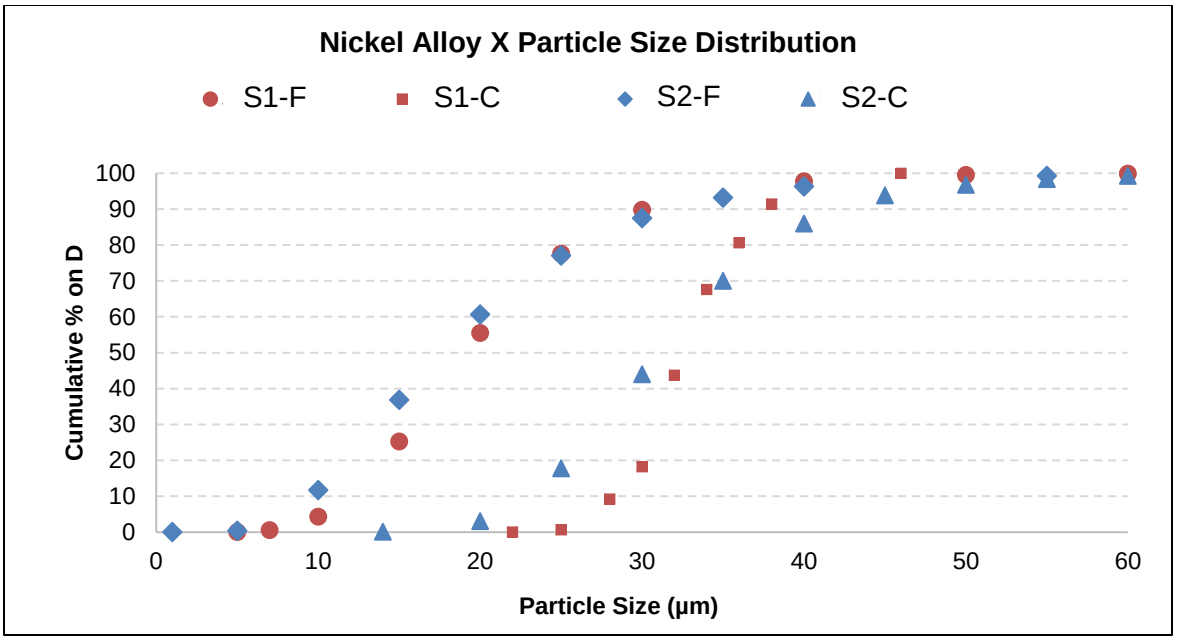

Figure 11. **Cumulative Size Distribution of the Four Nickel Alloy X Powders** (performed at Solar)

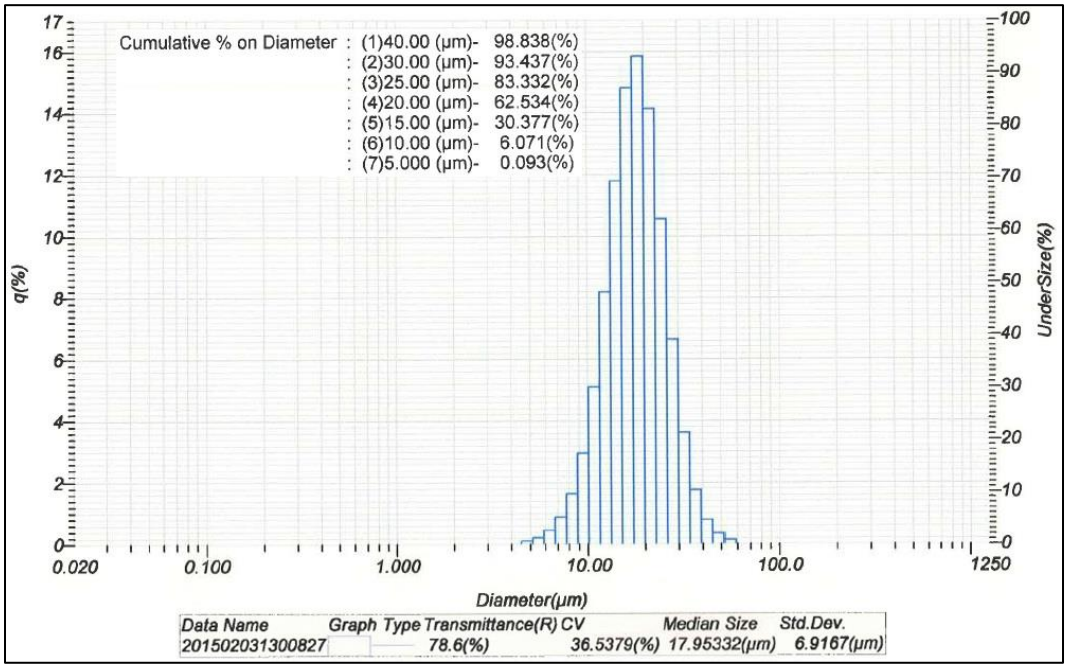

Figure 12. **Particle Size Distribution on S1-F as Measured at Solar**

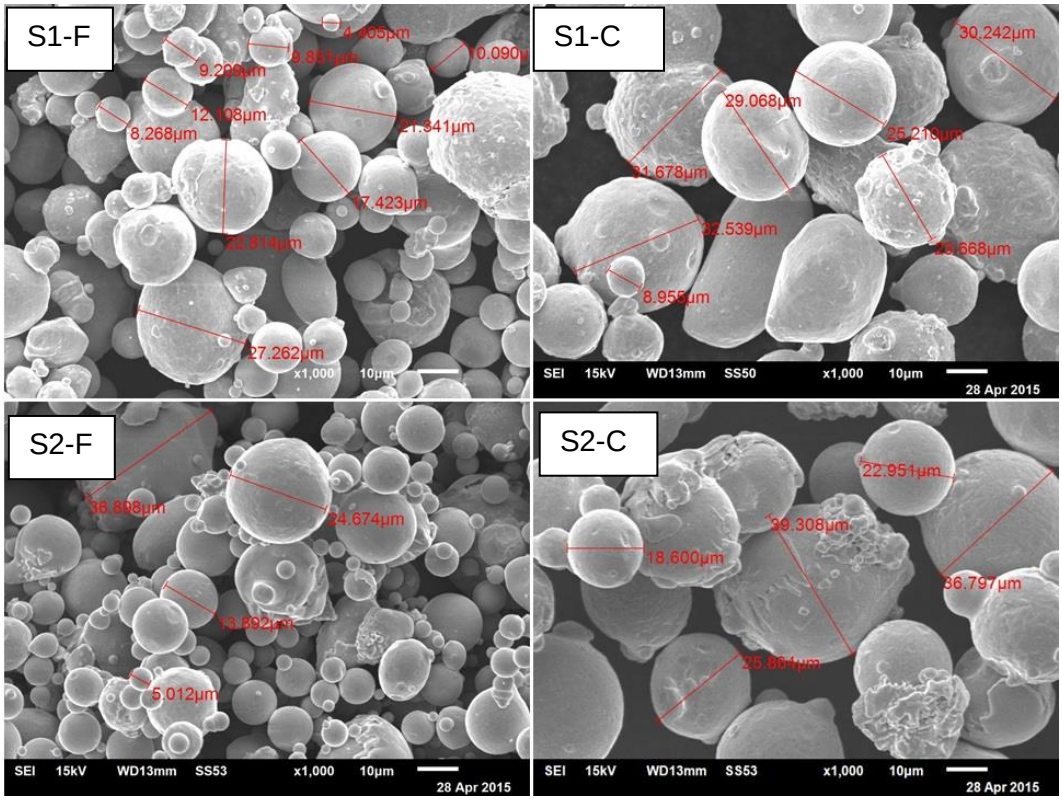

Figure 13. Scanning Electron Microscope (SEM) Images of the Powders

3.2 Production of Test Specimens

Test articles were produced using parameters derived from the processing studies. These included the four NIST test artifacts and several tensile test bars, based on ASTM E08-09.

3.2.1 NIST Test Artifacts

As part of the AM activity planned for Task 2, Solar produced the NIST test artifacts from all four of the powders. Figure 14 shows the design of the NIST test artifacts with corresponding features.

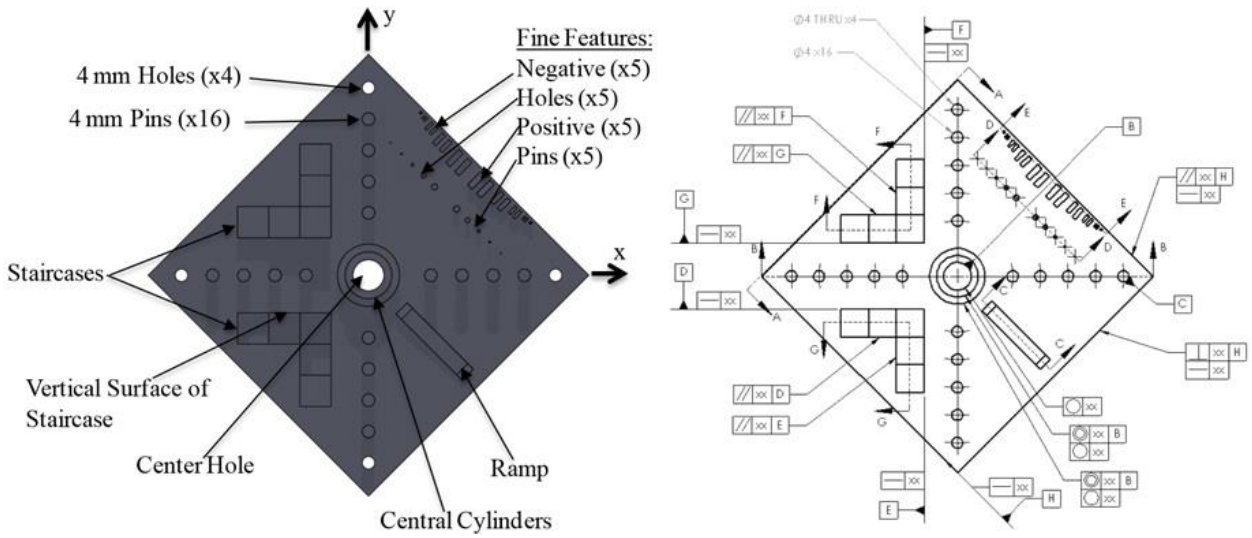

Figure 14. The Design of the NIST Test Artifact with the Corresponding Features [(1)]

Figure 15 compares the fine positive and negative rectangular features produced on the NIST test artifact with the S1-F powder; “a” and “b” are the representatives of the negative and positive rectangular features, respectively; 1 and 2 refer to features with the widths of 0.25 mm and 0.5 mm, respectively. As shown, producing both features with 0.25 mm widths was challenging. Further investigations on the NIST test artifact were conducted at EWI, after the completion of coordinate-measuring machine (CMM) inspections at Solar.

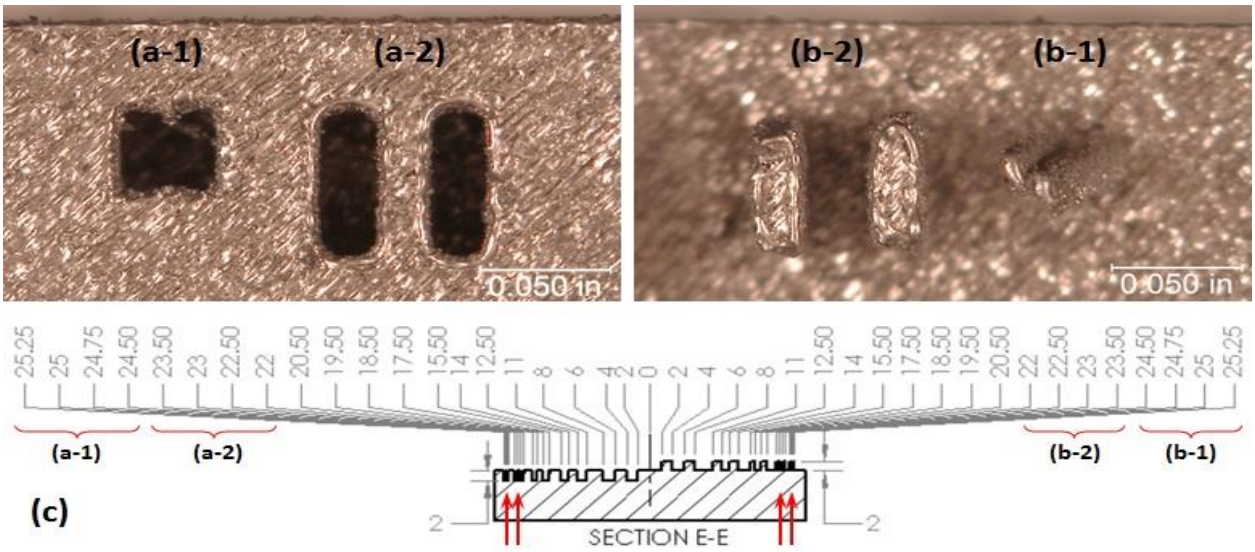

Figure 15. The Positive and Negative Rectangular Features Produced on the NIST Test Artifact by Using the S1-F Powder: a) negative features, b) positive features, 1) width= 0.25 mm, 2) width= 0.5 mm

Issues arose regarding incomplete spreading of powder (short-feed) and leaking seals that allowed insufficient powder to be distributed on the build plate. Solar investigated the possible scenarios and found the root causes. Short-feed was mainly caused by the failure of a pin-pad locator for the powder spreader mechanism in the ProX300 machine at Solar. The accelerated wearing of this device resulted in the inappropriate vertical displacement of the powder hopper, in some instances. As a result, some layers experienced lack of powder.

Figure 16 shows an example of the short-feed during the fabrication of mechanical test walls with the S1-F powder. In the consecutive layer, the nominal powder layer thickness was double the size when spread over the previously deposited build. As a result, horizontal marks or even gaps (delamination) formed on the mechanical test walls. Figure 17 shows the results of powder short-feed in mechanical test walls of S2 powders. The first set of the horizontal marks appeared at an 8-mm distance from the bottom side of the walls. Other horizontal marks and gaps were in the range of 25 mm from the top surface of the mechanical test walls.

Figure 16. Short Feed during the Building Mechanical Test Walls from S1-F Powders (the dashed line shows the area with short-feed)

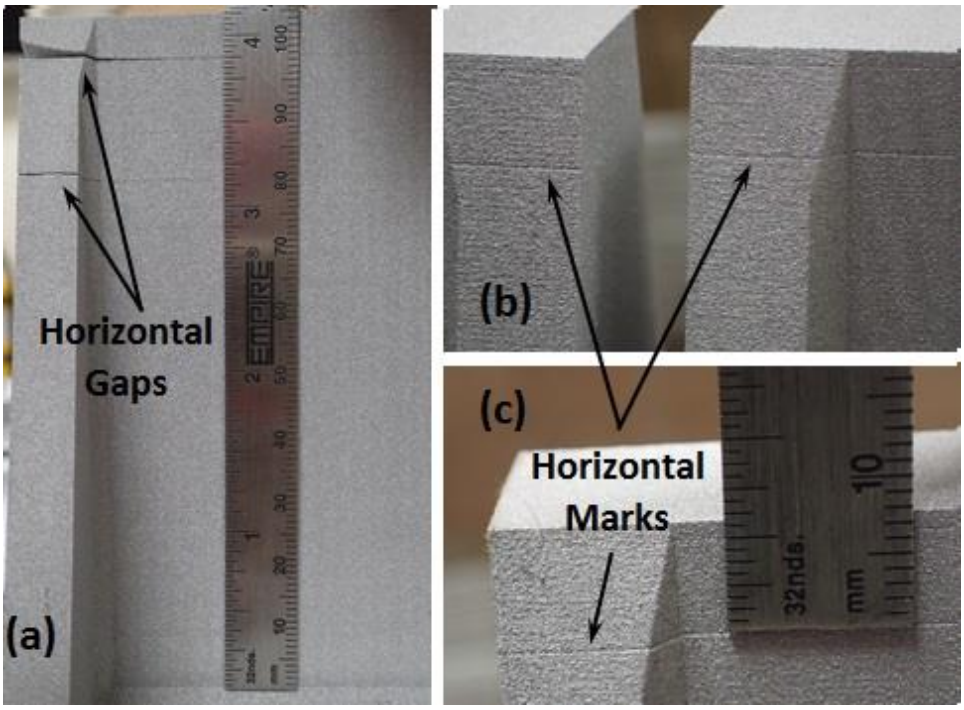

Figure 17. Horizontal Marks and Gaps Formed in the Mechanical Test Walls Due to Powder Short-feed: a) S2-F powder, b) and c) S2-C powder

3.2.1.1 Dimensional Accuracy of the Produced NIST Artifacts

The first step of the dimensional inspection was conducted through the visual comparison of the NIST test artifacts. A stereoscope was used to take images of the fine features produced with four powders. Figure 18 compares the top view of the positive fine features. All powders were able to produce the finest features. However, features produced with the S1-F powder had a smoother top surface and sharper edges. The two coarse powders showed the maximum irregularity of the surface.

The side view of the same positive fine features is compared in Figure 19. It appeared that the features produced with the S1-C, S2-F, and S2-C powders were slightly larger than those produced with the S1-F powder. The fabrication of features with a rougher surface and larger size could be an indication of the application of non-optimized process parameters. Note that the top view and side view have different scales.

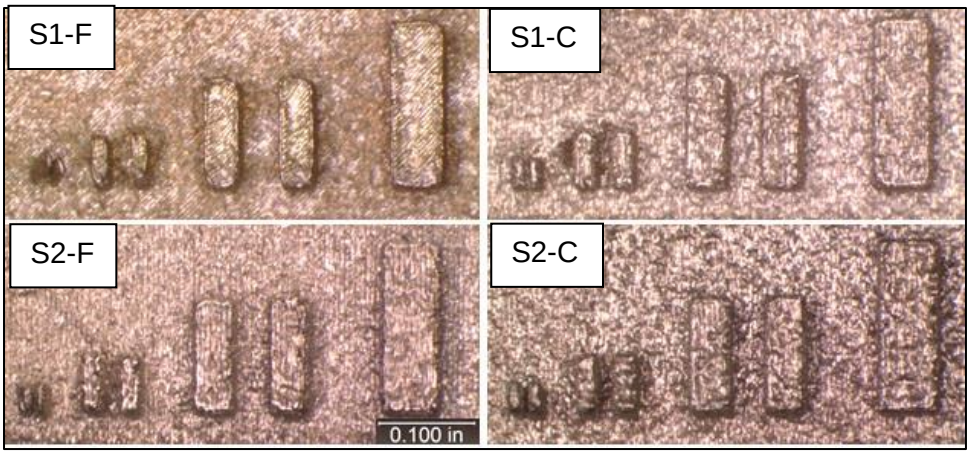

Figure 18. Top View of the Positive Fine Features on the NIST Test Artifacts Produced with the Four Powders

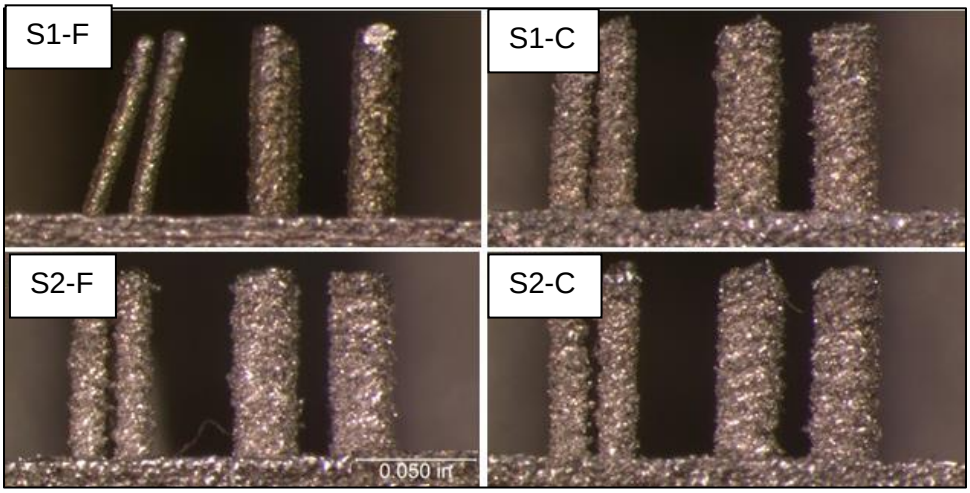

Figure 19. Side View of the Positive Fine Features on the NIST Test Artifacts Produced with the Four Powders

Figure 20 (left) compares the fabrication of a negative feature on the side wall of the NIST test artifacts. This feature has a square shape with an overhanging surface on the top. Material dropping was observed in all four of the NIST test artifacts. However, the two coarse powders showed more severe dropping on the top surface. These results are in accordance with the formation of the maximum irregularity on the external surfaces of the positive features produced with the coarse powders.

Figure 20 (right) compares the fabrication of a negative feature on the top surface of the NIST test artifacts. All the holes were identical and had the same diameter of 1 mm. However, the hole produced with the S1-F powder showed the largest diameter. Holes produced with the other three powders not only were smaller, but also had partially-fused powders attached to their inner walls. Another difference between the holes was the lack of a circular line on the periphery of the hole produced with the S1-F powder. This line should be produced by the

application of a post-contour option in the ProX300 machine. It is another indication of the application of a non-optimized process parameter for powders other than S1-F.

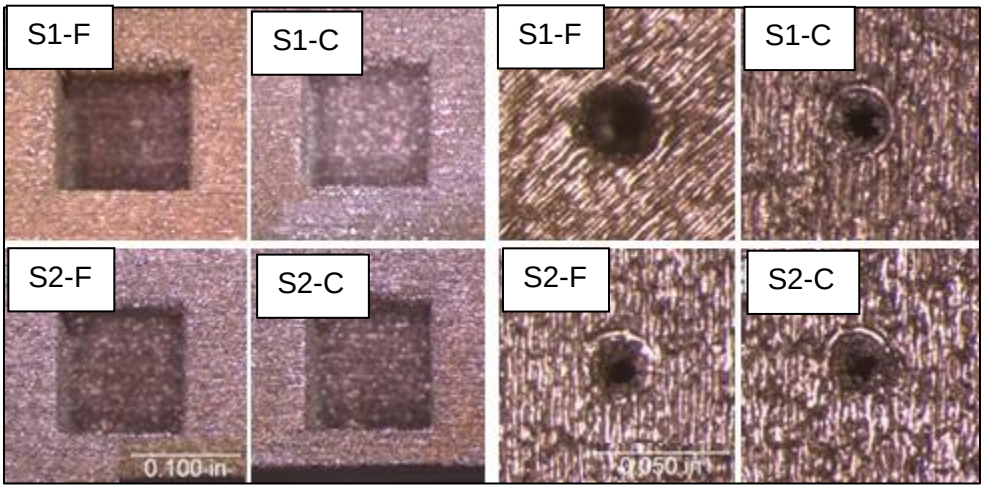

Figure 20. Comparison of the Material Dropping in a Negative Fine Feature Produced on the Side Wall of the NIST Test Artifact (left)**, Comparison of the Fabrication of a Negative Fine Feature on the Top Surface of the NIST Test Artifact** (right)

In the second step, the dimensional inspection was conducted at Solar using a CMM. Flatness, parallelism, and straightness were studied on the top, bottom, and side walls. Figure 21 compares the deviations of these parameters in the four NIST test artifacts. S1-F (P) is the representative of the NIST test artifact produced with the S2-F powder before removal from the build plate. As plotted in Figure. 21(a), all the test artifacts had a flatness deviation of 0.002 to 0.004 in.

In addition, the center hole roundness, as well as the inner and outer cylinder diameters were measured. The maximum deviation of 0.006 in. was observed in the S1-F artifact (Figure 21(b)). The minimum deviation was measured in the S1-C artifact.

All the test artifacts showed a slight deviation in terms of concentricity (Figure 18(c)). The maximum deviation in concentricity was equal to 0.002 in. and was measured in the S1-F artifact.

The positional variation of X and Y pins were plotted in Figure 22. All data were laid in the same range, with the maximum deviation of ±0.005 in. The S1-F NIST artifact had a slightly better positional accuracy. However, a decrease in the deviation of the S1-F (P) after removal from the build plate indicated the effect of residual stresses that could be initiated as a result of the fast cooling rate.

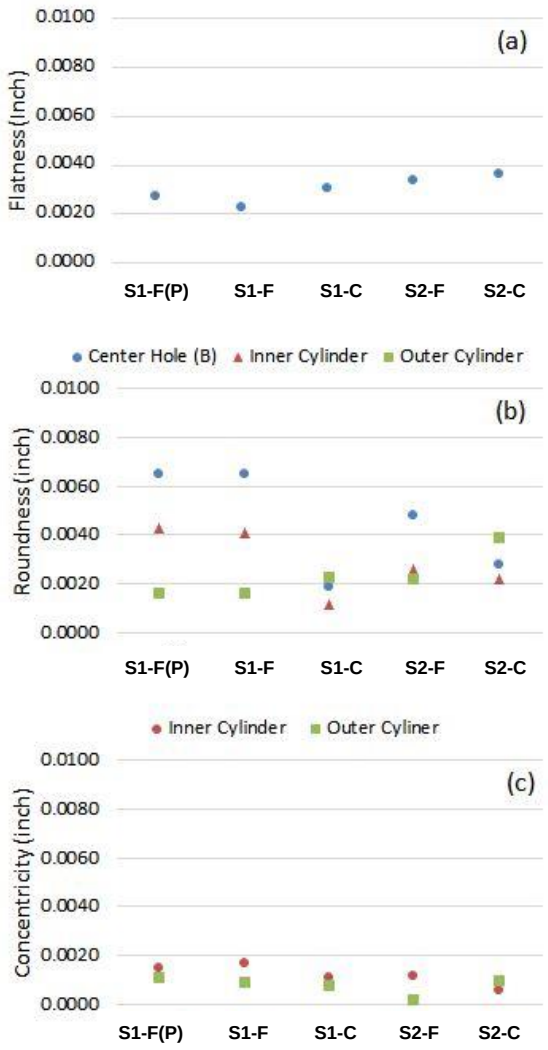

Figure 21. Flatness of Top Surface (a), Hole Roundness (b), Concentricity with the Central Hole (c)

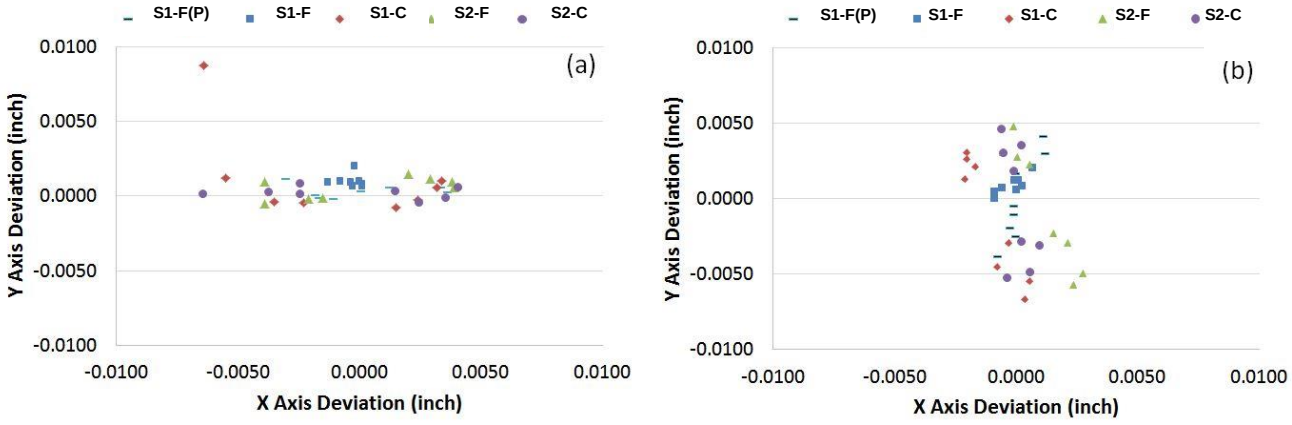

Figure 22. X-Pins Positional Variation (a), Y-Pins Positional Variation (b)

Eight pins and two holes with the nominal diameter of 0.1574 in. (4 mm) were measured in both X and Y directions. The standard deviations (σ) of these measurements were calculated. The 3σ variation in diameter was plotted in Figure 23. The maximum deviation in diameter was measured in holes of the NIST test artifact produced with the S1-F powder before removal from the build plate.

Generally, there was no significant effect of powder type on dimensional deviation. The typical allowable tolerances for cast features are in the range of ±0.005 to ±0.010 in. All powders were within that range. According to the results of CMM, it can be concluded that the L-PBF process used in this project was capable of producing fine features and met capabilities of investment casting. However, the process must be further tuned to achieve the target values of 0.157 in. (diameter).

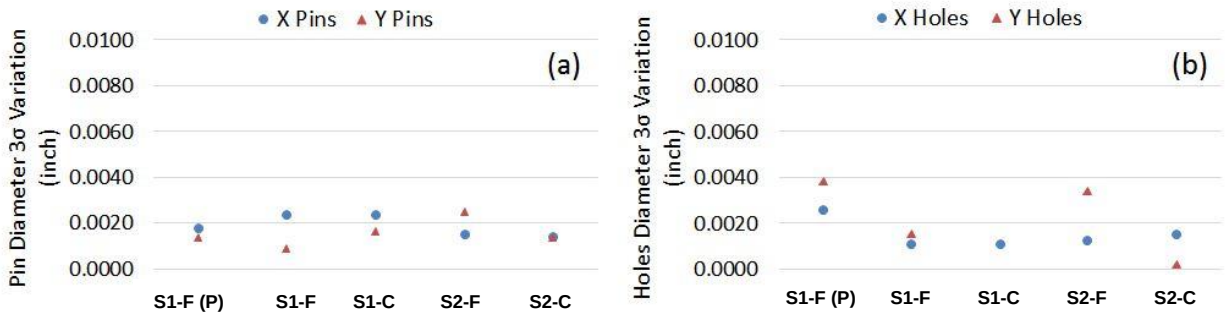

Figure 23. 3σ Variation in Diameter of Pins along X and Y Directions (a) 3σ Variation in Diameter of Holes along X and Y Directions (b)

Figure 24 shows the six locations (A-F) used for the sectioning of the NIST test artifact produced with the S1-F powder. The microstructure around the negative holes was compared in Section A. Sections B and C were used to study the formation of negative and positive fine features. Sections D and E were used to study the microstructure around the negative features, with overhanging surfaces, on the side walls. The influence of the cross-sectional thickness, as well as stress concentration sites were studied on section F.

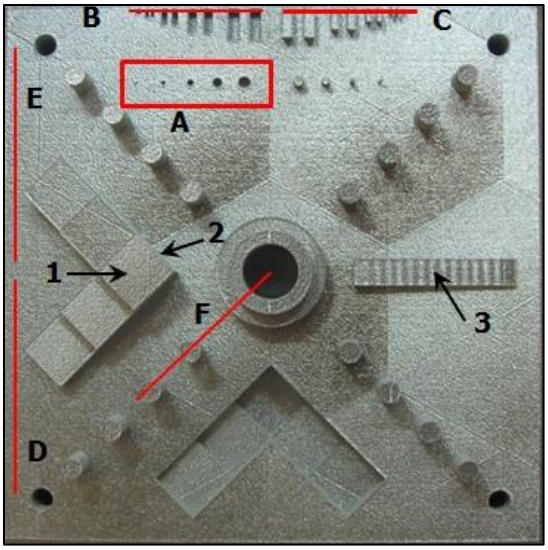

Figure 24. Layout for Hole Dimensioning, Metallurgical Sectioning, and Surface Roughness Measurement in the NIST Test Artifact Produced with the S1-F Powder

Generally, the small holes in all the powders exhibited non-uniform circular shapes. However, with increasing hole diameter, the circularity of holes increased. Figure 25 shows a high magnification image of the macrostructure formed on the top surface of the NIST test artifact produced with S1-F powder. The hole had a nominal diameter of 0.25 mm. A powder particle is partially fused to the wall and trapped inside the hole. It should be noted that similar holes with the 0.25-mm nominal diameter were partially or completely fused in the NIST test artifacts produced with the other three powders.

Figure 25. High Magnification Imaging of Macrostructure in the NIST Test Artifact Produced with the S1-F Powder (the hole has a nominal diameter of 0.25 mm)

Figure 26 compares the macrostructure around a 1-mm hole produced on the top surface of the NIST test artifacts. Similar to the results of stereoscopy presented in Figure 21, the holes

produced with the S2-F, S2-C, and S1-C powders had much smaller diameters than the nominal size.

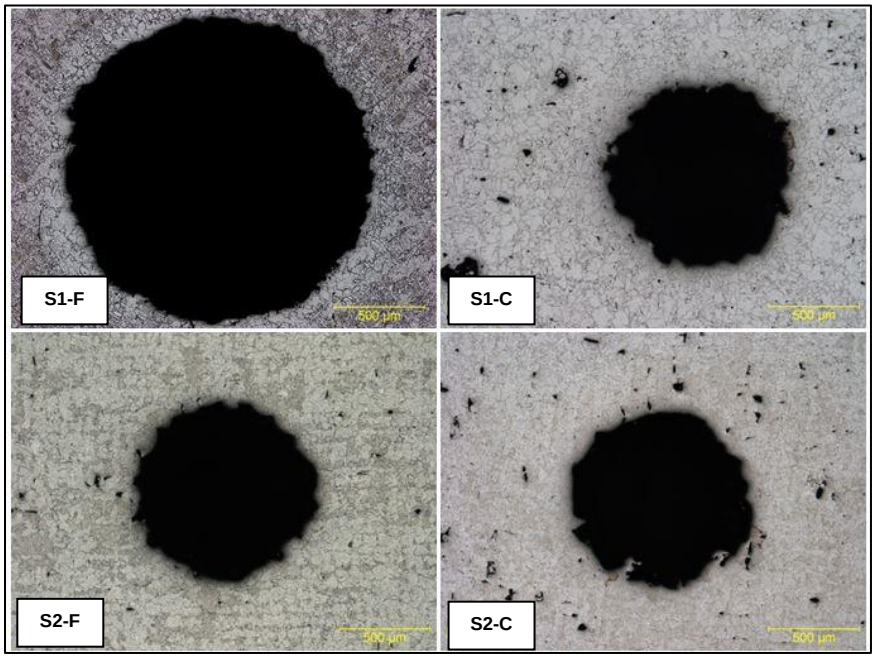

Figure 26. Comparison of the Macrostructure Formed around a 1-mm Hole on the Top of the NIST Test Artifacts

The two powders from S2 had the maximum levels of porosity, while, the specimen produced with the S1-F powder showed the minimum porosity.

Figure 27 illustrates the microstructure of Hastelloy X along the buildup direction. During the solidification, grains tend to grow along the heat transfer direction, but in the opposite direction. Since the build plate is the main heat sink during the L-PBF processes, grains with high aspect ratios formed along the buildup direction.

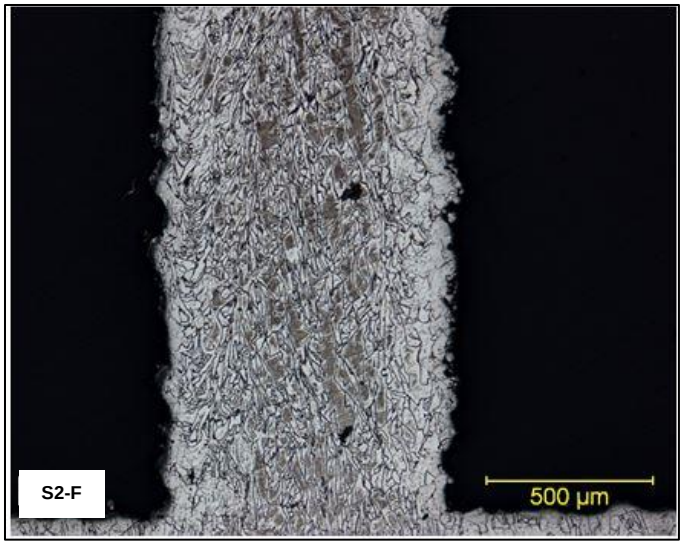

Figure 27. Formation of Grains with High Aspect Ratios along the Buildup Direction

Figure 28 compares the high magnification images of microstructures produced with the four powders. One major difference between the microstructures was a lower volume fraction of precipitates in the S2 specimens. Also, S2 specimens had larger grains, compared to those of the S1 specimens. The difference in grain sizes could be attributed to the grain growth during HT. All specimens underwent stress relief HT at 2150°F for one hour.

The exposure to high temperatures can activate grain growth. However, the presence of higher amounts of precipitates in the S1 specimens could hinder the mobility of grain boundaries. Therefore, S1 specimens experienced a slower grain growth. Also for all powders, thinner walls represented the lowest volume fraction of precipitates that could be attributed to the higher cooling rates in thin walls. Precipitation increased with an increase in wall thickness. In addition, in both cases, the finer powder revealed lower amounts of precipitates.

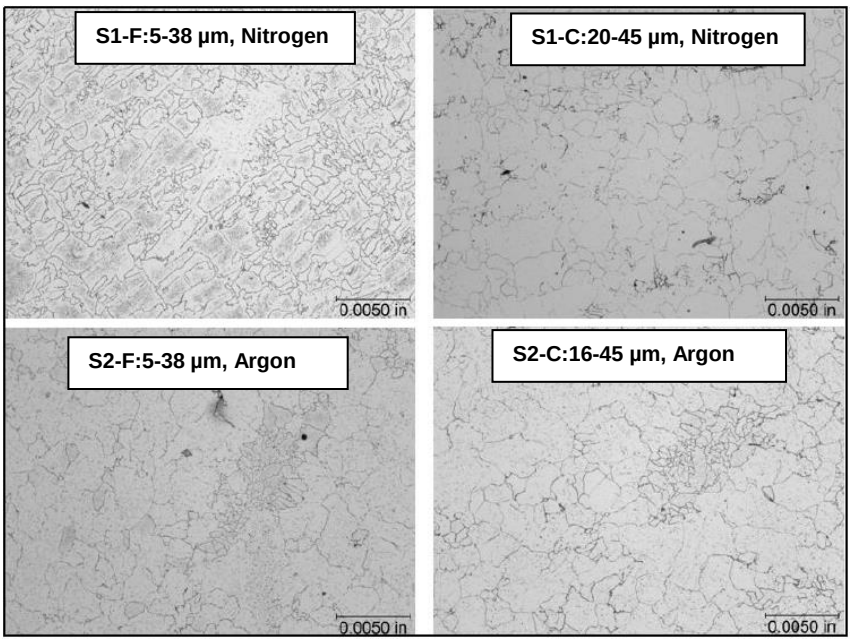

Figure 28. Comparison of the Microstructure in Specimens Produced with the Four Powders and HT at 2150°F/hour (the S1-F specimen displayed minimal grain growth in contrast to the significant grain growth for the other three powders)

3.2.1.2 Surface Roughness Measurements on the NIST Artifacts

Surface roughness measurements were performed on all four NIST test artifacts. Three representative surfaces were selected, including the top and side surfaces of the positive staircase, as well as the top surface of the ramp. These three surfaces are denoted by 1, 2, and 3, respectively, in Figure 24. Surfaces were scanned using an Alicona IF Sensor R25 machine.

The ramp is the only feature on the NIST test artifact that is solely designed to investigate the surface roughness. The ramp has a constant slope of 2.3 degrees, by a 1-mm rise over a 25-mm length. Due to the discrete layer thickness of any AM process, a stair-step effect appears on the ramp top surface.(1) Figure 29 shows the 3D reconstruction of the ramp top surface in the S1-F NIST test artifact. The stair-stepping effect can be clearly recognized in the form of some lines across the length.

Ra and Sa, the 2D and 3D arithmetic mean heights, respectively, were calculated. Table 10 summarizes the results of Sa measurements. All powders showed an almost identical surface roughness on the side wall of the staircase. However, on the top surfaces of the staircase and on the ramp, the S1-F powder showed a slightly lower surface roughness. As expected, a decrease in the powder size was accompanied by the formation of smoother surfaces. The second-lowest surface roughness was measured on the S2-F powder. The two coarse powders had an almost similar surface roughness on the top surfaces, as shown in Figure 30.

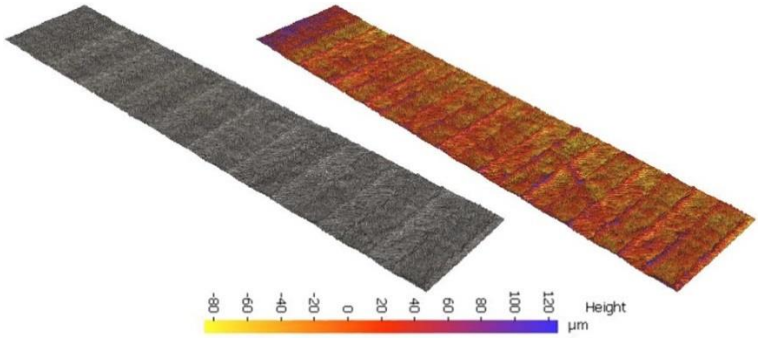

Figure 29. The 3-D Reconstruction of the Top Surface of the Ramp on the NIST Test Artifact Produced with the S1-F Powder

Table 10. Results of Surface Roughness Measurement (Sa, µm) on the NIST Test Artifacts

Scanned Surface	NIST-S1-F	NIST-S1-C	NIST-S2-F	NIST-S2-C
Staircase - Top Surface	10.431	17.506	14.705	18.495
Staircase - Side Wall	14.709	16.230	19.114	17.378
Ramp	22.092	27.083	24.652	26.944

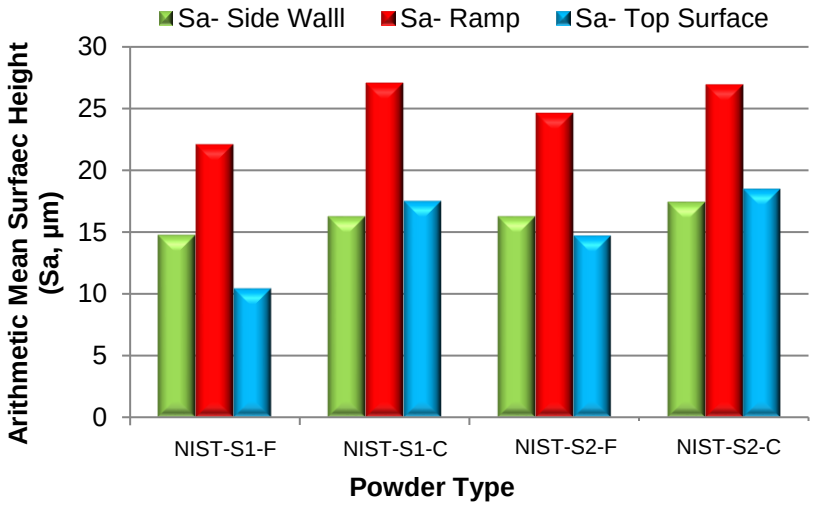

Figure 30. Results of the Surface Roughness Measurement Conducted on the NIST Test Artifacts

The typical maximum allowable limit for the surface finish of investment casting is Ra less than 125 µin. (3.17 µm). All powders showed a higher level of surface roughness. Further optimization of the process parameters was conducted in Task 3, to satisfy this requirement.

3.2.1.3 Chemistry and Metallurgy of the NIST Artifacts

3.2.1.3.1 Chemistry. EWI conducted the chemical analysis through Element Materials Technology. Chemical compositions of the four buildups are compared with those of the four powders in Table 11. All powders met the standard specification for the chemical composition. However, the two powders provided by S1 had higher levels of N, Mn, and Si.

Table 11. Comparison of the Chemical Compositions of the Four Powders and the Four Buildups

Element	S1-F		S1-C		S2-F		S2-C	
	Powder	Build*	Powder	Build*	Powder	Build*	Powder	Build*
Aluminum	---	0.02	---	0.01	0.02	0.04	0.03	0.04
Boron	---	0.002	---	0.003	0.004	0.007	0.005	0.007
Carbon (total)	0.03	0.05	0.03	0.03	0.1	0.10	0.05	0.10
Cobalt	1.54	1.65	1.43	1.54	1.57	1.70	1.49	1.69
Chromium	20.5	21.44	20.8	20.88	22.12	21.68	21.57	21.73
Copper	---	0.14	---	0.14	---	0.12	---	0.12
Iron	19.2	19.12	19.8	19.72	17.33	16.35	18.14	17.00
Hydrogen	---	0.0003	---	0.0003	0.001	0.0001	---	0.0002
Manganese	0.89	0.85	0.86	0.83	0.04	0.03	0.14	0.10
Molybdenum	8.8	9.40	8	9.64	8.85	9.61	8.86	9.60
Nitrogen	---	0.10	0.11	0.10	0.01	0.02	0.01	0.01
Nickel	Balance	Balance	Balance	Balance	Balance	Balance	Balance	Balance
Oxygen	---	0.05	0.08	0.06	0.02	0.02	0.02	0.02
Phosphorous	0.011	0.021	0.01	0.015	<0.005	0.008	<0.005	0.010
Sulfur	0.004	0.006	0.005	0.005	0.002	0.004	0.002	0.004
Silicon	0.85	0.88	0.8	0.82	0.1	< 0.01	0.11	0.14
Titanium	---	0.02	---	< 0.01	---	< 0.01	---	0.01
Tungsten	0.68	0.77	0.69	0.81	0.97	1.13	0.71	1.09

**Analysis by LECO combustion, ASTM E 1019 (C, S), SOP 10.08 (O, N), SOP 10.09 (H), ICP per SOP 10.30 (all the elements)*

3.2.1.3.2 Metallurgical Analysis. Hastelloy X is a solid solution-strengthened superalloy. Its microstructure generally consists of austenite grains with fine precipitates. Carbides are the main types of precipitates and can form inside grains and on grain boundaries. M_6C carbide is effective in blocking dislocations movement and strength enhancement. However, it is an unstable phase and decomposes to new carbides during long-term and high thermal operation. $M_6C + M' \rightarrow M_{23}C_6 + M''$ is the dominant decomposition formula. The M′ and M″ can be substituted with Cr and Co or Mo, respectively.[2-4]

Similar to M_6C carbides, $M_{23}C_6$ carbides have the same face-centered cubic crystal structure. $M_{23}C_6$ is rich in chromium. The σ and μ carbides with a topologically close-packed (TCP) structure can form as the result of the decomposition of M_6C carbides. The σ phase, with a plate/needle-like morphology, has a (Fe,Mo)x(Ni,Co)y form, while the μ phase is a blocky shape and rich in Mo. Both phases are very hard and brittle and can be sources for crack initiation and brittle fracture.[5] The formation of continuous films of carbide precipitates on grain boundaries can deteriorate properties by lowering ductility.

The dark-field optical images of the S1-C and S2-C specimens were compared in Figure 31. The appearance of precipitates with different color could be a qualitative indication for the formation of carbides with different types.

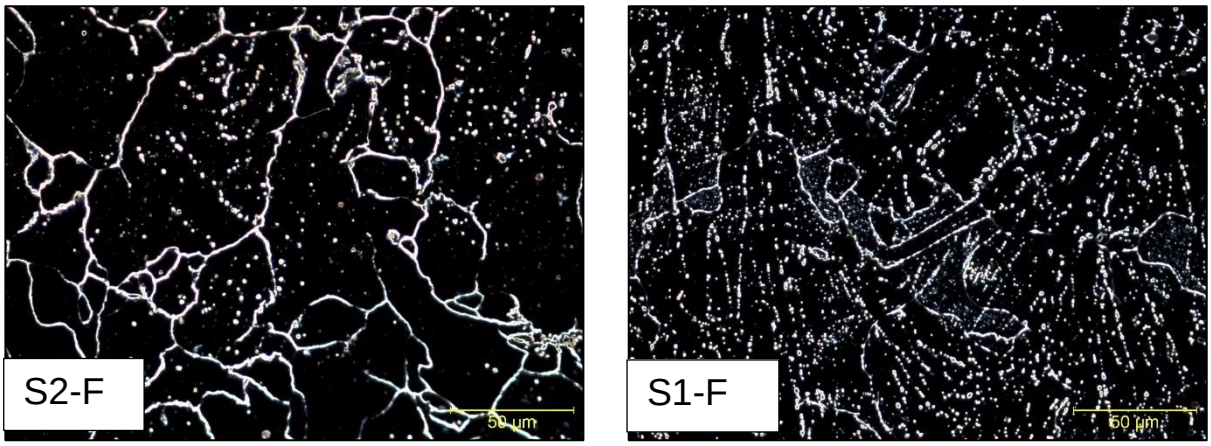

Figure 31. Comparison of the Dark-field Optical Images in the S1-F and S2-F Powders (the presence of different types of carbides was confirmed by the observation of precipitates with different colors)

The samples were also investigated using a scanning electron microscope (SEM). Figure 32 illustrates the morphology and distribution of precipitates formed in the S2 and S1 specimens at 5000× magnification. A limited amount of intra-granularity was observed in the S2 specimen, while the S1 specimen had a higher amount of precipitates. Also, the S2 specimen showed a notable grain growth.

To have a better understanding of the types of precipitates, EDS was used for a qualitative comparison of chemical compositions. Several precipitates located either on grain boundaries or inside the grains were analyzed. Figure 32c and 32d compare the higher magnification views of two precipitates in the S1 and S2 specimens, respectively. The EDS analyses of the precipitates are presented on the right side. High contents of Cr, Mo, Ni, and Fe elements were detected in the precipitates. However, the evidence in the images and the EDS results is not strong enough to differentiate between the carbide and TCP phases.

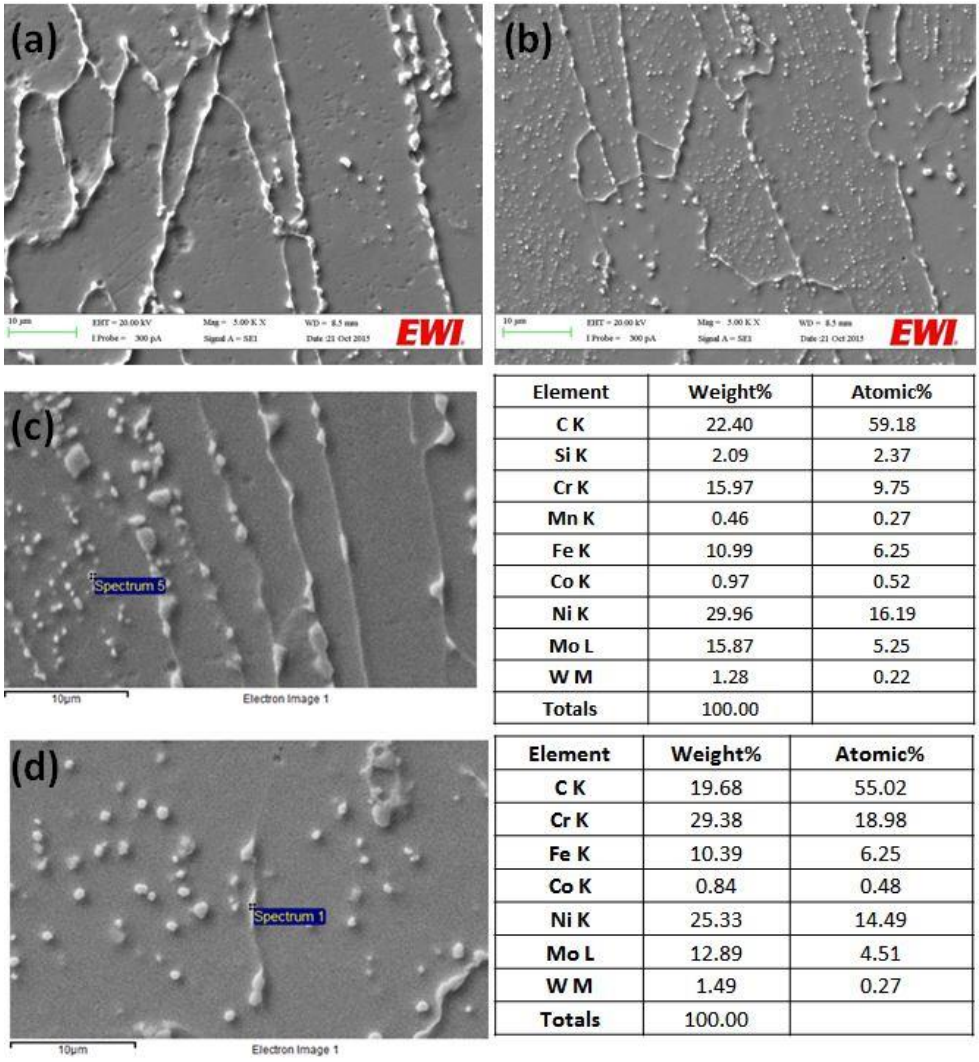

Element	Weight%	Atomic%
C K	22.40	59.18
Si K	2.09	2.37
Cr K	15.97	9.75
Mn K	0.46	0.27
Fe K	10.99	6.25
Co K	0.97	0.52
Ni K	29.96	16.19
Mo L	15.87	5.25
W M	1.28	0.22
Totals	100.00	

Element	Weight%	Atomic%
C K	19.68	55.02
Cr K	29.38	18.98
Fe K	10.39	6.25
Co K	0.84	0.48
Ni K	25.33	14.49
Mo L	12.89	4.51
W M	1.49	0.27
Totals	100.00	

Figure 32. Microstructural Analysis of the NIST Test Artifact: (a) S2-C Specimen Shows Grain Growth with Low Amount of Precipitates, (b) S1-C Specimen with High Amount of Precipitates and Fine Grains, (c) EDS Analysis of Precipitates in the S1-C Specimen, (d) EDS Analysis of Precipitates in the S2-C Specimen

3.2.1.3.3 Influence of Chemistry and Metallurgy on Structural Performance – Application of JMatPro.

The differences in chemical composition of powders can contribute to the formation of different precipitates. S1 powders had higher contents of Mn and Si, compared to S2 powders (Table 12). Theoretical calculations using JMatPro software were used to investigate this effect. As shown in Figure 33, the higher Mn and Si contents in the S1 powders can result in the formation of a wider solidification range than that of the S2 powders. A change in the solidification range can alter the mode of solidification, grain size, and types of precipitates. It must be noted that the S1 powders have higher contents of nitrogen, too. Nitrogen, as an austenite stabilizer, can alter the types and content of precipitates.

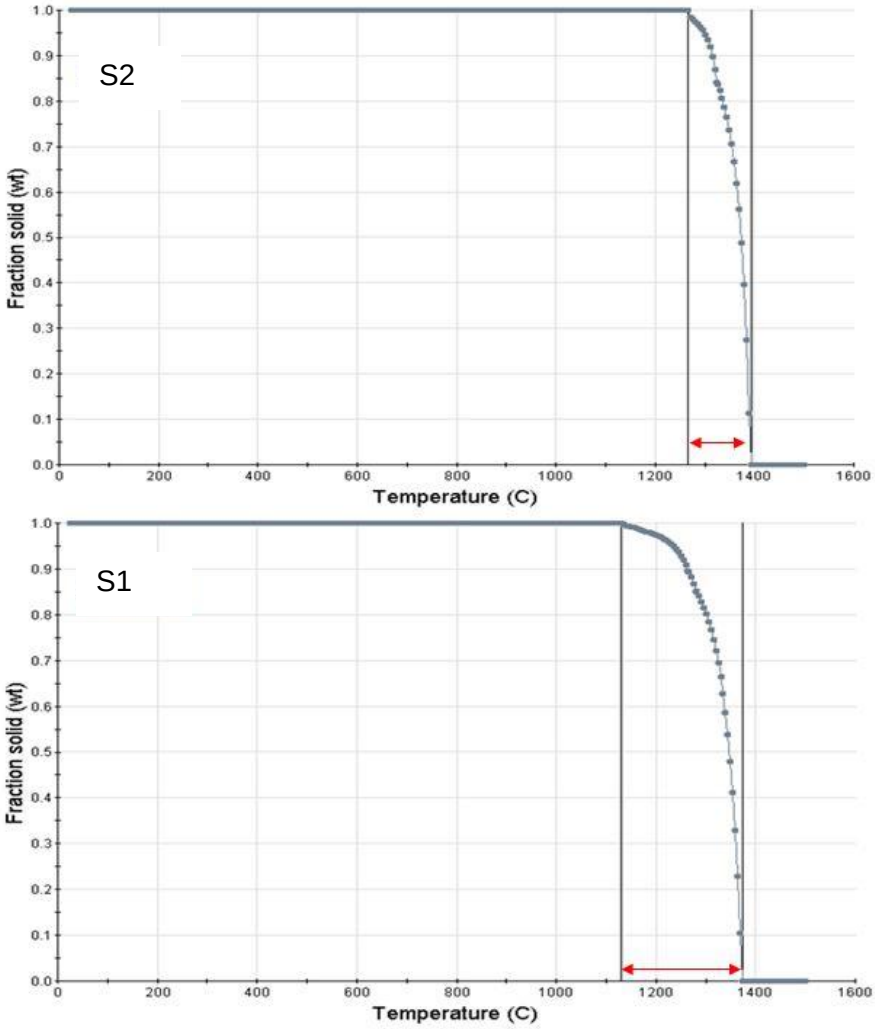

Figure 33. The Comparison of Theoretically Calculated Solidification Ranges Using JMatPro Software

Figure 34 compares the formation of cracks in the microstructure of the NIST test artifacts. In the specimens produced with the two S1 powders, cracks were initiated from the sharp corners around the central hole and propagated into the structures. No crack was detected in the NIST test artifacts produced with S2 powders. The higher amount of Mn and Si could increase the tendency for hot cracking in the S1 specimens.

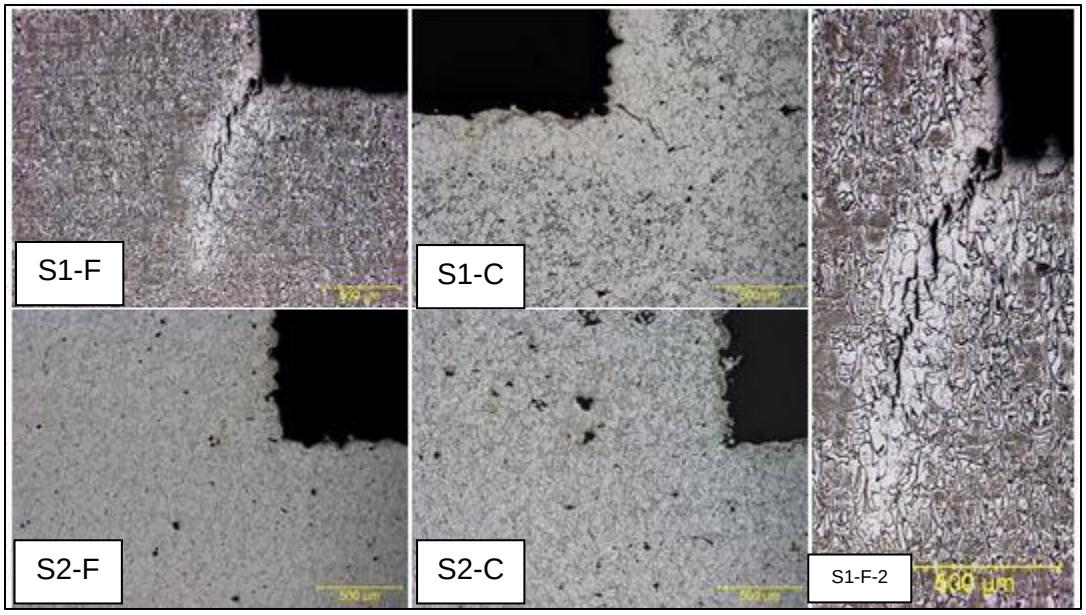

Figure 34. The Comparison of the Crack Formation on the Sharp Corners (SF-2 shows the cracked zone in the SF specimen, at a higher magnification)

The analysis of compositions indicated that the S1 specimens were more prone to solidification/liquation cracking because of the expanded solidification temperature range (Figure 33). However, investigation of the cracked zone at a higher magnification suggests that cracking occurred more likely due to residual stresses that developed during L-PBF or heat treatment.

Bright areas were observed along and around the crack (Figure 34). The same area was also depleted in precipitates. Interestingly, the same phenomenon was observed on the periphery of holes on the top surface (Fig. 26), as well as on the edges of thin features. Figure 35 shows a higher magnification of the bright band formed in the S1-C specimen. At the edge of the hole, the microstructure reveals grain boundary precipitates, with very few precipitates formed inside the grain.

The volume fraction of precipitated carbides gradually increased from the edge of the hole toward the bulk of the sample. In addition, the grain size at the edge of the hole is larger than the bulk of the samples. One explanation could be the development of a higher level of thermal stress at the edge of holes caused by the higher cooling rate. In addition, the faster cooling

leads to a lower volume fraction of precipitates. During the heat treatment, the residual stress can be considered as the driving free energy for recrystallization. Therefore, it can be concluded that the grain coarsening phenomenon occurred faster in the depleted area.

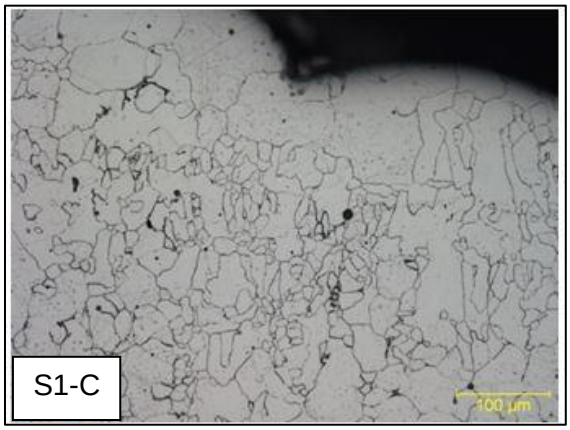

Figure 35. Formation of a Depleted Area along and around the Crack (a depleted area was also formed on the edge of fine features)

3.2.1.3.4 Porosity. Figure 36 compares the cross-sectional analysis of specimens produced by the four powders. The same process parameters were used for all powders. The S1-F powder showed the maximum density of 99.9%, as expected. The other three powders had elevated levels of voids (lack of fusion).

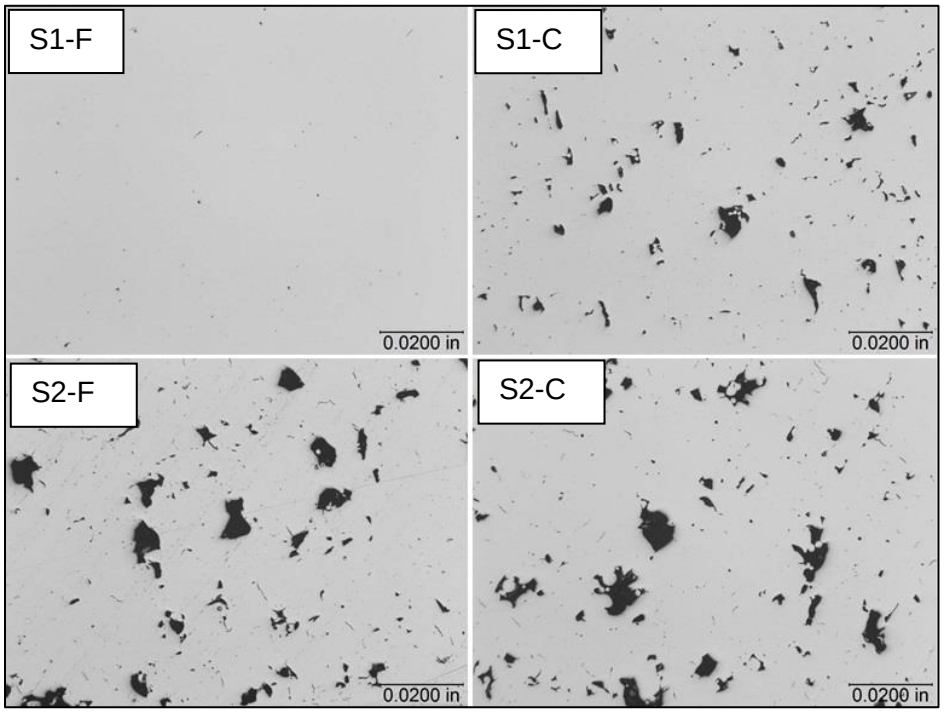

Figure 36. Comparison of the Formation of Defects in Specimens Produced by the Four Powders (same process parameters were used to produce all specimens)

Table 12 compares the level of voids in the mentioned specimens. Image analysis was used to estimate the density on one sample per powder, based on the calculation of surface-area fraction of voids. These results show that the density of a final AM material is sensitive to both particle size distribution (PSD) and powder manufacturer.

Table 12. Level of Void Measured by Image Analysis in Specimens Produced by the Four Powders (same process parameters were used to produce all specimens)

	S1 – F	S1 – C	S2 – F	S2 – C
Void (%)	0.01	2.03	4.57	4.50

3.2.1.3.4. Parametric Study on S2 Powders. This unexpected porosity was a cause for concern as the material would not meet the density requirement for the fuel injector. It became necessary to revisit process parameters for the S2 powders. That was undertaken with an additional parameter-space study. Thirteen levels of laser power were used from 190 to 390 W. Figure 37 shows the optical macroscopic images of the cylindrical specimens produced with the S-F powder, as an example. The highest and lowest levels of laser power were set for Specimens 1 and 13, respectively. A noticeable difference in the optimization of process parameters for the S2-F powder was cracking. The higher magnification images of Specimen 10 in Figure 37 compare the population of cracking at the center and around the edges. Micro-cracks mostly formed around the edges, with the minimum or no cracks in the core of cylinders. This could be related to the type of stresses developed in the specimen. The solidification and cooling of the molten top layer is accompanied by shrinkage. Because shrinkage is restricted by cooler underlying layers, a tensile stress develops on the top layer. If the tensile stress exceeds the ultimate tensile strength of material at a given temperature, the solid-phase fracturing occurs. With the lack of constraints around the edges, material can easily fracture.

The cracking tendency decreased with a decrease in laser power. Figure 38 compares the cracking tendency in Specimens 1 and 7, produced with the laser power of 390 and 290 W. Sample 7 was processed using the process parameters developed by the L-PBF machine manufacturer for the S1-F material. At a higher heat input, a larger thermal gradient develops in the structure. Therefore, a higher thermal stress forms in a specimen and could increase the number of micro-cracks.

The second set of process optimizations was conducted to identify a small process window between the excessive porosity and excessive micro-cracking. A 60-µm hatch size was also used, in addition to the initial setting at 50 µm. Although the cracking tendency slightly decreased at the hatch size of 60 µm, there did not appear to be an obvious processing window between the onset of cracking and porosity.

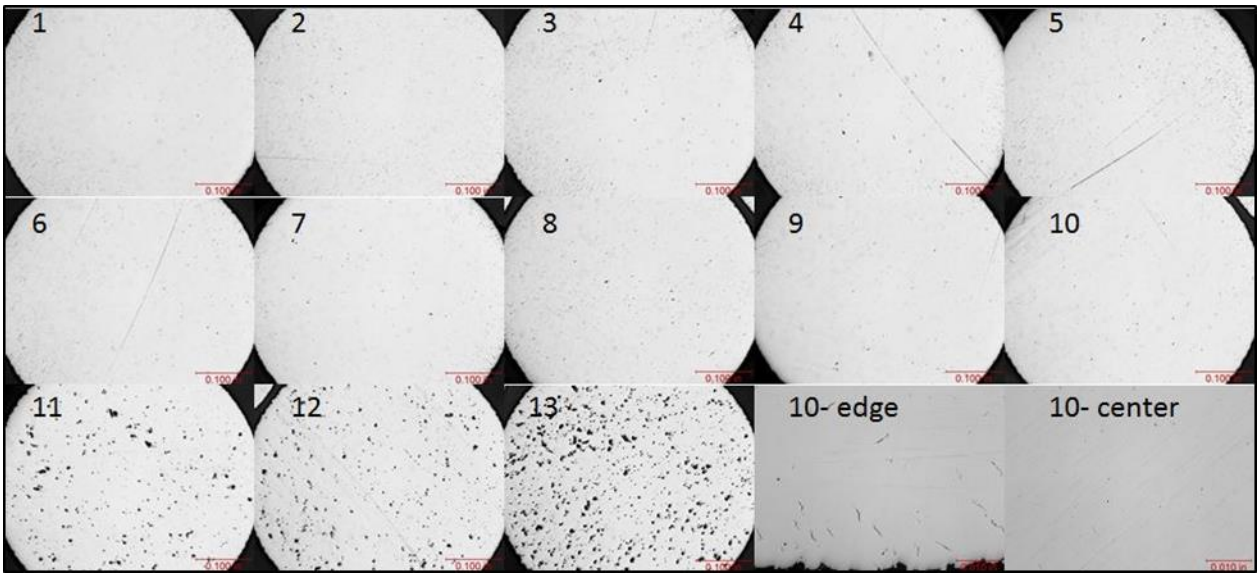

Figure 37. Cross-sectional Macroscopic Images of the Cylindrical Specimens Produced with the S2-F Powder (Specimens 1 and 13 had the highest and lowest laser powers, respectively)

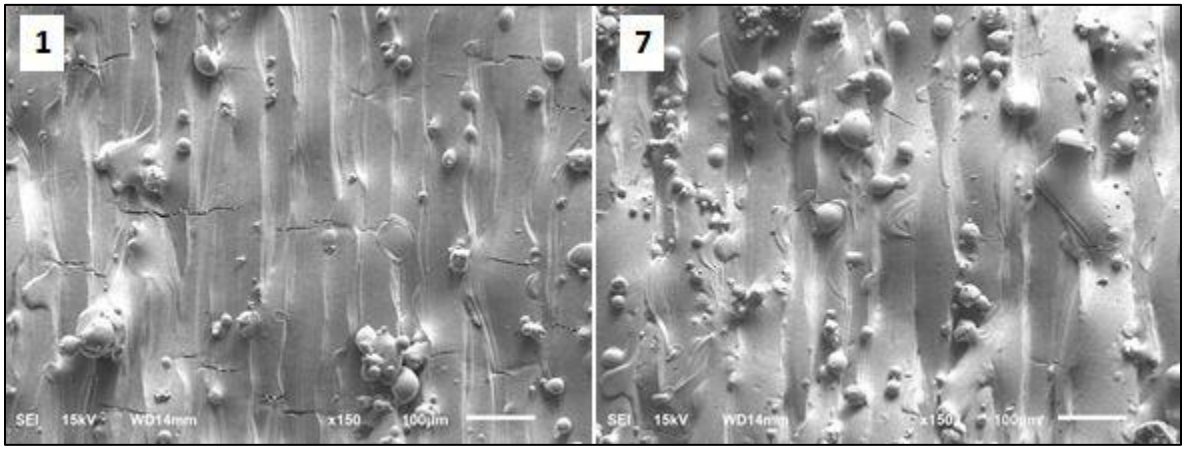

Figure 38. Influence of Laser Power on the Tendency for Cracking in the S2-F Powder (Specimens 1 and 7 were produced using the laser power of 390 and 290 W, respectively)

With this being resolved, it was possible to move forward to producing specimens for mechanical testing. Noting that, parameters between Samples 10 and 11 were used to produce the test walls for Task 2.0.

However, this processing window was considered too small for a robust commercial process. Options to improve the processing window were proposed (in-depth parameter development, HIP, chemistry changes); however, they were considered out of scope for this project.

3.2.2 Mechanical Testing Using the ASTM E08-09 Tensile Specimens

The ASTM E8-09 Specimen 3 was used as the design for mechanical testing specimens, with a reduced length of 1.25 in. (Figure 39).

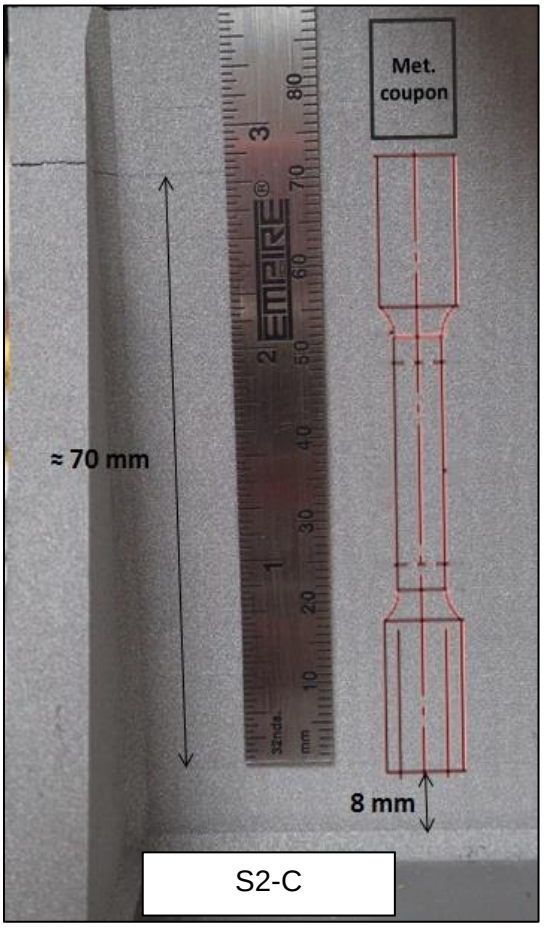

Figure 39. Layout for EDM Cut of Mechanical Testing Specimens, per ASTM E8-09, Specimen 33.2.2.1 Room Temperature Tensile Test

The room temperature tensile tests were conducted at EWI. Specimens with the gage diameter of 0.25 in. and gage length of 1 in. were machined from the mechanical test walls, per the ASTM E8-09 standard. The extension rate (crosshead speed) was set at 0.05 in./min. Three specimens were prepared and tested from each of the four powders. All specimens broke inside the gage area.

The results of the room temperature tensile test for all the four materials are summarized in Table 13. The minimum tensile requirements for investment cast Hastelloy X (per AMS 5390) are presented in the last row of Table 13. The ultimate tensile strength (Avg. UTS), 0.2% yield strength (Avg. YS), elongation (Avg. El%), and reduction in area (Avg. RA%) were plotted in Figure 40. The dashed lines on the plots indicate the minimum requirements per AMS 5390. Figure 41 shows the average values of the measured properties. On average, the S2

specimens had slightly lower yield strength and higher elongation and reduction of area, compared to those of the S1 materials.

All specimens produced with the four powders met the tensile requirements of AMS 5390, except one of the S2-C specimens (S2-C-3), with an elongation slightly less than the requirement. It should be noted that the AMS5390 specification is for the investment cast Ni Alloy X material and the comparison to the AM material is only for reference.

Table 13. Summary of the Results of the Room Temperature Tensile Test for S1-F and S1-C Specimens

Sample ID	Test Temp. (°F)	Avg. UTS		Avg. YS		Avg. El (%)	Avg. RA (%)
		MPa	ksi	MPa	ksi		
S1-C-1	23	768.8	111.5	432.3	62.7	24.1	24.8
S1-C-2	23	689.5	100.0	449.5	65.2	15.3	18.2
S1-C-3	23	778.4	112.9	433.0	62.8	33.2	24.8
S1-F-1	23	790.8	114.7	426.1	61.8	17.2	16.8
S1-F-2	23	800.5	116.1	411.6	59.7	21.4	20.5
S1-F-3	23	797.0	115.6	431.6	62.6	20.2	20.4
S2-C-1	23	779.1	113.0	340.6	49.4	26.0	30.2
S2-C-2	23	826.7	119.9	338.5	49.1	31.1	28.2
S2-C-3	23	548.1	79.5	319.9	46.4	7.3	12.9
S2-F-1	23	791.5	114.8	350.9	50.9	31.2	27.1
S2-F-2	23	793.6	115.1	349.6	50.7	30.8	28.5
S2-F-3	23	790.8	114.7	342.0	49.6	35.9	34.9
Reference AMS5390 Investment Cast Ni Alloy X Specification Requirements		241.0	35.0	379.0	55.0	8.0	Not rated

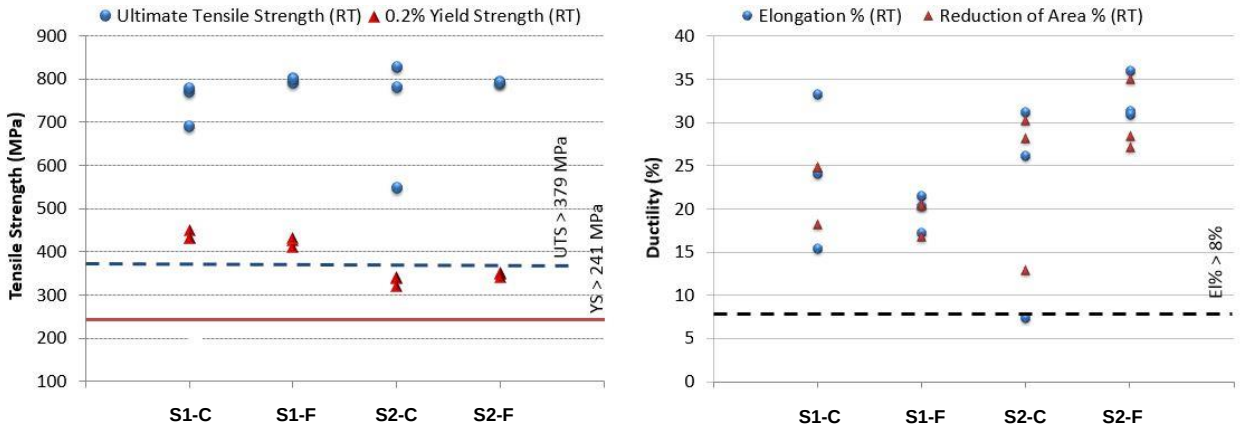

Figure 40. Room Temperature Tensile Data Points of the Specimens Produced with S1 and S2 Powders

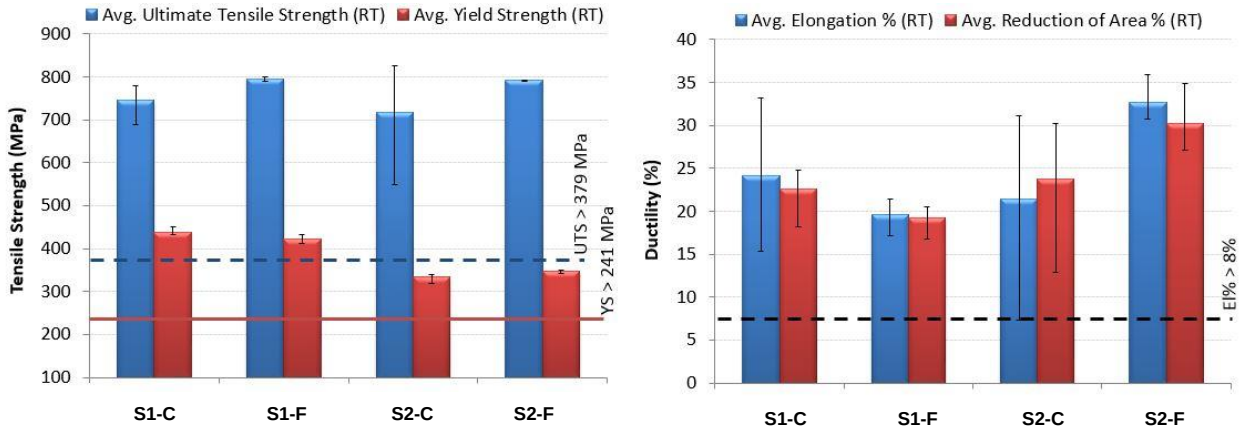

Figure 41. Average Room Temperature Tensile Properties of the Specimens Produced with S1 and S2 Powders

Figure 42 compares the SEM analysis of the fracture surfaces of the S1-F and S1-C tensile specimens tested at room temperature. Both specimens displayed rough, intergranular fracture morphology. Both specimens displayed a rough fracture surface with an intergranular morphology. Un-melted powder particles were observed on the fracture surfaces of both materials.

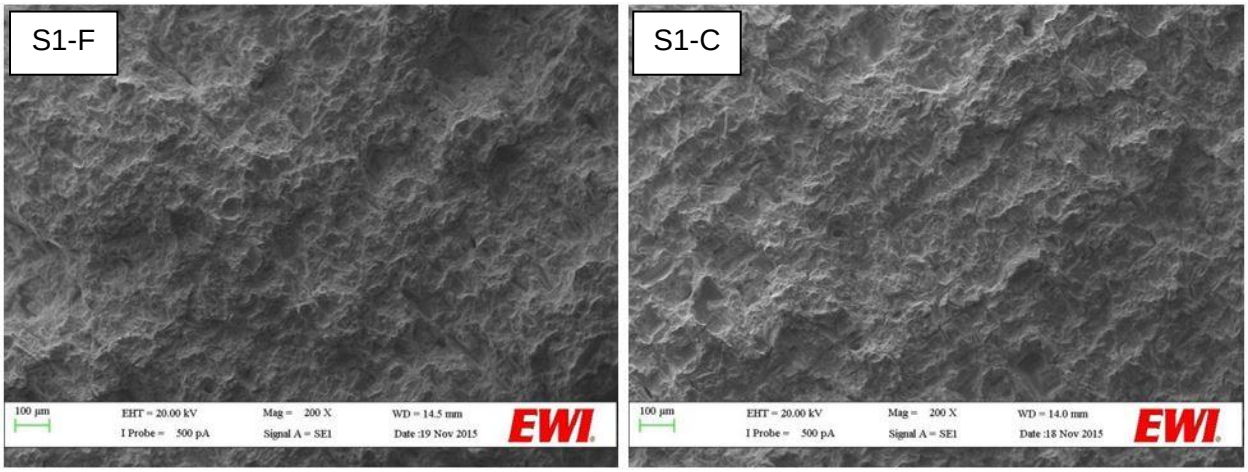

Figure 42. Representative SEM Images of S1-F (left) **and S1-C** (right) **Tensile Specimens Tested at Toom Temperature**

At a higher magnification, the formation of dimples on the fracture surfaces are obvious, which is an indication of the ductile fracture (Figure 42). Secondary cracking, indicated by arrows in Figure 43, occurred prior to the final separation. Also evident was the formation of dimples on the fracture surface, as an indication of ductile fracture. In addition, secondary cracking formed on the surface prior to the final fracture, indicated by the arrows.

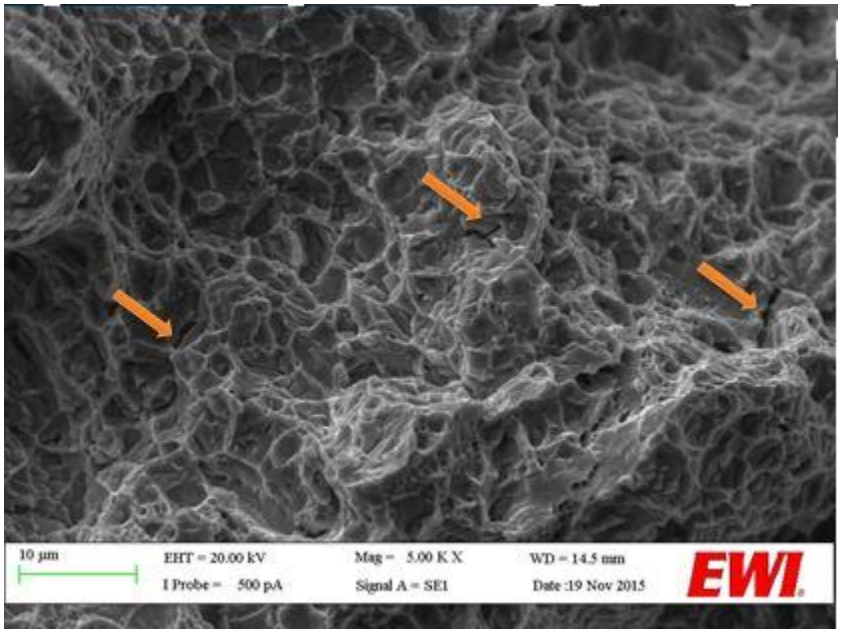

Figure 43. Representative SEM Images of a S1-F Tensile Specimen Tested at Room Temperature

Discrete and irregular areas displaying a smooth surface were observed on the fracture surfaces of both materials (Figure 44). These areas were mostly surrounded by un-melted powder particles (left image). The un-melted zones, known as the lack of fusion (LOF), are

typical to the powder-bed fusion (PBF) AM processes. The formation of dimples is the identical feature on fracture surfaces of both materials (right image).

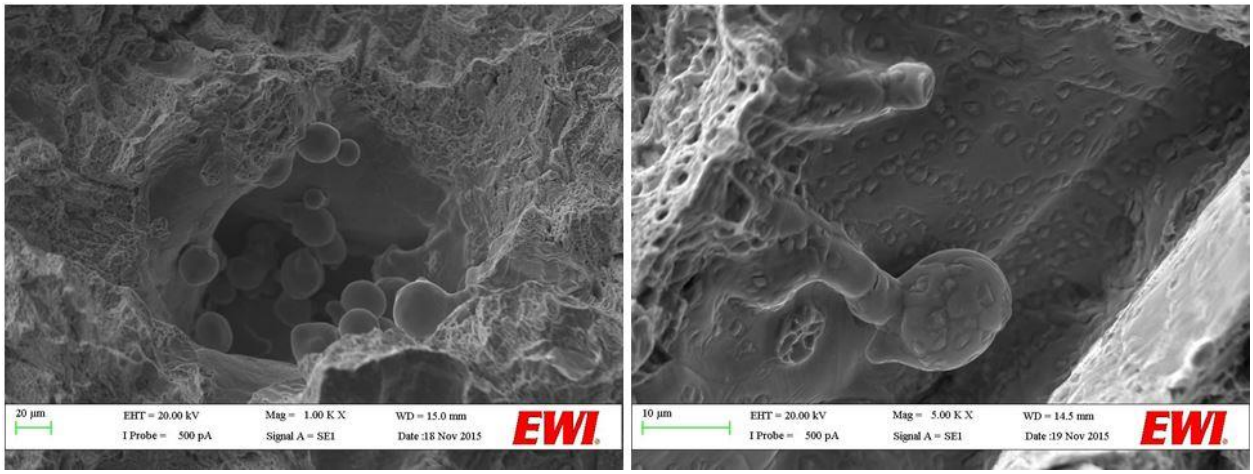

Figure 44. Areas with Smooth Surfaces on SEM Image of S1-F Tensile Specimen

Precipitates were observed on the fracture surfaces of both materials (Figure 45). Almost all precipitates had a bulky morphology. Some precipitates split under the tensile loading, which could be an indication of their brittleness. The split precipitates are indicated using dark arrows in Figure 45. The EDS analysis was conducted to compare the chemical composition of the precipitates and substrates. The red-dotted circles in Figure 45 show the sampling area used for the EDS analysis. The blue circles show the sampling areas for the base metal metrics. A summary of the results is presented in Table 15.

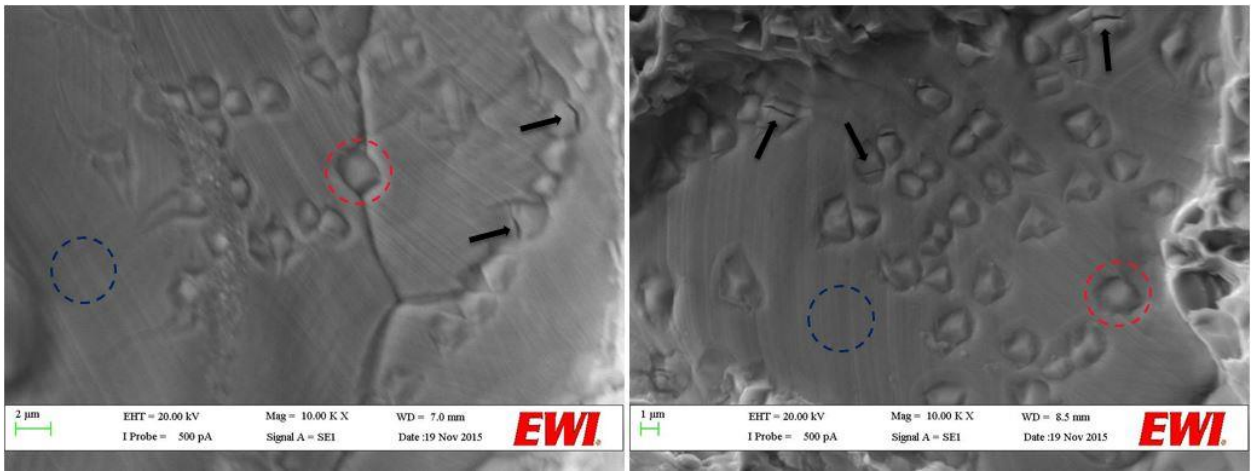

Figure 45. Precipitates Observed on Room Temperature Tensile Fracture Surfaces

In addition to the results of the EDS analysis, the chemical composition of substrates measured using the ICP/LECO methods are presented in Table 14 for comparison purposes. Results of the EDS analyses of the substrates closely matched with those of the ICP/LECO testing.

Table 14. Chemical Composition of Substrates and Precipitates on Radiographic Testing (RT) Tensile Fracture Surface of S1 Buildups

	S1-C (wt-%)			S1-F (wt-%)		
	ICP/LECO	EDS*		ICP/LECO	EDS*	
Element	Substrate		Precipitate	Substrate		Precipitate
Carbon	0.03	5.59	15.51	0.05	11.16	17.01
Chromium	20.88	20.7	15.44	21.44	19.38	15.97
Cobalt	1.54	1.4	0.58	1.65	1.44	0.84
Iron	19.72	18.4	4.46	19.12	17.36	8.2
Manganese	0.83	0.8	0.37	0.85	0.79	0.39
Molybdenum	9.64	8.14	34.33	9.4	8.89	25.99
Nickel	45.4	43.61	22.33	45.48	39.21	25.88
Silicon	0.82	0.61	4.82	0.88	0.84	3.86
Tungsten	0.81	0.75	2.16	0.77	0.94	1.87

**EDS results are semi-quantitative and standard-less.*

In comparison to the substrates, the precipitates in both materials contained considerably higher percentages of carbon and molybdenum. Also, a notable decrease of iron and nickel was observed in the precipitates. Other elements, such as silicon and tungsten, showed a slight increase in the precipitates, while chromium and cobalt slightly decreased.

The fracture analysis of the S1-C and S1-F tensile specimens tested at elevated temperature was conducted using SEM. Prior to the testing, specimens were cleaned in an ultrasonic cleaner for 15 minutes using Alconox solution. Methanol was used in a following cleaning step.

Figure 46 shows representative images of the fracture surfaces in the specimens. Features on the fracture surfaces of elevated temperature tensile specimens were almost identical to those of the room temperature tensile specimens. SEM evaluation of the fracture surface revealed rough, intergranular fracture morphology for both materials. Identical features were observed on the fracture surfaces of both materials, including secondary cracking and LOF, surrounded by un-melted powder particles.

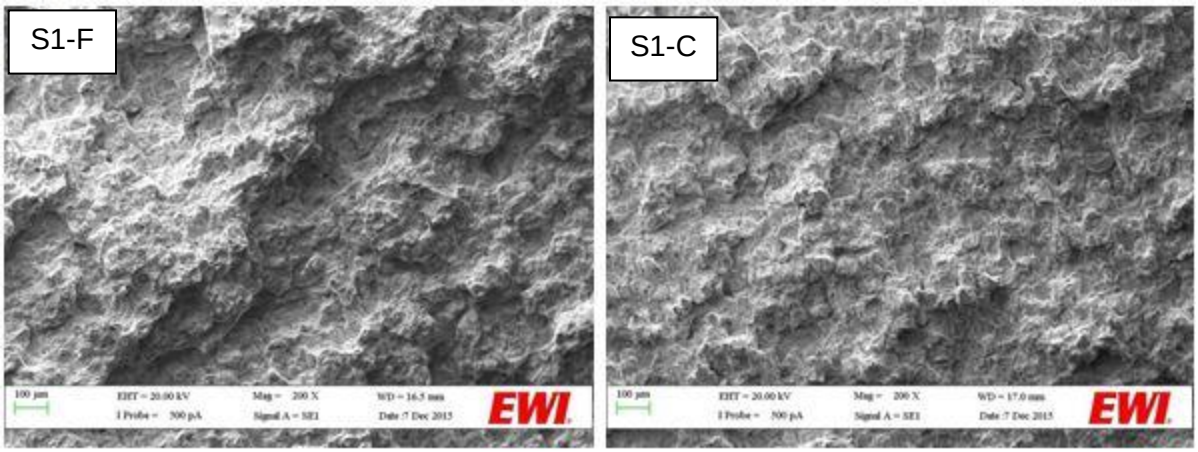

Figure 46. Representative SEM Images of S1-F (left) **and S1-C** (right) **tensile specimens tested at 1500°F** (Both showing rough, intergranular fracture morphology; un-melted powder particles were observed on the fracture surfaces of both materials)

3.2.2.2 Elevated Temperature Tensile Test

The elevated temperature tensile test was conducted by EWI through Element Material Technology. Three tensile specimens were prepared for any of the S2 powders, per the ASTM E8-09 standard. The test was conducted per ASTM E21, at 1500°F (815.5°C), after 20 minutes of soak time. All specimens failed inside the gage area.

The results of the elevated temperature tensile test for all specimens are summarized in Table 15. Figures 47 and 48 illustrate the data points and average properties of the four materials. In comparison to the S1 specimens, the S2 specimens showed a slightly lower strength and higher elongation and reduction of area. Two of the S1-F specimens (S1-F-1 and S1-F-3) showed elongation lower than the minimum requirement of the AMS 5390 standard.

Table 15. Mechanical Properties of AM S1 and S2 Materials at Elevated Temperature

Sample ID	Test Temp. (°F)	Avg. YS		Avg. UTS		Avg. El (%)	Avg. RA (%)
		MPa	ksi	MPa	ksi		
S1-C-1	1500	248.2	36.0	317.2	46.0	23.5	19.5
S1-C-2	1500	251.7	36.5	310.3	45.0	16.0	18.0
S1-C-3	1500	258.6	37.5	313.7	45.5	18.0	22.0
S1-F-1	1500	248.2	36.0	306.8	44.5	11.0	14.0
S1-F-2	1500	251.7	36.5	306.8	44.5	12.0	12.0
S1-F-3	1500	234.4	34.0	306.8	44.5	11.0	10.0
S2-C-1	1500	196.5	28.5	296.5	43.0	37.5	33.5
S2-C-2	1500	196.5	28.5	296.5	43.0	39.0	34.0

Sample ID	Test Temp. (°F)	Avg. YS		Avg. UTS		Avg. El (%)	Avg. RA (%)
		MPa	ksi	MPa	ksi		
S2-C-3	1500	196.5	28.5	296.5	43.0	39.5	39.5
S2-F-1	1500	203.4	29.5	299.9	43.5	27.0	27.0
S2-F-2	1500	203.4	29.5	299.9	43.5	25.0	25.0
S2-F-3	1500	199.9	29.0	299.9	43.5	25.5	25.5
Reference AMS5390 Investment Cast Ni Alloy X Specification Requirements		241.0	35.0	n/r	n/r	12.0	Not rated

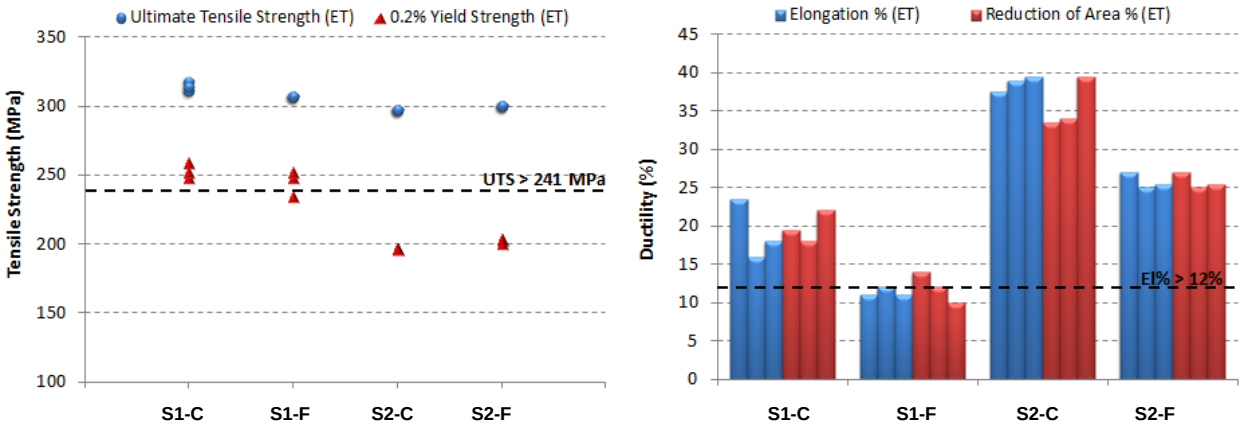

Figure 47. Elevated Temperature Tensile Data Points of the Specimens Produced with S1 and S2 Powders

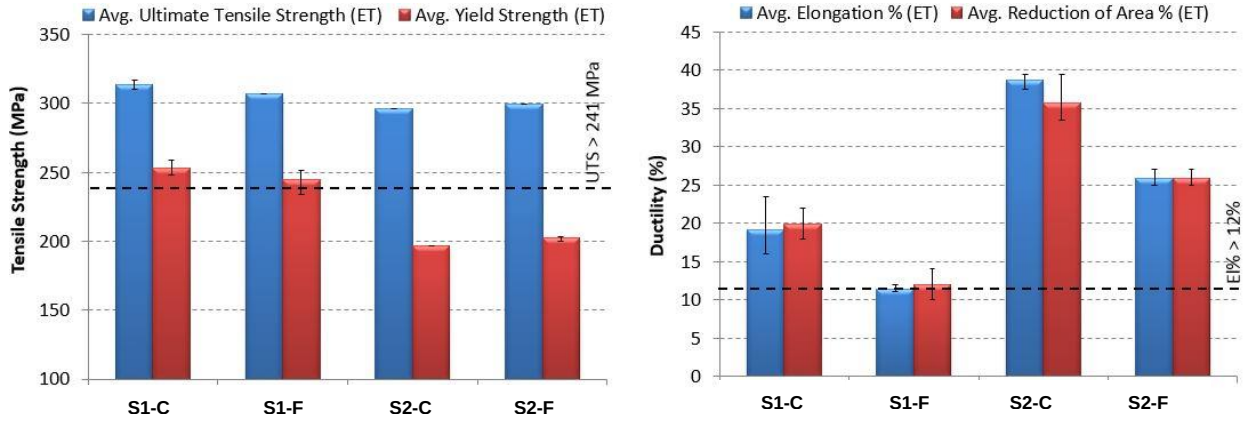

Figure 48. Average Elevated Temperature Tensile Results of the Specimens Produced with the S1 and S2 Powders

3.2.2.3 Low Cycle Fatigue.

The LCF test was conducted by Solar through a subcontractor. Three specimens with a gage diameter of 0.25 in. were tested for any of the S2 powders. A sinusoidal waveform was used at the test temperature of 1000°F (537.8°C). Total strain range and stress ratio were set at 0.6% and -1, respectively.

The results of the LCF test for all specimens are summarized in Table 16. Figure 49 shows the number of cycles and the average cycles prior to failure for any of the four materials. On average, the specimens produced with the S1 powders showed a slightly longer life under the cyclic loading. S1-F and S2-F materials displayed a relatively higher average life cycle compared to those of the S1-C and S2-C materials. The S2-C material showed the minimum fatigue life.

The fine powders provided by the two suppliers showed higher life cycles than those of the coarse powders.

Table 16. LCF Properties of AM Nickel Alloy X Material Produced with S1 and S2 Powders

Sample ID	Test Temp. (°F)	Total Strain Range (%)	Cycles to Failure
S1-C-1	1000	0.6	1820
S1-C-2	1000	0.6	2576
S1-C-3	1000	0.6	3451
S1-F-1	1000	0.6	4713
S1-F-2	1000	0.6	5855
S1-F-3	1000	0.6	3680
S2-C-1	1000	0.6	1881
S2-C-2	1000	0.6	2153
S2-C-3	1000	0.6	1185
S2-F-1	1000	0.6	3341
S2-F-2	1000	0.6	4483
S2-F-3	1000	0.6	5423

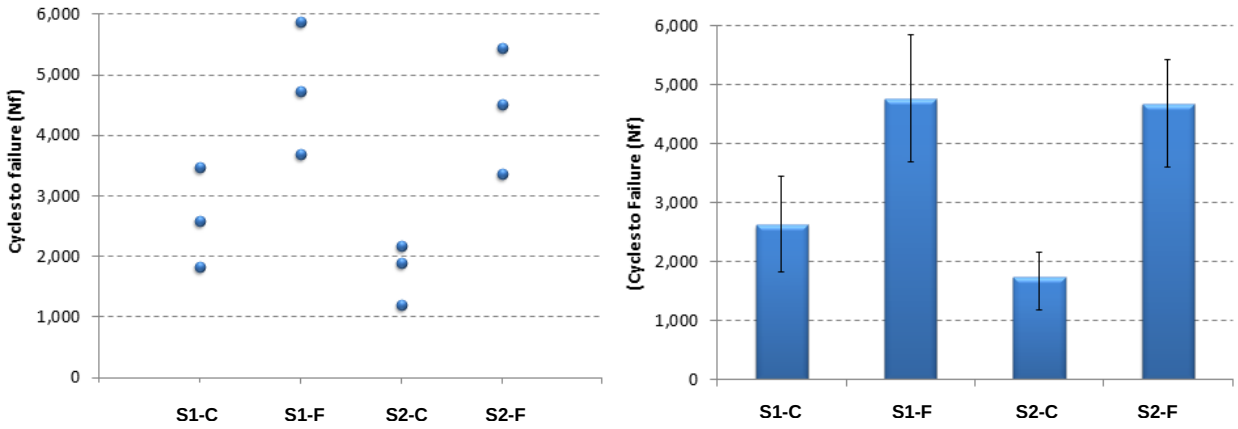

Figure 49. LCF Test Results of S1 and S2 Specimens Conducted at 1000°F

The better performance of the finer materials could be explained by the effect of powder size distribution on the packing density of a powder bed. The presence of a fine powder particle could increase the packing density of the powder bed. As a result, a part with fewer un-sintered zones or LOFs could be produced. Fewer LOFs could result in the higher fatigue life of the specimens produced with the S2-F and S1-F powders. However, it should be noted that strength of a material is another major factor that influences the performance of a material under LCF testing. Therefore, flaws might have less influence on the LCF performance of a material than on the high cycle fatigue (HCF) performance of a material.

Figure 50 compares the stereo-microscope images of the fractured LCF specimens. The fracture initiation sites could be distinguished with their relatively darker coloration. The samples built with the finer powders displayed multiple initiation sites (six to eight sites) and consequently, the fracture occurred on multiple planes associated with each initiation. The samples produced with the coarse powders displayed relatively fewer initiation sites (one to three) and the overall fracture occurred on a single plane.

In Figure 50, red arrows show relatively darker coloration at the fracture initiation sites. The fracture surfaces of the fine powders provided by both suppliers displayed multiple initiation sites and occurred on multiple planes. In contrast, the fracture surfaces of the coarse powders displayed less initiation sites and occurred relatively on one plane.

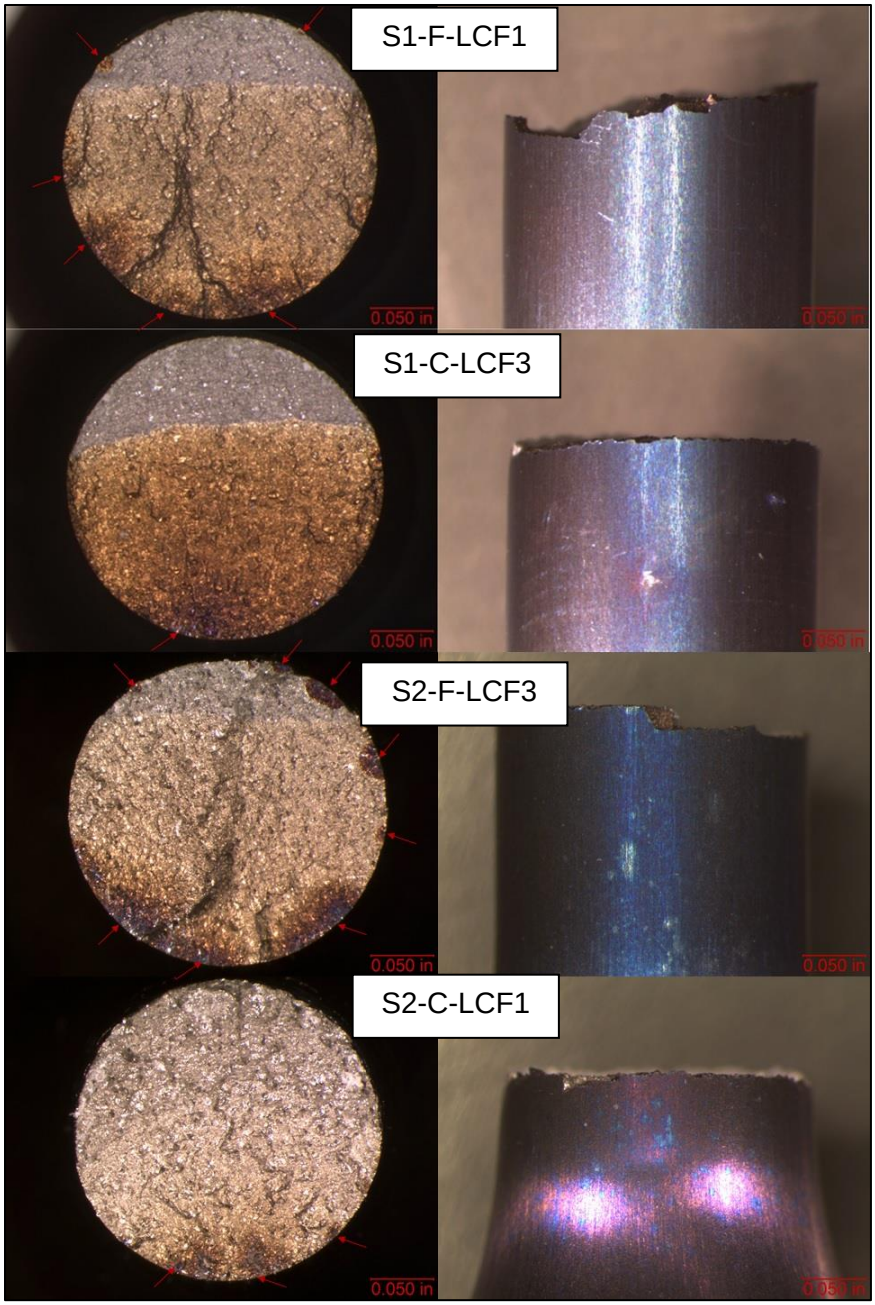

Figure 50. Representative Stereo Microscope Images of AM Materials Tested at 1000°F

Similar to the results of fractography on tensile specimens, SEM evaluation of the initiation sites of all materials revealed the presence of discrete, irregular sites of LOF. Figure 51 compares the crack initiation sites in the four materials. On average, the coarse powders from the two suppliers showed larger areas of LOF. The fracture surface surrounding the areas of LOF displayed a transgranular morphology with river marks emanating away from the LOF (Figure 51). Each image shows the presence of un-melted powder particles and smooth surfaces typical

of LOF produced during the AM build. The coarse powders from both suppliers showed a significantly larger area of LOF compared to the initiation sites of the fine powder.

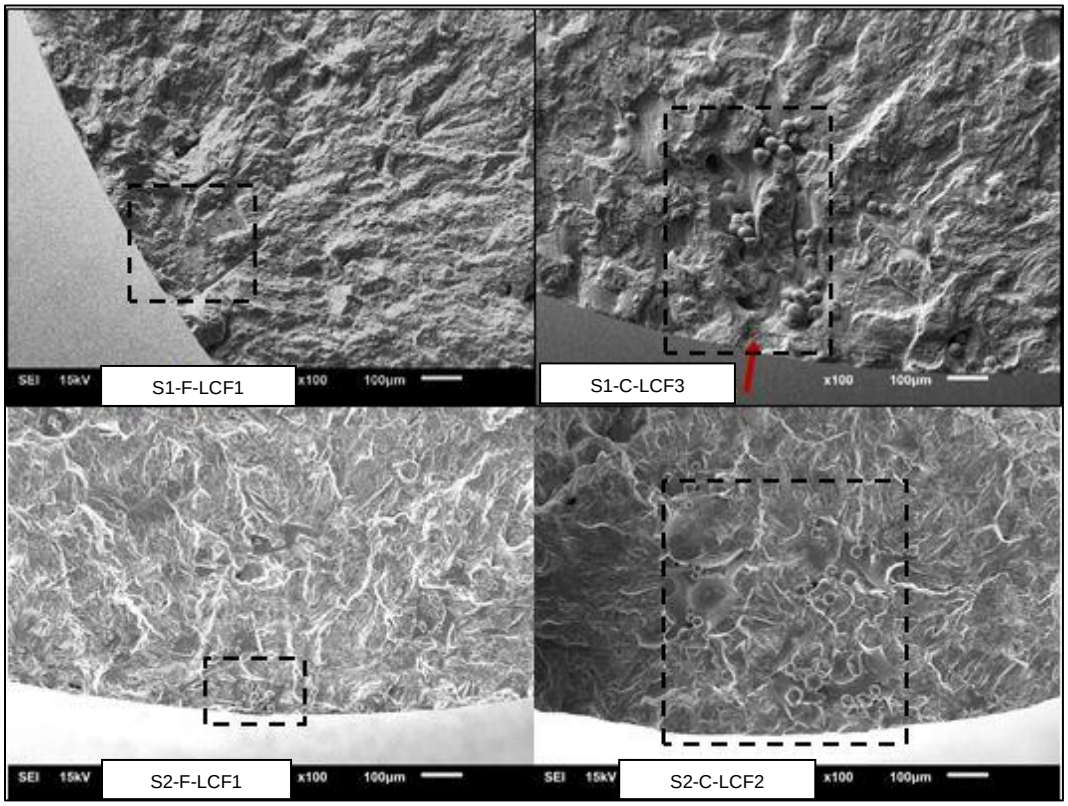

Figure 51. SEM Images of Crack Initiation Sites of the Materials Tested at 1000°F

Away from the initiation sites, the fracture surface displayed fine striations space approximately 1-2 µm apart, typical of stable LCF crack propagation (Figure 52).

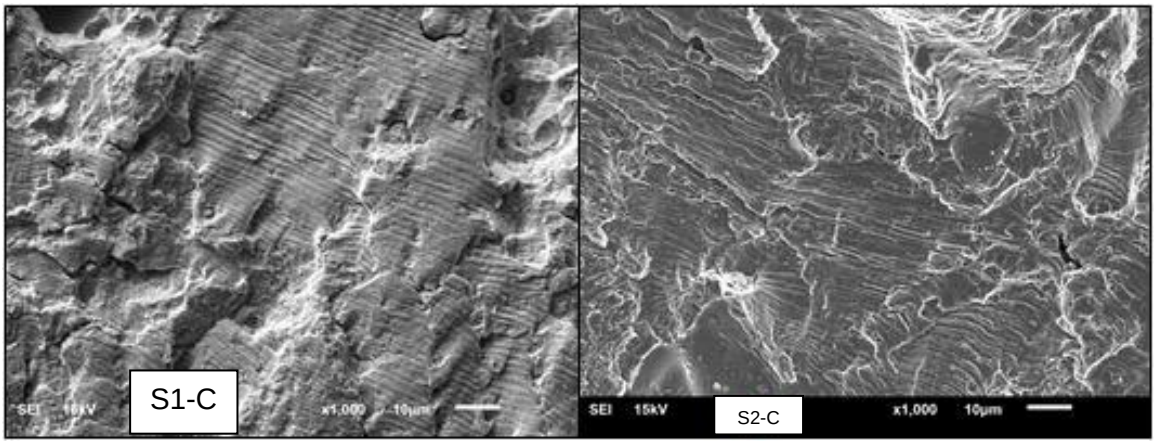

Figure 52. SEM Image of the S1-C and S2-C LCF Test Specimen Fracture Surface

3.2.2.4 Creep

The creep test was conducted at Solar through Joliet Metallurgical Laboratory. Three specimens of each of the S2 powders were tested at 1500°F (815.5°C), under a 15-ksi stress. The results of the creep test for specimens produced with the four powders are summarized in Table17. The AMS 5390 standard does not provide any requirements for the elevated temperature creep properties of Hastelloy X. Two other standards, including AMS 5536 and AMS 5754, were used for the comparison purposes.

Table 17. Creep Rupture Properties of AM Nickel Alloy X Material Produced with S1 and S2 Powders

Sample ID	Test Temp. (°F)	Test Stress (ksi)	Hours to Rupture	Elongation at Rupture (%)
S1-C-1	1500	15	34.6	6.0
S1-C-2	1500	15	36.6	5.1
S1-C-3	1500	15	35.2	6.7
S1-F-1	1500	15	22.7	6.8
S1-F-2	1500	15	20.8	6.1
S1-F-3	1500	15	20.8	5.2
S2-C-1	1500	15	38.8	15.9
S2-C-2	1500	15	58.6	16.7
S2-C-3	1500	15	38.8	16.9
S2-F-1	1500	15	35.6	13.8
S2-F-2	1500	15	35.8	13.0
S2-F-3	1500	15	40.3	13.6
Reference AMS 5390 Cast Ni Alloy X Specification Requirements	n/a	n/a	n/a	n/a
Reference AMS 5536 Sheet/Strip/Plate Specification Requirements	1500	16	15-24	3-8
Reference AMS 5754 Bar/Forging/Ring Specification Requirements	1500	15	24	10

The life time, elongation, and reduction of area of the specimens are plotted in Figure 53. Figure 54 compares the average results of the creep test. In general, specimens produced with the S2 powders showed a longer rupture time. The S2-C and S1-F materials showed the longest and shortest rupture time, respectively. Also, like the results of tensile testing, the S2 materials showed a significantly higher ductility, in comparison to the S1 materials.

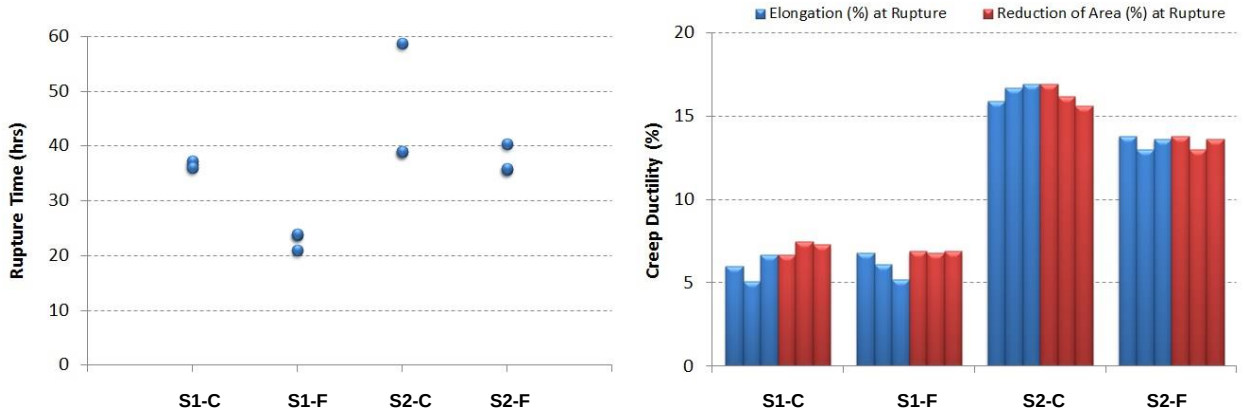

Figure 53. Creep Test Data Points of the Specimens Produced with the S1 and S2 Powders

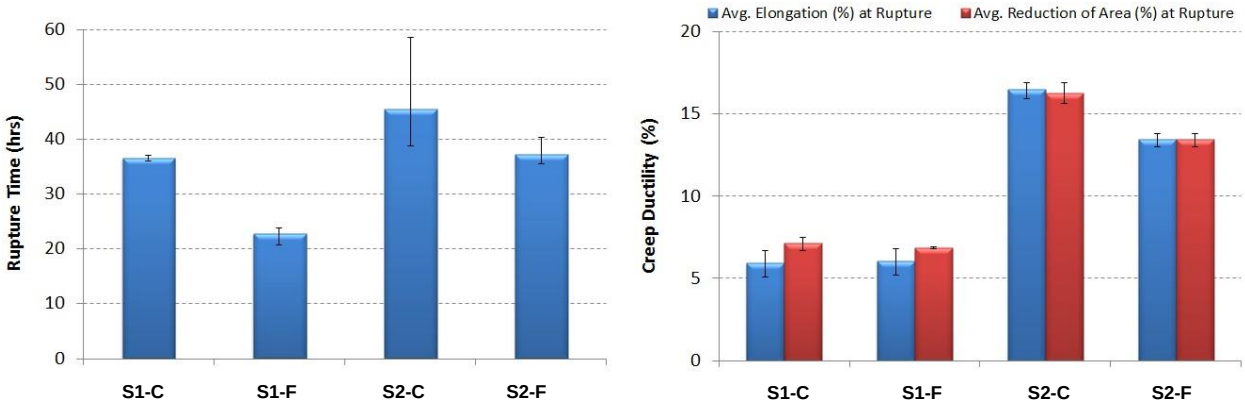

Figure 54. Average Results of the Creep Test of the Specimens Produced with the S1 and S2 Powders

3.2.2.5 Down Selection of Powders

AM of any material, metal, plastic, or ceramic, is similar to the manufacture of composites in that the material is being produced while the part is being produced. This introduces the potential for considerable variability, unless precise materials and process controls are employed to offer a wide, predictable materials process window to achieve reproducible performance.

3.2.2.5.1 Microstructure and Composition. Many factors play a role in selection of the right material. The preliminary microstructure analysis was conducted to provide evidence for the mechanical performance of the four materials. Figures 55 and 56 compare the microstructures of the four materials. In Figure 56, the S1-F material displayed a relatively smaller grain size and significantly more intra-granular precipitates.

In Figure 56, the images show the presence of fine intra-granular precipitates and coarse-grain boundary precipitates in the S1-F powder. The other three powders displayed coarse intragranular precipitates in addition to coarse-grain boundary precipitates. The finer grain size and the precipitates made the S1-F material the most resistant material to transgranular fatigue crack propagation. Conversely, the lowest ductility under the elevated temperature tensile test and creep was recorded in the S1-F material.

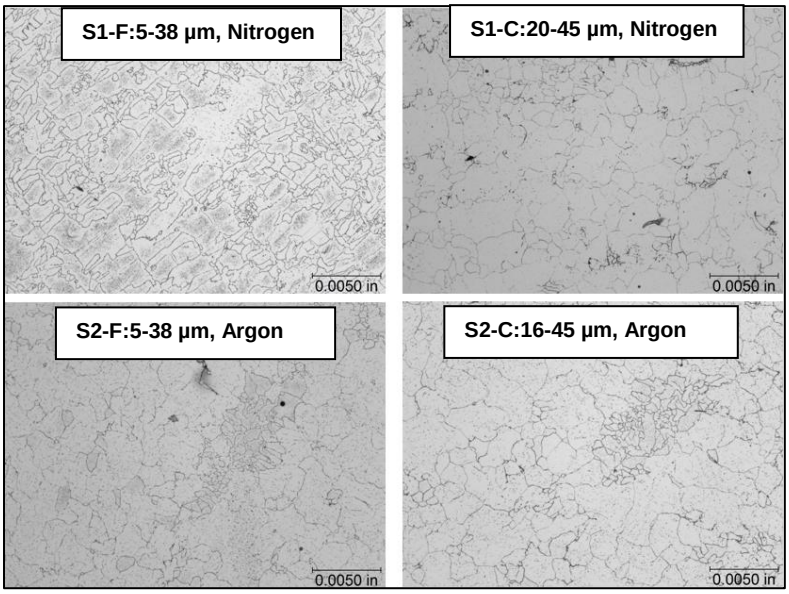

Figure 55. Optical Micro Images of Heat-treated (2150°F/Hour) AM Nickel Alloy X Material Produced with the Four Candidate Powders (images show minimal grain growth for the S1-F powder in contrast to the significant grain growth for the other three powders)

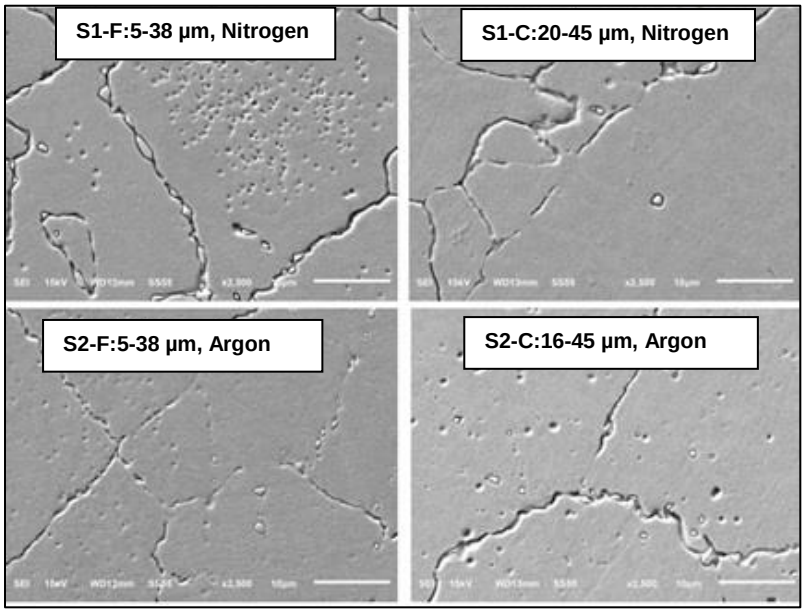

Figure 56. SEM Micro Images of Heat-treated (2150°F/Hour) AM Nickel Alloy X Material Produced with the Four Candidate Powders

The higher strength and lower ductility of the S1-F specimens under tensile and creep testing could be related to the difference in chemical composition of powders provided by the two suppliers. Table 18 compares the chemical composition of the four powders and buildups. The two S1 powders had significantly higher contents of manganese and silicon and slightly less tungsten and iron than the S2 powders.

Another potential influencing factor on mechanical performance of materials could be the type of inert gas used for the powder atomization. The S1 and S2 powders were produced using nitrogen and argon, respectively. A similar trend was observed in a separate study conducted by the Additive Manufacturing Consortium (AMC) at EWI. Between the two sets of Inconel 718 specimens produced with L-PBF processes, specimens atomized with nitrogen showed a lower ductility and a higher level of precipitation. Because both Hastelloy X and Inconel 718 are Ni-based alloys, there could be some similarities in the influence of an atomizing gas on microstructural characteristics of Ni-based alloys.

Table 18. Comparison of the Chemical Compositions of the Four Powders and the Four Buildups

Element	S1-F		S1-C		S2-F		S2-C	
	Powder	Build*	Powder	Build*	Powder	Build*	Powder	Build*
Aluminum	---	0.02	---	0.01	0.02	0.04	0.03	0.04
Boron	---	0.002	---	0.003	0.004	0.007	0.005	0.007
Carbon (total)	0.03	0.05	0.03	0.03	0.1	0.10	0.05	0.10
Cobalt	1.54	1.65	1.43	1.54	1.57	1.70	1.49	1.69
Chromium	20.5	21.44	20.8	20.88	22.12	21.68	21.57	21.73
Copper	---	0.14	---	0.14	---	0.12	---	0.12
Iron	19.2	19.12	19.8	19.72	17.33	16.35	18.14	17.00
Hydrogen	---	0.0003	---	0.0003	0.001	0.0001	---	0.0002
Manganese	0.89	0.85	0.86	0.83	0.04	0.03	0.14	0.10
Molybdenum	8.8	9.40	8	9.64	8.85	9.61	8.86	9.60
Nitrogen	---	0.10	0.11	0.10	0.01	0.02	0.01	0.01
Nickel	Balance	Balance	Balance	Balance	Balance	Balance	Balance	Balance
Oxygen	---	0.05	0.08	0.06	0.02	0.02	0.02	0.02
Phosphorous	0.011	0.021	0.01	0.015	<0.005	0.008	<0.005	0.010
Sulfur	0.004	0.006	0.005	0.005	0.002	0.004	0.002	0.004
Silicon	0.85	0.88	0.8	0.82	0.1	< 0.01	0.11	0.14
Titanium	---	0.02	---	< 0.01	---	< 0.01	---	0.01
Tungsten	0.68	0.77	0.69	0.81	0.97	1.13	0.71	1.09

**Analysis by LECO combustion, ASTM E 1019 (C, S), SOP 10.08 (O, N), SOP 10.09 (H), ICP per SOP 10.30 (all the elements*).

The chemical analysis of the powder, as well as the modeling carried out using the JMatPro software, indicated differences between the powders produced by the two suppliers. The two powders from S2 had significantly lower amounts of Mn and Si and a higher W, which could contribute to cracking. This necessitated development of separate processing parameters for the S2 powders.

3.2.2.5.2 Overall Mechanical Performance and Component Integrity. Process parameter optimization trials were conducted for the two S2 powders; however, results showed that within the range evaluated, the L-PBF of both S2 powders was accompanied by micro-cracking. In addition to cracking, the S2-C powder had a poor compatibility with the ProX300. The free flowing S2-C powder leaked past the seals and resulted in short feeds. The S1-C powder also displayed similar behavior, but to a lesser extent. Therefore, the S2-C powder was eliminated from further analysis. The second round of process optimization was conducted on the S2-F powder to eliminate cracking. Although the cracking tendency slightly decreased, with an increase in the hatch spacing from 50 to 60 µm, there did not appear to be an obvious

processing window between the onset of cracking and porosity. Therefore, focus settled on the S1-F powder.

3.2.2.6 Overall Suitability of Mechanical Performance

Per the requirements of AMS 5390, all materials had acceptable performances under the room and elevated temperature tensile testing. S1-F powder was the only material that showed a slightly lower ductility at the elevated temperature. It should be noted that the application of a proper heat treatment could improve the ductility of these materials.

Both S1 powders showed an almost similar creep performance, but the S1-F powder had a considerably longer fatigue life. Similarly, the two S2 powders performed almost identical under the creep testing. However, the S2-F powder had an average longer fatigue life.

Because the high-temperature fatigue performance of Hastelloy X is critical for the fuel injector application, the S1-F powder was selected for further analysis in Task 3. Powder comparisons are presented in Table 19.

Table 19. Comparison of the Cost and Mechanical Performance of Materials Produced with the S1 and S2 Powders

Powder/ Properties	Cost Comparison	Powder Compatibility with AM Machine (ProX300)	Microstructure (Micro cracks)	RT Tensile Test			ET Tensile Test		Creep		Fatigue
				UTS	YS	El%	UTS	El%	Hrs (rpt.)	El% (rpt.)	Cycles
S1-C	100%										
S1-F	132%							No HT			
S2-C	190%										
S2-F	195%										

Hrs: Hours; rpt: rupture

3.2.3 Dimensional Accuracy – Fuel Injector Feature Specimens

Two custom designs were introduced to examine issues specific to producing an actual fuel injector device. The types, sizes, and orientations of features in the original design of the fuel injector were used to develop the design of the coupons.

3.2.3.1 Angled Throat Sections

Figure 57 shows specimens produced with the S1-F powder. Three inclination angles of 0, 20, and 45 degrees were used to reproduce the actual complexity of the fuel injector design.

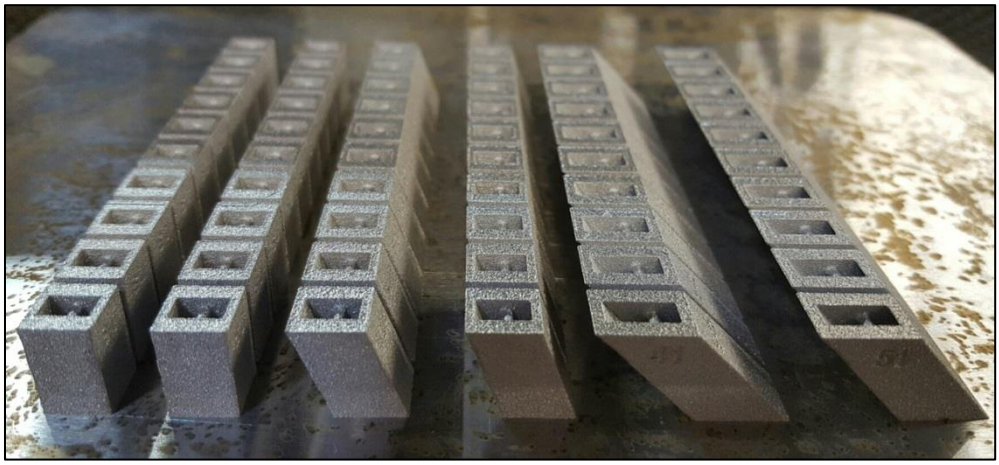

Figure 57. Specimens Produced with Three Inclination Angles of 0, 20, and 45 Degrees for the Analysis of Surface Roughness and Dimensional Accuracy (two each, left to right)

Figure 58 illustrates the results of surface roughness measurements for the S1-F samples. All three inclination angles showed a lower surface roughness on the top surfaces, compared to the bottom surface. This could be explained by the stair-stepping effect associated with the slicing of the 3D design and the layer-by-layer fabrication of the specimens. On the top surface of the 0-degree specimen, no stair-stepping effect is active, which resulted in the minimum surface roughness. The 45-degree specimen has wider steps, compared to those of the 20-degree specimen, which resulted in the lower surface roughness on the top surface of the 45-degree specimen. However, the wider steps had an opposite influence on the surface roughness of the downward-facing surfaces. Because downward-facing surfaces are only supported by loose powders, more severe material dropping is expected to occur on surfaces with the higher inclination angles (and larger steps).

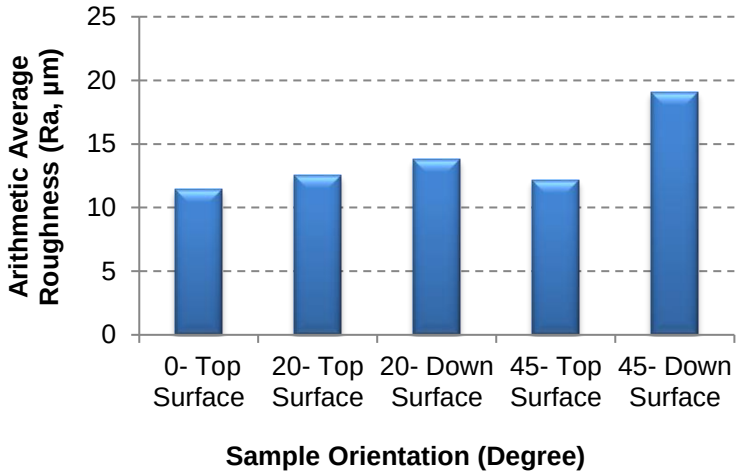

Figure 58. Results of Surface Roughness Measurement from S1-F Specimens Produced with the Nominal Process Parameters

3.2.3.2 Dimensional Accuracy Specimens – Holes and Complex Openings

New designs were developed to minimize and control material dropping (i.e., “print through”) on overhanging surfaces, which leads to dimensional inaccuracy. Three diamond-shaped features with the diagonal sizes of 0.03, 0.07, and 0.15 in. were printed at four different angles of 0, 30, 45, and 60 degrees (Figure 59).

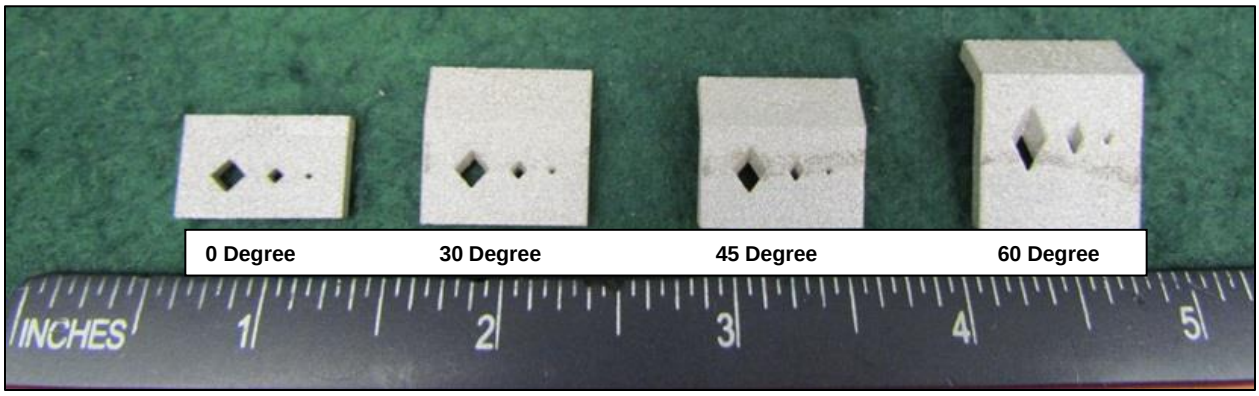

Figure 59. Four Specimens Designed for the Analysis of Dimensional Accuracy, Fabricated with the S1-F Powder

The influence of process parameters on dimensional accuracy of AM components was investigated. For this purpose, several features were produced with different sizes and various inclination angles, with the S1-F powder. Also, a DOE was developed, containing a wide range of laser powder, scanning speed, and hatch size. Table 20 contains the parameters used for this study.

Table 20. Combination of Process Parameters Designed for the Dimensional Accuracy Analysis

ID	DOE Category	Speed (mm/s)	Hatch Spacing (mm)	Power (W)
L1	L-S	1200	0.05	162
L2	L-S	1200	0.05	172
L3	L-S	1200	0.05	181
L4	L-S	1200	0.05	191
L5	L-S	1200	0.05	200
L6	L-S	1200	0.05	210
M1	M-S	1750	0.05	219
M2	M-S	1750	0.05	240
M3	M-S	1750	0.05	261
M4	M-S	1750	0.05	282

ID	DOE Category	Speed (mm/s)	Hatch Spacing (mm)	Power (W)
L7	L-H	1200	0.03	129
L8	L-H	1200	0.03	148
L9	L-H	1200	0.03	168
L10	H-H	1200	0.09	228
L11	H-H	1200	0.09	262
L12	H-H	1200	0.09	296
M7	L-H	1750	0.03	175
M8	L-H	1750	0.03	217
M9	L-H	1750	0.03	258
M10	H-H	1750	0.09	308

ID	DOE Category	Speed (mm/s)	Hatch Spacing (mm)	Power (W)
M5	M-S	1750	0.05	303
M6	M-S	1750	0.05	324
H1	H-S	2500	0.05	250
H2	H-S	2500	0.05	275
H3	H-S	2500	0.05	300
H4	H-S	2500	0.05	325
H5	H-S	2500	0.05	350
H6	H-S	2500	0.05	375

L-S: Low scanning speed
M-S: Medium scanning speed
H-S: High scanning speed

ID	DOE Category	Speed (mm/s)	Hatch Spacing (mm)	Power (W)
M11	H-H	1750	0.09	382
M12	H-H	1750	0.09	456
H7	L-H	2500	0.03	172
H8	L-H	2500	0.03	215
H9	L-H	2500	0.03	257
H10	H-H	2500	0.09	303
H11	H-H	2500	0.09	379
H12	L-H	2500	0.09	455

L-H: Low hatch spacing
M-H: Medium hatch spacing
H-H: High hatch spacing

Figure 60 shows the coupons after production, while still attached on the build plate. Coupons L3, M3, and H6 were produced with an almost equal heat input (0.150 ±0.001 J/mm or 75 ±0.5 J/mm^3), but differing process parameters, as shown. Coupon M9 (circled red in Figure 60) failed to be completely produced due to the instability of the weld pool at the M9 parameter settings. Measurements revealed that all the holes had a diameter smaller than the designed nominal diameter. However, by an increase in the scanning speed, holes diameters became larger and closer to the nominal size.

Figure 61 compares the higher magnification images of the 0.07-in. holes produced with L3, M3, and H6 process parameters. The hole diameter was measured along and normal to the buildup direction (red line in Figure 61).

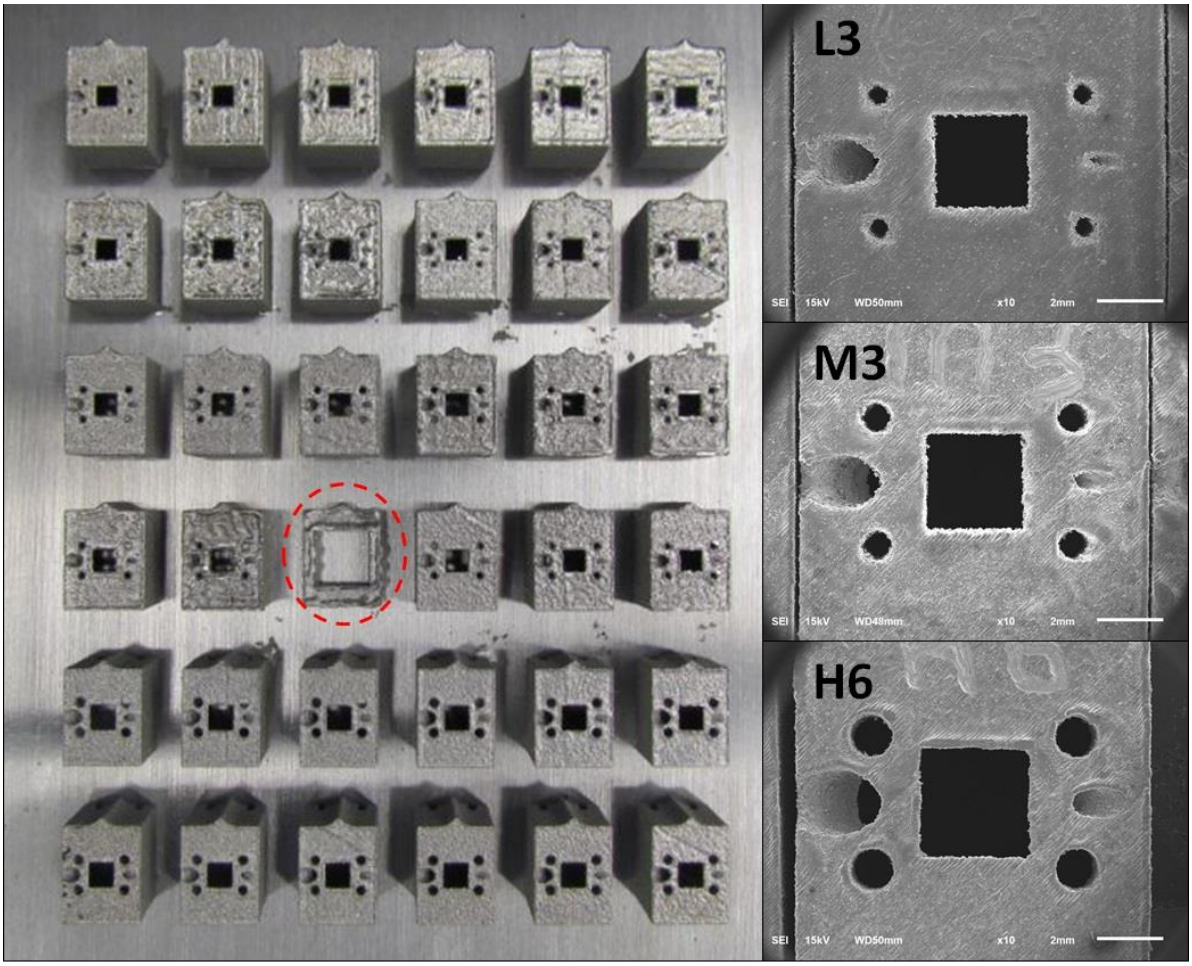

Figure 60. Coupons Produced for the Dimensional Accuracy

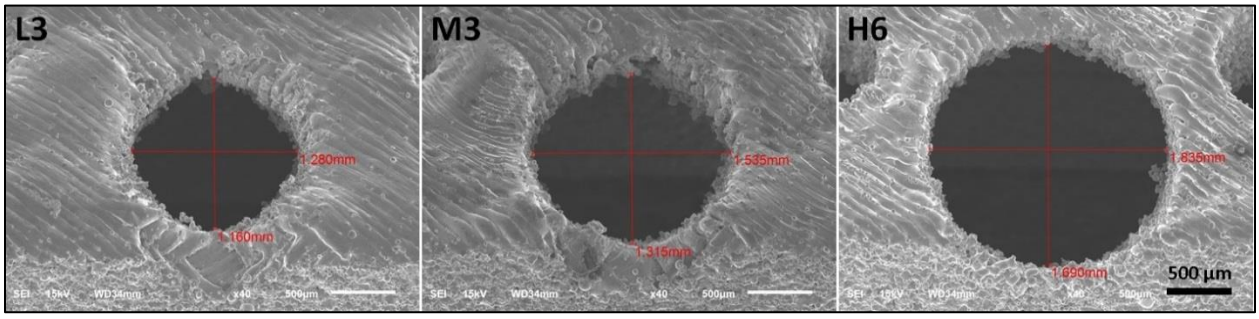

Figure 61. Comparison of the Diameters of the 45-degree Holes Produced with L3, M3, and H6 Parameters

Figure 62 compares the experimentally measured diameters of holes produced with parameters L1, M1, and H1. All parameters had a constant hatch spacing of 0.05 mm. The blue and red bars represent the hole diameters and errors compared to the nominal diameter, respectively. An increase in the scanning speed significantly reduced the error. Parameters H1 and H2 were

the only parameters that had negative errors, which means the holes produced with these two parameters were larger than the nominal diameter.

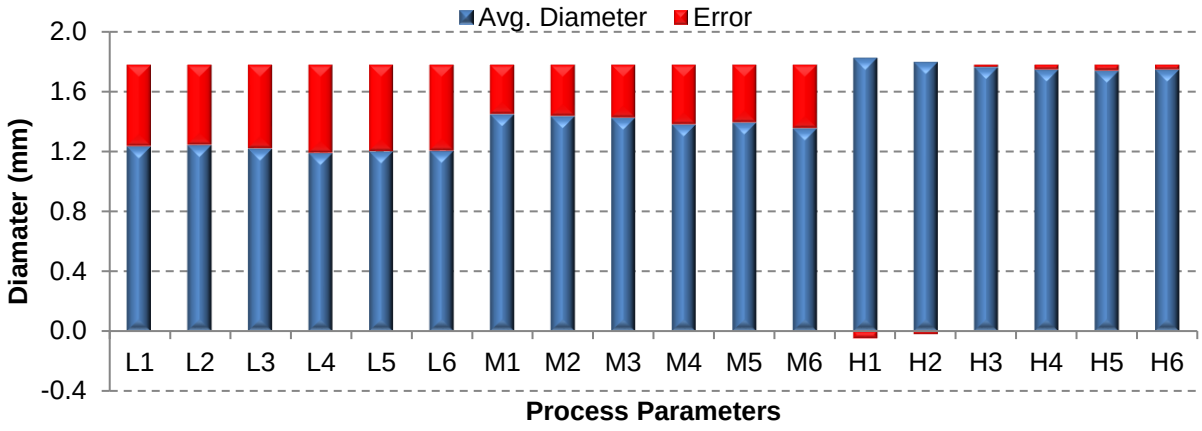

Figure 62. Influence of Scanning Speeds on the Dimensional Accuracy of the 70-degree Hole

L3, M3, and H6 had an almost equal energy density of 75 ±0.5 J/mm^3. However, each of the parameters used a laser power of 181, 261, and 375 W, respectively. Although the laser power in H6 was two times larger than that of L3, H6 produced a more accurate feature. It can be concluded that at a constant energy density applied on the Hastelloy X during L-PBF, laser scanning speed could be considered as the only or one of the primary factors influencing dimensional accuracy.

Figure 63 compares the influence of hatch spacing on dimensional accuracy. The scanning speed of 1200 mm/s with the largest levels of error was used for this comparison. The blue and red bars represent the hole diameters and errors compared to the nominal diameter, respectively. The smallest hatch spacing used at parameters L7-L9 resulted in the maximum error sizes from the nominal diameter. L10-L12 resulted in the minimum error. A second observation, at a constant laser scanning speed and hatch spacing, was that an increase in laser power (or heat input) was accompanied by an increase in error. This could be explained by the increase in the size of partially melted powders that attach to the actual design and result in dimensional error.

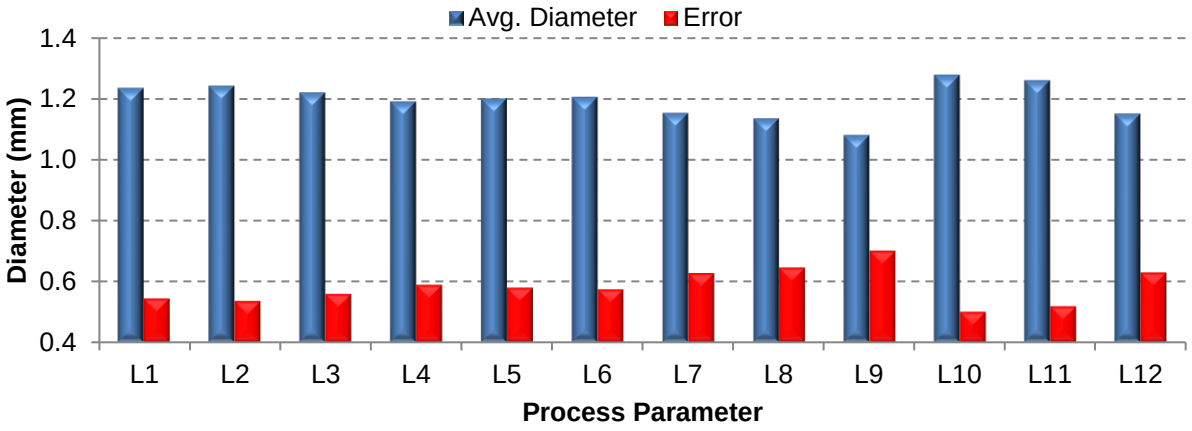

Figure 63. Influence of Hatch Spacing on the Dimensional Accuracy of the 70-degree Hole

According to the results, laser scanning speed had the primary impact on the dimensional accuracy, at a constant heat input. The key factor here is that when scan speed is changed significantly on a ProX300, a significant geometric adjustment is also required. Users should plan accordingly.

3.2.4 Heat Treatment Specimens

The minimum and maximum wall thicknesses in the original design of the fuel injector were incorporated into the design of the heat treatment coupon. Therefore, the influence of heat treatment procedures on microstructure of the coupons will be transferrable to the fuel injector component. Figure 64 shows the top and bottom view of the heat treatment coupon. Locations 1 through 6 refer to the different thicknesses of 0.254, 0.508, 0.889, 1.279, 1.279, and 2.540 mm, respectively. Locations 7 through 9 indicate the angled holes that were incorporated into the walls of the coupon. The four holes on the top surface were incorporated into the design to facilitate the mounting and polishing process.

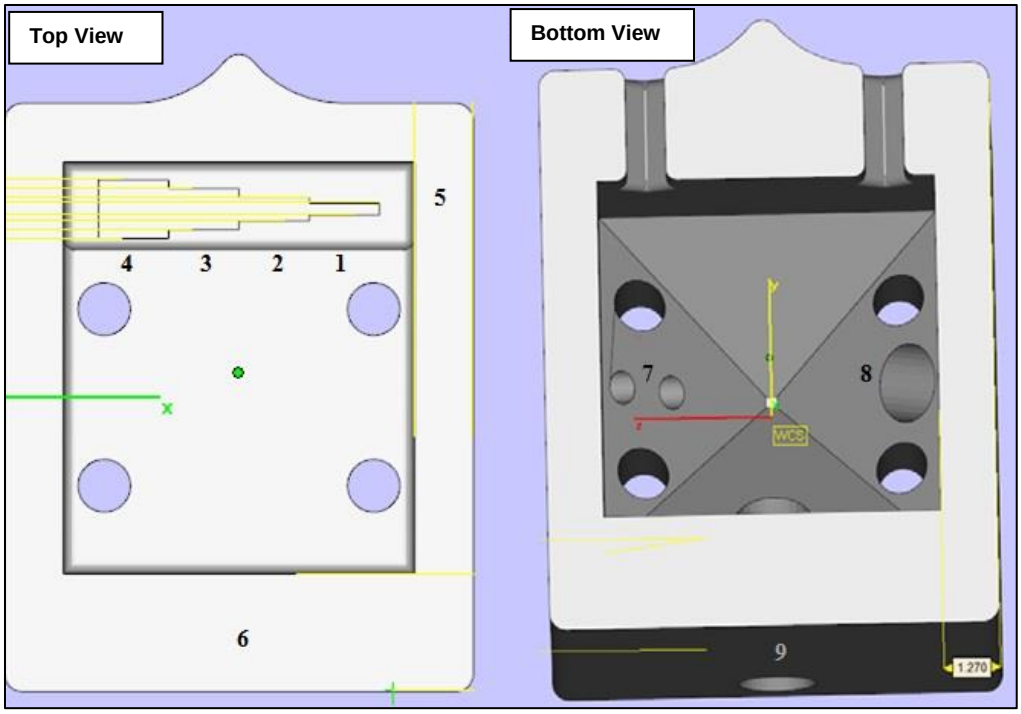

Figure 64. Design of the Heat Treatment Coupon

Figure 65 shows the heat treatment coupons produced using the nominal process parameters of the S1-F powder. All coupons were fabricated with a 0-degree angle inclination.

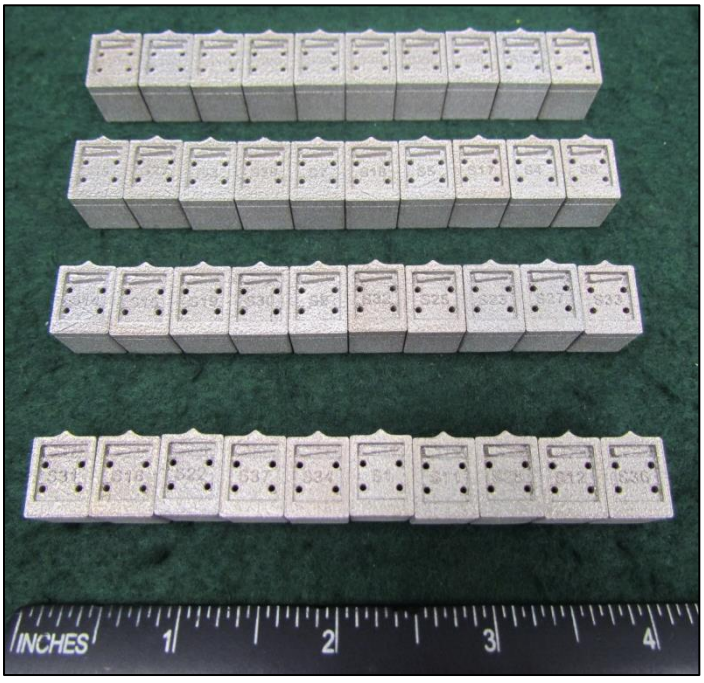

Figure 65. Heat Treatment Coupons Produced with the S1-F Powder

3.3 Heat Treat Process Development

Heat treating becomes an essential consideration to achieve final density for AM constructs. Low porosity is critical for the performance of any component, compared with cast or machined parts, and is a significant consideration for the fuel injector design. This section details the work aimed at finding the best combination of powder processing and heat treating to achieve the needed performance.

3.3.1 Heat Treatment Simulation by JMatPro

Conservative alloy development is time consuming and costly because it involves several experimental trials of alloy processing and evaluation. In addition, alloy properties optimization is very difficult due to the wide range of variables to be controlled.

Proper computational thermodynamics software can be used to shorten the alloy development process that provides appropriate methods for evaluating phase formation, carbide precipitates, and phase stability as a function of alloy composition and temperature. Software is developed and constructed based on the change of free energy of different phases with the changes in temperature, pressure, and the chemical composition. Among these software packages, the JMatPro software package was selected, since it was designed mainly for Ni-based alloys. The JMatPro database for Ni-based alloys can be run to calculate the effect of seventeen alloying elements at different temperatures and composition ranges at ambient pressure.

JMatPro analytical software was used extensively to investigate the differences in chemical composition of phases and their stability in Hastelloy X. The calculations indicated the effect of different alloying elements on the formation of undesirable phases such as σ- phase, μ-phase, Laves-phase, and secondary carbides. The precipitation of intermetallic phases, such as sigma, Mu, and Laves phase has a serious degradation effect on ductility and corrosion resistance in this order. Throughout these calculations, the formation temperature of each phase and mixing ratio between these phases could be predicted.

Calculations were performed on the two Hastelloy X powders, S2-F and S1-F. The team conducted a new set of chemical analyses to measure a few elements that were missing in certifications received from the powder suppliers. The chemical compositions of the two powders are shown in Table 21. Generally, the chemical compositions of the received powders were in conformance with the standard requirements and are within the specified limits. The main differences between these two powders were in the amounts of Mn, Si, and W. The Mn and Si contents for the S1-F powder were higher than that of the S2-F powder. On the other hand, the W content was higher in S2-F, than in S1-F.

Table 21. Chemical Compositions of the S2-F and S1-F Powders

Element	S2-F	S1-F	Standard
C	0.09	0.06	0.05-1.5
Mn	0.11	0.79	0.0-1.0
Si	0.23	0.83	0.0-1.0
P	0.012	0.011	0.0-0.04
S	0.005	0.005	0.0-0.03
Cr	21.0	20.7	20.5-23.0
Mo	8.6	8.6	8.0-10.0
Co	1.5	1.4	0.5-2.5
Fe	17.1	18.5	17.0-20.0
W	0.89	0.63	0.2-1.0
O	0.067	0.067	For Information
N	0.018	0.091	For Information
H	0.0008	0.0009	For Information
Ni	Balance	Balance	For Information

Differences highlighted in yellow.

Figure 66 and Table 22 show the calculation results of the types of phases and their stability and weight % as a function of temperature for the S2-F powder. The same results were calculated and shown for the S1-F powder in Figure 67 and Table 23.

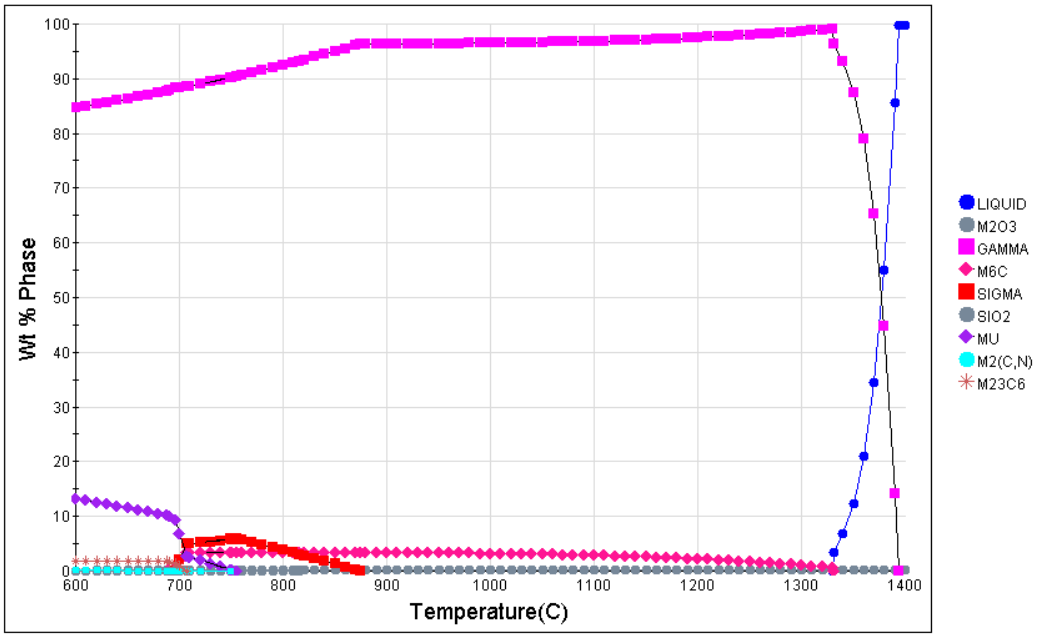

Figure 66. Calculated Phase Distribution Plot as a Function of Temperature in the S2-F Powder

Table 22. Temperature Dependent Percentages of Phases in the S2-F Powder

Phase	Temperature (°C)							
	1300	1200	1100	1000	900	800	700	600
Gamma	98.64	97.52	96.87	96.52	96.35	92.47	88.36	84.69
M_6C	1.15	2.27	2.92	3.27	3.44	3.51	1.77	---
Sigma	---	---	---	---	---	3.81	1.95	---
SiO_2	---	---	---	---	---	0.01	0.03	0.06
Mu (μ)	---	---	---	---	---	---	6.79	13.25
Laves	---	---	---	---	---	---		
$M_{23}C_6$	---	---	---	---	---	---	0.87	1.75
M_2O_3	0.21	0.21	0.21	0.21	0.21	0.20	0.16	0.10
$M_2(C,N)$	---	---	---	---	---	---	0.07	0.13

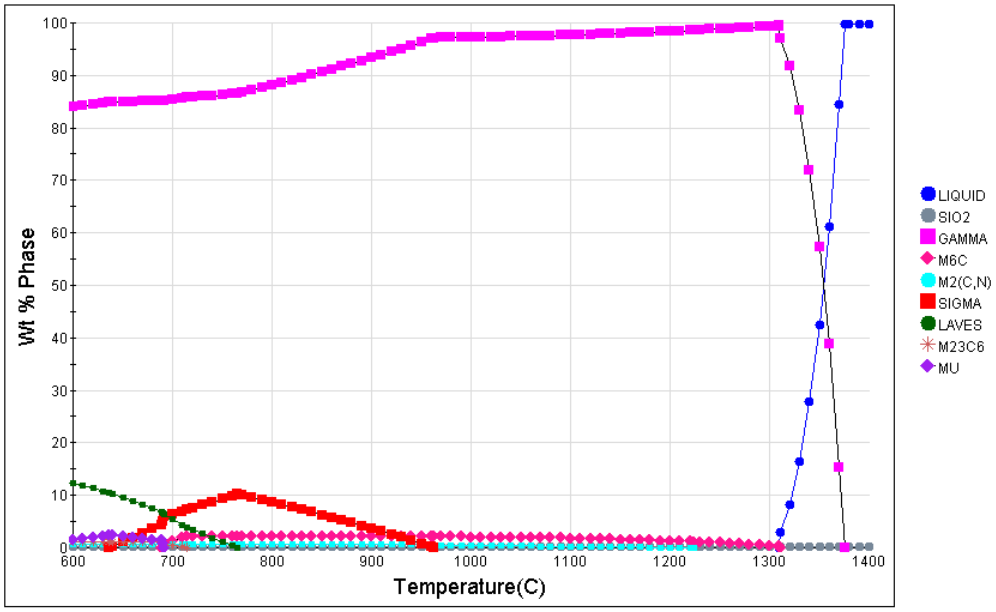

Figure 67. Calculated Phase Distribution Plot as a Function of Temperature in the S1-F Powder

Table 23. Temperature Dependent Percentages of Phases in the S2-F Powder

Phase	Temperature (°C)							
	1300	1200	1100	1000	900	800	700	600
Gamma	99.36	98.4	97.69	97.25	93.32	88.17	85.39	84.03
M_6C	0.51	1.42	1.91	2.16	2.26	2.3	1.27	---
Sigma	---	---	---	---	3.65	8.65	6.38	---
SiO_2	0.13	0.13	0.13	0.13	0.13	0.13	0.13	0.13
Mu (μ)	---	---	---	---	---	---	---	1.51
Laves	---	---	---	---	---	---	5.52	12.38
$M_{23}C_6$	---	---	---	---	---	---	0.52	1.16
M_2O_3	---	---	---	---	---	---		
$M_2(C,N)$	---	0.06	0.13	0.47	0.65	0.76	0.79	0.79

The following conclusions were drawn from the JMatPro analyses.

- At high temperature, ranging from 1300-1000°C (just below the solidus temperature):
  - Both powders have the same equilibrium phases, mainly gamma phase and M_6C carbide.
  - The S2-F powder has a higher amount of M_6C carbide than S1-F at the same temperature.
  - A small amount of SiO_2 could be formed in the S1-F powder due to the higher Si content, in addition to the formation of $M_2(C,N)$ compound as a result of higher nitrogen content compared to the S2-F powder.
  - On the other hand, the S2-F powder showed the potential to form a small amount of the M_2O_3 intermetallic compound.
- At 900°C:
  - Sigma phase formation is predicted in the microstructure of the S1-F powder, while the S2-F powder showed a slight increase in M_6C phase content.
  - Sigma phase is predicted to start formation at 963°C, per the calculation results.
- At 800°C:
  - Sigma phase formation is predicted to be present in the microstructure in the S2-F powder.
  - Sigma phase is predicted to start formation at 874°C in the S2-F powder, per the calculation results.
  - The amount of sigma phase in the S1-F powder increased by a factor of 2.4 times, compared to that at 900°C.
- At 700°C:
  - The predicted formed phases are similar with different phase distribution wt%, except:
    - The S1-F powder showed the presence of Laves phase. The formation temperature of Laves phase is calculated to be 764°C
    - The S2-F powder showed the presence of Mu (μ) phase. The formation temperature of Mu phase is calculated to be 755°C.
  - This difference could be attributed to different chemical composition and the major constituents in each phase as follows:
    - Mu phase: the typical major constituents are Mo, W, Ni, Co, Cr. The S2-F powder has the same Mo amount with higher W content
    - The general formula of the Laves phase is AB_2. There are a large number of intermetallic phases under this formula based on the alloying elements. It was reported that for a Ni-based alloy with a high level of Cr (20 wt.%) together with a certain amount of Fe (10 wt.% or above) in addition to the presence of high amount of Si and Mn, the formation of Laves phase is possible.[6] The S1-F powder contains higher amounts of the above-mentioned alloying element.
- At 600°C:
  - Both sigma phase and M_6C carbide are dissolved in the two powders.
  - Higher amount of Laves phase was predicted for the S1-F powder and Mu phase for the S2-F powder.

- The precipitation of intermetallic phases, such as sigma, Mu, and Laves phase, has a serious degradation effect on ductility and corrosion resistance in this order.

Regarding the predicted phase formation and precipitation, the effect of Mn, Si, and W was investigated at constant temperature (800°C). The results are shown in Figure 68 for the S2-F powder and Figure 69 for the S1-F powder. Only the effect of a single alloying element change with respect to Ni content was investigated while all other elements were kept constant.

The results indicated the complex interactions between the alloying content and the distribution of formed phases and precipitates. The obtained results can be summarized as follows:

- For the S2-F powder:
  - With increasing Mn content, the amount of Mu phase decreased and the sigma phase increased.
  - With increasing Si content, the amount of sigma phase increased up to 0.75 wt.% Si, and then decreased. The amount of the Mu phase kept constant, up to 0.85 wt.% Si, and then decreased with increasing Si content.
  - With increasing W content, the amount of sigma phase decreased and Mu phase increased.
- The S1-F powder:
  - With increasing Mn content, the amount of both sigma phase and Laves phase remained constant, while the amount of M_6C carbide decreased.
  - With increasing Si content, the amount of sigma phase increased to a maximum value at 0.6 wt.% Si and then sharply decreased. Also at 0.6 wt.% Si, the Laves phase started to increase.
  - With an increase in the W content, the amount of both sigma phase and Laves phase remained constant up to 0.85 wt.%, and then the amount of sigma phase decreased and Laves phase increased.

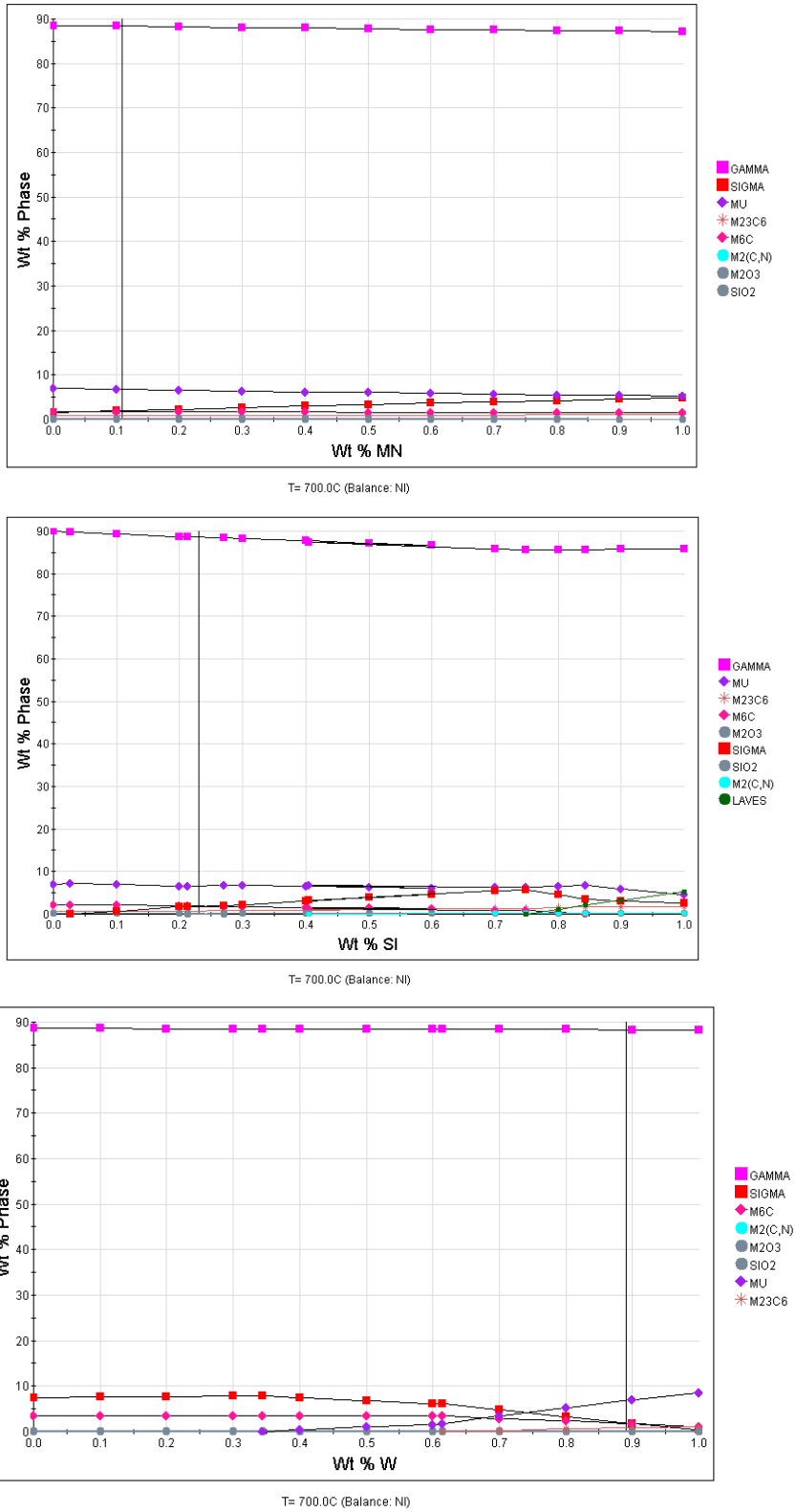

Figure 68. Phase Distribution for the S2-F Powder at 700°C as a Function of Mn, Si, and W Content

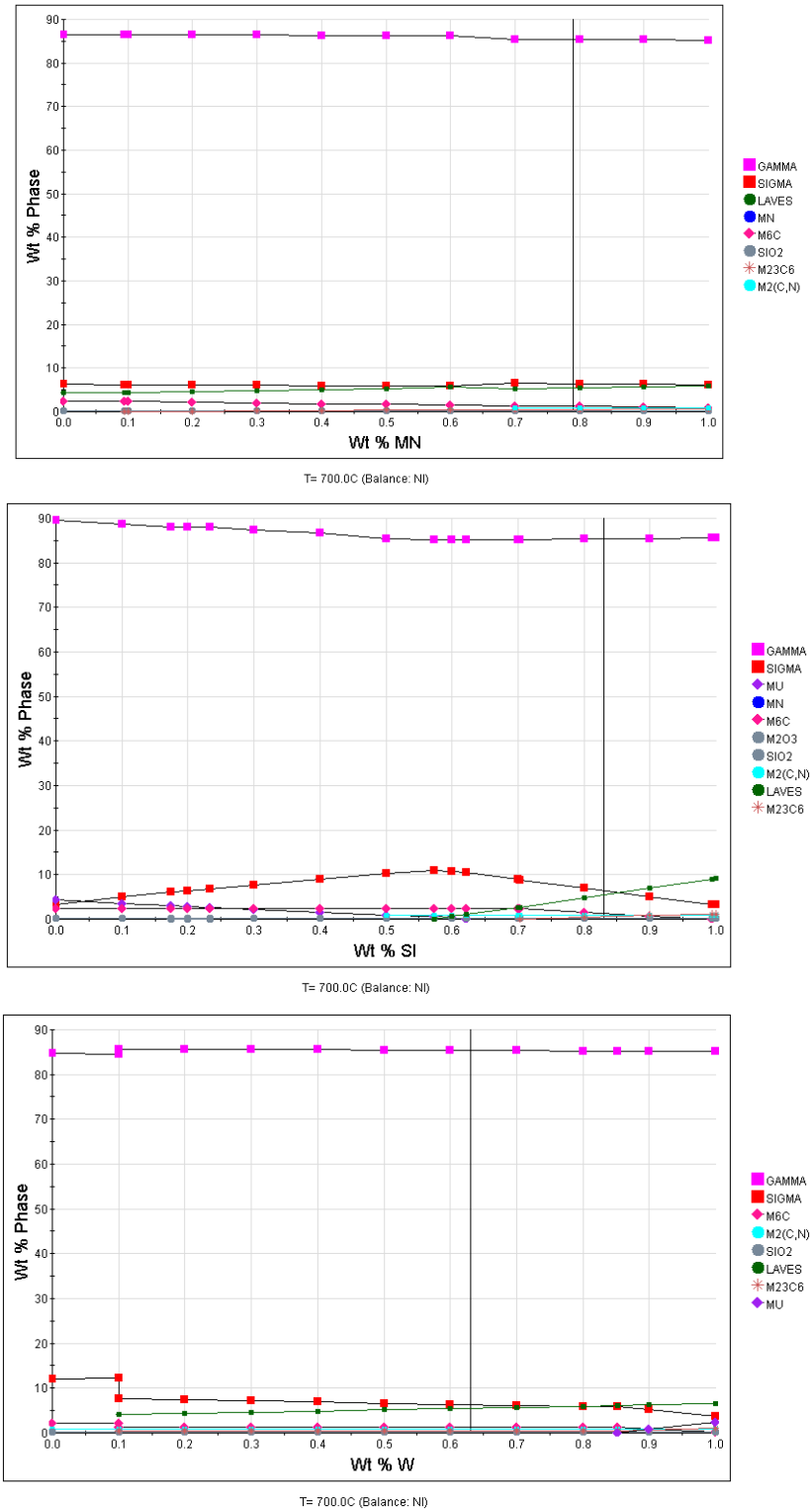

Figure 69. Phase Distribution for the S1-F Powder at 700ºC as a Function of Mn, Si, and W Content

These results represent a guide in Hastelloy X chemical composition development and predict a wide range of behavior with respect to the phase distribution and stability at different temperatures. However, these calculations were done with the assumption of the establishment of equilibrium conditions. During the fast solidification and cooling in AM processes, segregation can lead to many non-equilibrium conditions.

Nevertheless, the results revealed the stability of phases and transformation from high temperature M_6C carbides to low temperature $M_{23}C_6$ carbides. In addition, the results reflected the high sensitivity of the formation and presence of difference phases to chemical composition.

3.3.1 Experimental Heat Treatment

Based on the results obtained from the JMatPro analysis, as well as previous experiences with the heat treatment of Hastelloy X, multiple procedures were developed for heat treatment. Table 24 provides a list of ten heat treatment cycles that were developed. A combination of solution annealing, HIP, and aging were offered to down-select an optimum heat treatment procedure. At the first step, the team completed procedures 1-a, 1-b, 1-c, 2, 6, 7, and 8.

Table 24. Heat Treatment Procedures Developed for the Hastelloy X

HT Procedure	Solution Annealing			HIP				Aging					
	Temp. (°F)	Time	Post Cooling	Temp. (°F)	Pressure (MPa)	Time (hr)	Post Cooling	Temp._1 (°F)	Time_1 (hr)	Post Cooling	Temp._2 (°F)	Time_2 (hr)	Post Cooling
1-a	2150	15 min.	AC	---	---	---	AC	---	---	---	---	---	---
1-b	2150	40 min.	AC	---	---	---	AC	---	---	---	---	---	---
1-c	2150	1 hr	AC	---	---	---	AC	---	---	---	---	---	---
2	---	---	---	2150	100	4	AC	---	---	---	---	---	---
6	2150	4 hr	AC	---	---	---	AC	---	---	---	---	---	---
7	2150	8 hr	AC	---	---	---	AC	---	---	---	---	---	---
8	2200	1 hr	AC	---	---	---	AC	---	---	---	---	---	---

AC: Argon cooling

Representative coupons are shown in Figure 70. These materials were produced with the four candidate powders and show minimal grain growth for the S1-F powder in contrast to the significant grain growth for the other three powders.

Figures 71-74 show how the microstructure of the Hastelloy X coupons has responded to the different HT procedures. Images were taken on two cross sections parallel (Z) and normal (XY) to the buildup direction, at 200× and 500× magnification.

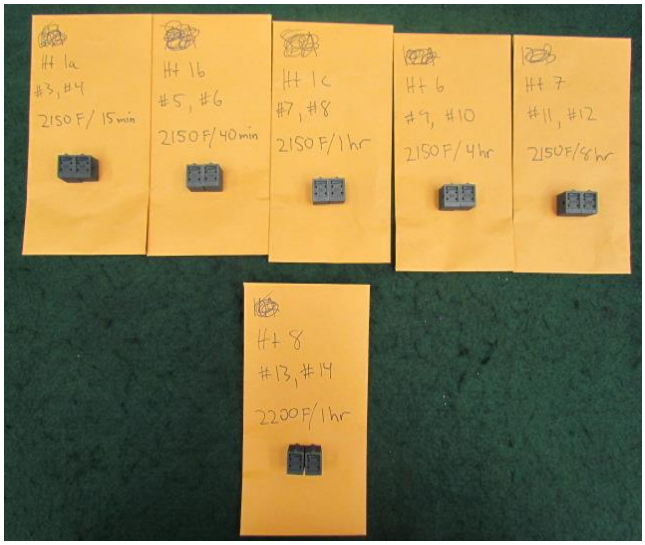

Figure 70. HT Coupons per Procedures 1- a, 1-b, 1-c, 6, 7, and 8

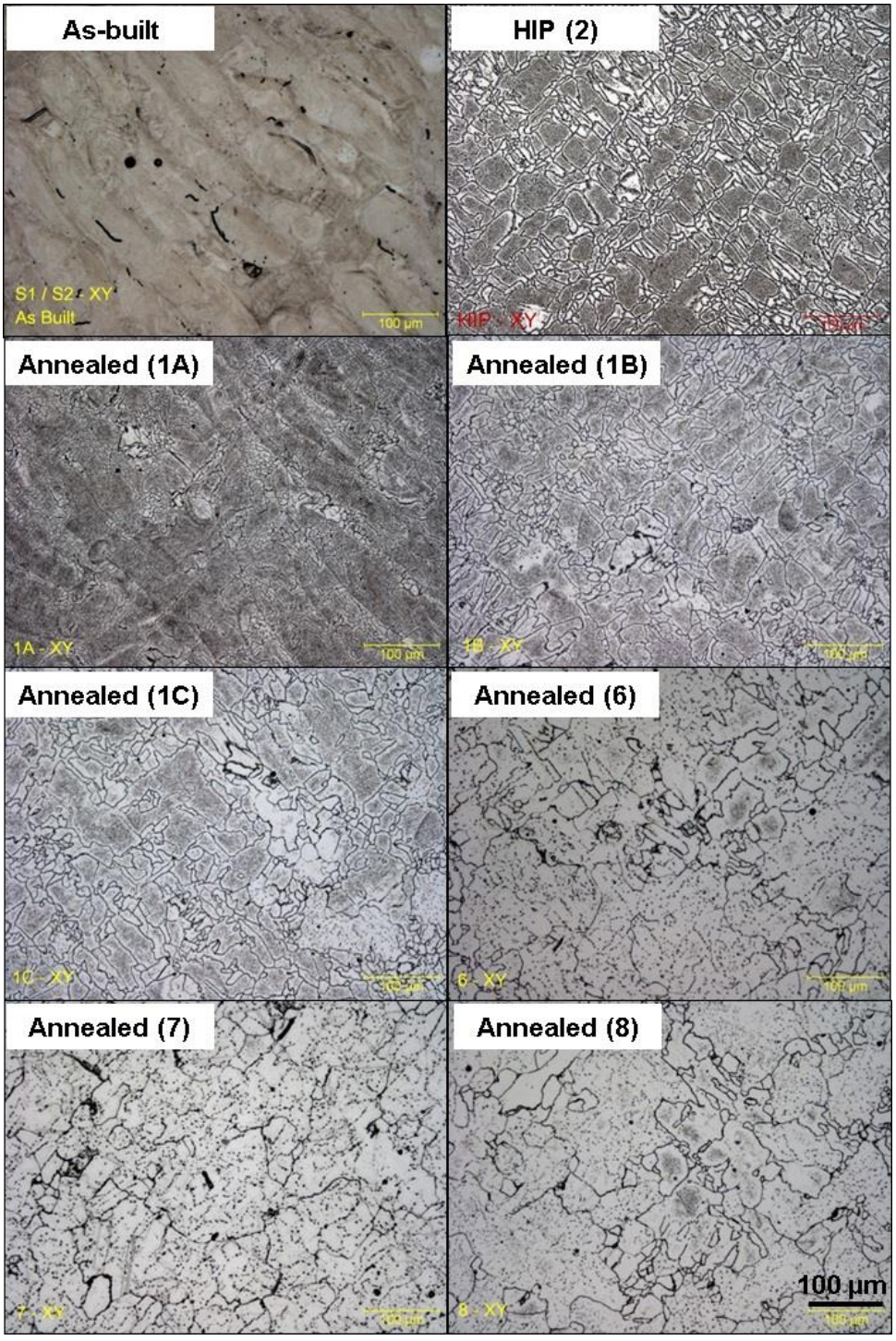

Figure 71. Microstructures of Hastelloy X Specimens Underwent Different HT Procedures (images - XY cross sections (transverse to the build up direction) at 200× magnification)

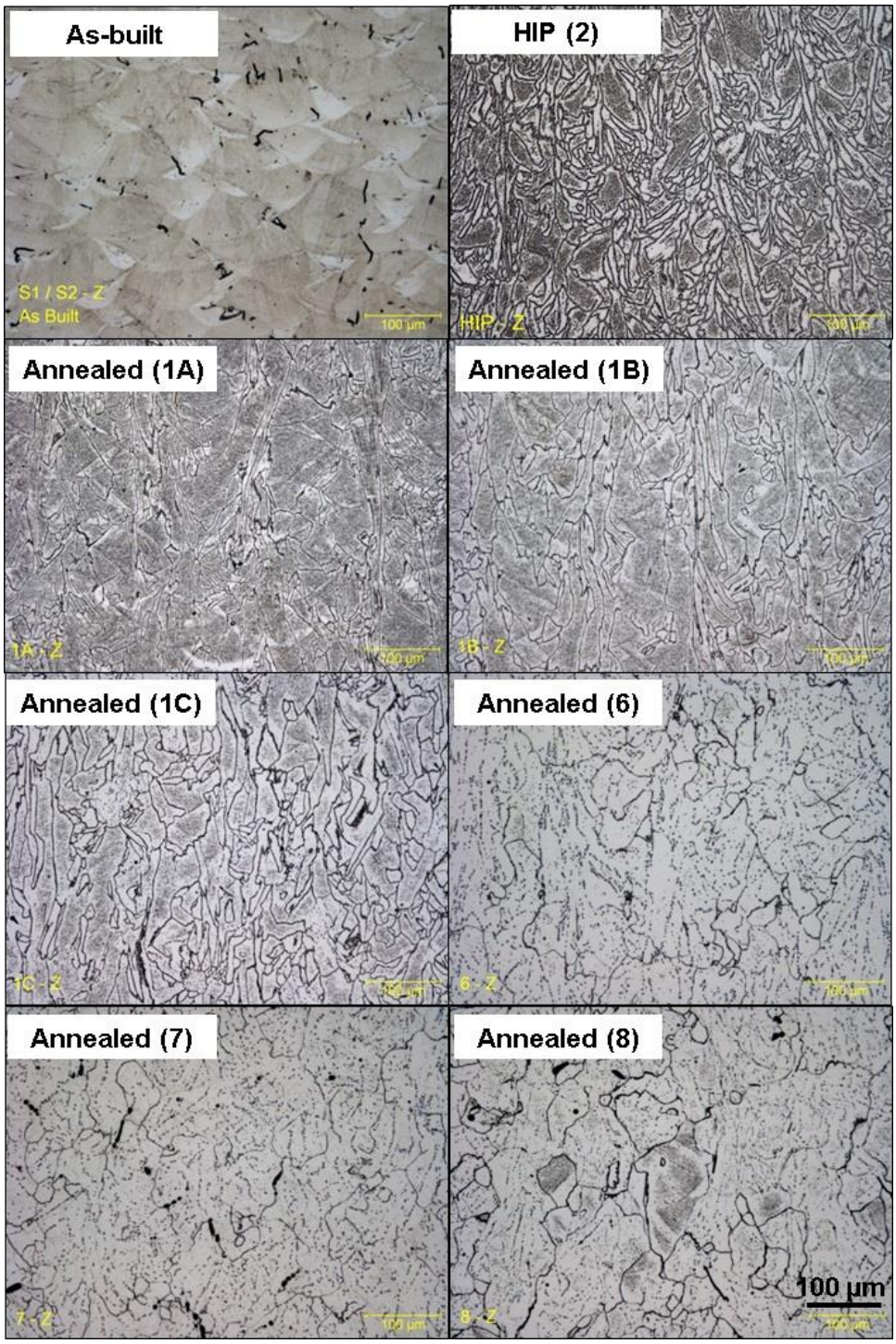

Figure 72. Microstructures of Hastelloy X Specimens Underwent Different HT Procedures (images - Z cross sections (parallel to the buildup direction), at 200× magnification)

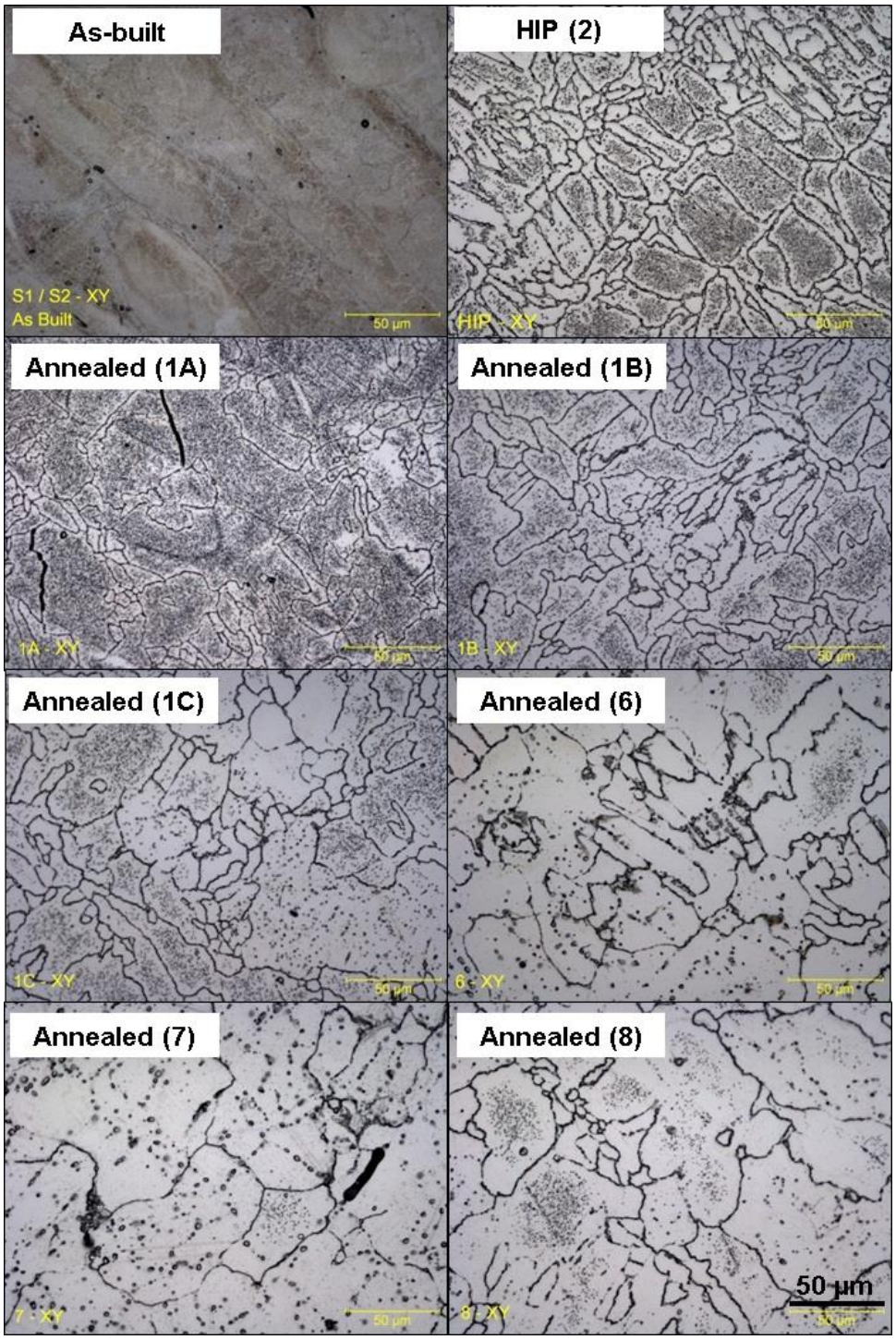

Figure 73. Microstructures of Hastelloy X Specimens Underwent Different HT Procedures (Images - XY cross sections (transverse to the buildup direction), at 500× magnification)

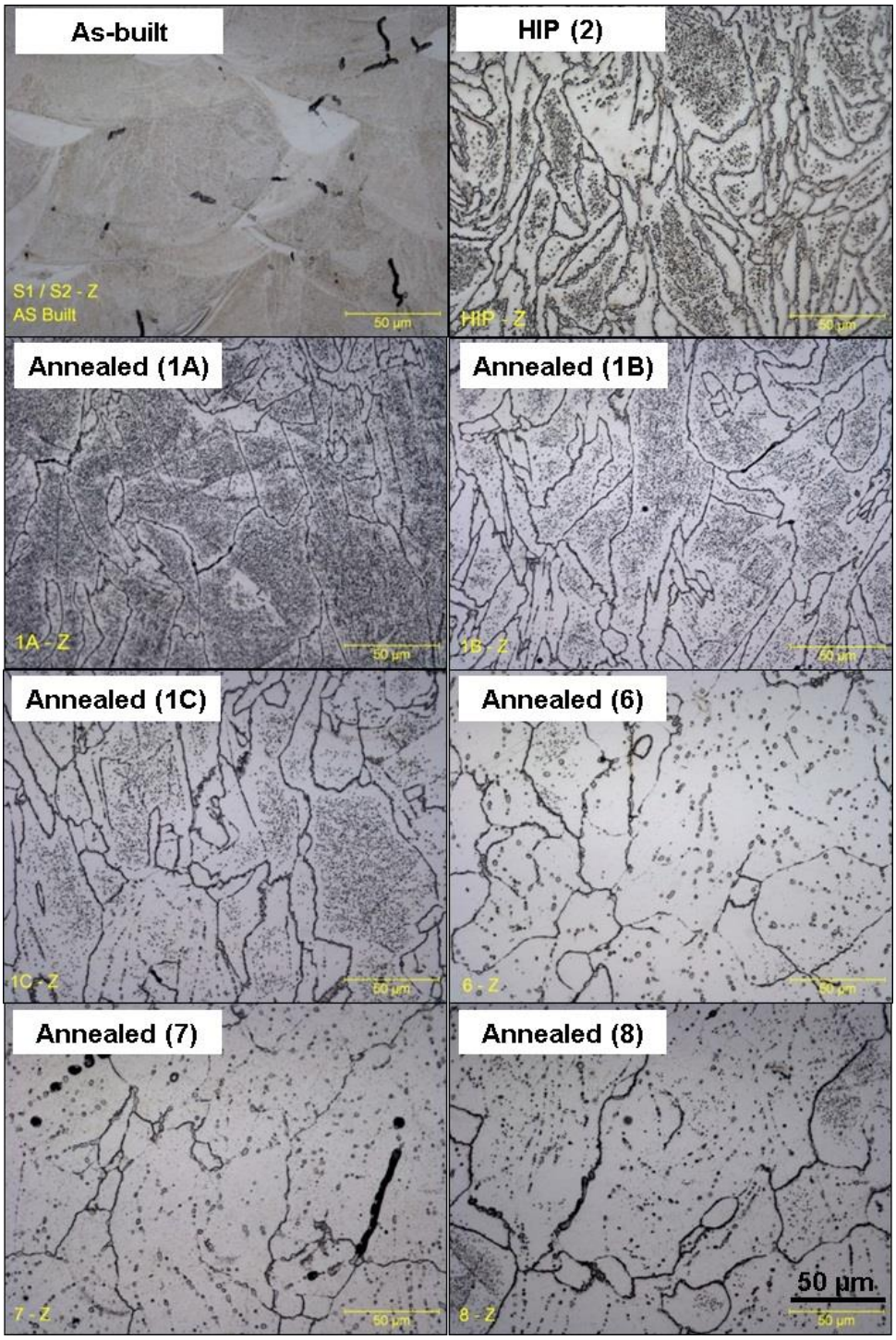

Figure 74. Microstructures of Hastelloy X Specimens Underwent Different HT Procedures (images - Z cross sections (parallel to the buildup direction), at 500× magnification)

3.3.1.1 The Influence of Annealing Time

3.3.1.1.1 Grain Growth. The identical annealing temperature of 2150°F was used in all the heat treatment procedures 1a, 1b, 1c, 6, and 7; annealing time was the only variable. As expected, with an increase in the annealing time from 15 minutes (1a) to 40 minutes (1b), recrystallization started. This increase could suggest that an incubation time less than 40 minutes (at 2150°F) is expected for Hastelloy X produced by the L-PBF process in this project. Grain growth progressed at the longer annealing times of 4 hours (6) and 8 hours (7).

3.3.1.1.2 Precipitates Distribution. Similar to the results of grain growth, dissolution of grain interior precipitates was increased with an increase in the annealing time. The diffusion process required for the dissolution took a longer time to complete.

3.3.1.2 The Influence of Annealing Temperature

The two annealing procedures of 1c and 8 were performed for one hour, at 2150°F and 2200°F, respectively. A slight increase in temperature had a significant influence on the activation and progress of grain growth for the AM material. Grain growth is dependent upon the diffusion process that is influenced by the amount of residual stresses, which is the driving force for recrystallization and grain growth, as well as the annealing time and temperature. At a constant amount of residual stresses and time, the temperature has a significant impact on the resultant grain size, type, and amount of precipitates.

3.3.1.3 The Influence of External Pressure during the HIP Cycle

Coupons 2 and 6 were heated for four hours at 2150°F. However, Coupon 2 was kept under a 100-MPa (14.5 ksi) isostatic pressure, as for a HIP cycle. Because of the applied external isostatic pressure, grain growth was significantly controlled in Coupon 2. This could be attributed to the induced strain during HIP that could hinder the movement of the grain boundaries. Thus, a smaller fraction of elements could sweep and migrate toward the grain boundaries. Coupon 6 showed a significant reduction in the volume fraction of precipitates.

Figure 75 compares the influence of heat treatment procedures on microstructures of Hastelloy X coupons at a higher magnification. All images were taken on the X-Z cross sections (parallel to the buildup direction). A dense distribution of intragranular precipitates could be observed in the microstructure after 15 minutes' exposure to 2150°F. Also, some particles with relatively fine sizes precipitated on grain boundaries. After one hour exposure to the same temperature, some finer grain interiors were almost completely depleted from precipitates, while grain boundary precipitates became slightly larger. Eight hours of soaking at 2150°F was enough for a significant grain growth. Almost all the fine precipitates at the matrix merged and formed

significantly larger particles. Specimens 1a, 1c, and 7 had an annealing temperature of 2150°F, but with the annealing times of 15, 60, and 240 minutes, respectively.

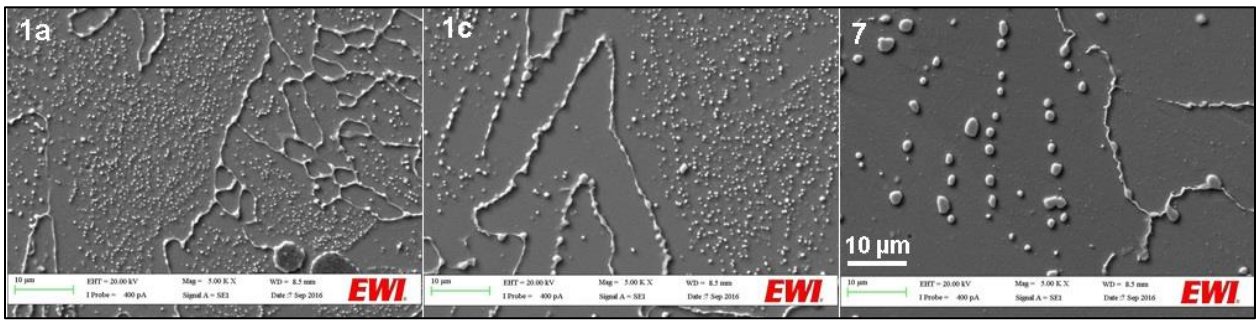

Figure 75. SEM Images of the Hastelloy X Coupons Heat Treated at 2150°F for 15 minutes (left)**, 1 hour** (middle)**, and 4 hours** (right)

Figure 76 shows a high magnification image of the precipitates formed in the matrix of the HIP'd specimen. Table 25 presents the chemical compositions of four precipitates and the matrix measured using EDS.

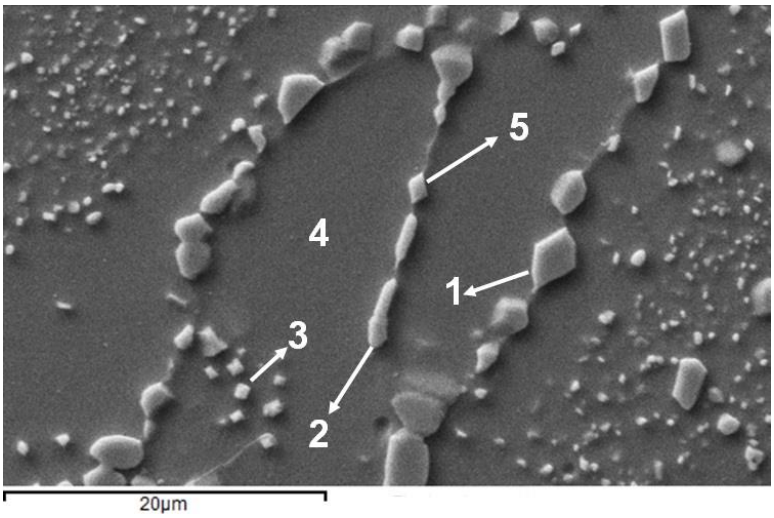

Figure 76. Higher Magnification Images of the Precipitates Formed in Hastelloy X Specimen after the HIP HT Procedure

Table 25. Chemical Composition (wt%) of Precipitates and the Matrix of the HIP'd Hastelloy X Specimen, Measured Using SEM/EDS

Element	Specimen 1	Specimen 2	Specimen 3	Specimen 4- Matrix	Specimen 5
Si	4.43	3.55	4.09	0.65	4.77
Cr	16.43	19.13	18.36	22.01	16.67
Mn	0.38	0.53	0.43	1.0	0
Fe	4.75	10.99	9.6	19.5	5.72
Co	0.67	0	0.91	1.67	0.72
Ni	22.52	32.93	31.58	46.7	23.94
Mo	47.15	30.48	32.53	7.64	44.94
W	3.67	2.39	2.5	0.84	3.24

Results of the chemical analysis are plotted in Figure 77. The red and blue arrows indicate the decrease or increase in the content of an element, respectively, compared to the Hastelloy X matrix. All four selected precipitates showed a considerable increase in Si, Mo, and W and decrease in Cr, Fe, and Ni. However, precipitates in Specimens 1 and 5 had a nearly identical chemical composition and were different than the other two identical precipitates of Specimens 2 and 3. Further analysis of the precipitates using x-ray diffraction would provide additional information to identify types of precipitates.

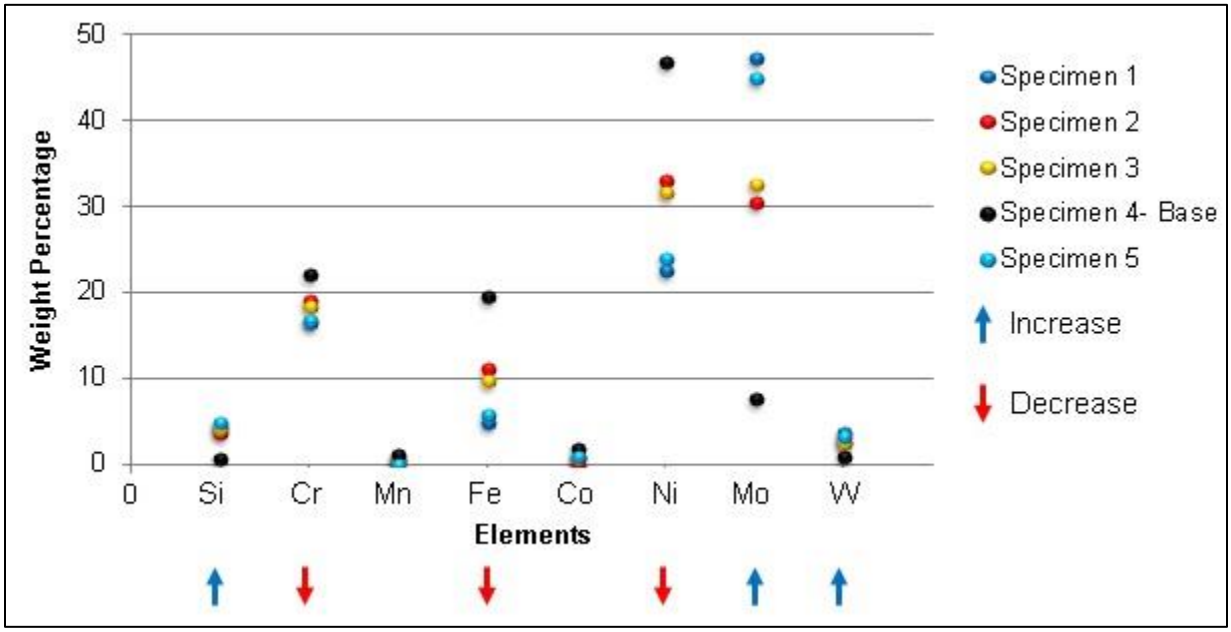

Figure 77. Comparison of the Chemical Composition of Precipitates and the Matrix of the HIP'd Hastelloy X Specimen

3.3.1.4 Hardness Measurement

Hardness of the heat-treated samples, as well as the as-built specimen, was measured, using a 100-Kg load (Figure 78). As expected, an increase in the annealing time was accompanied by a reduction in hardness, caused by the grain growth and precipitations dissolution. HT 8, with a 50°F increase in the annealing temperature, showed a significant decrease in hardness compared to HT 1c. Also, a larger deviation in hardness could be found in Coupon 8 that could be attributed to the in-homogeneous and local growth of some grains (Figure 76).

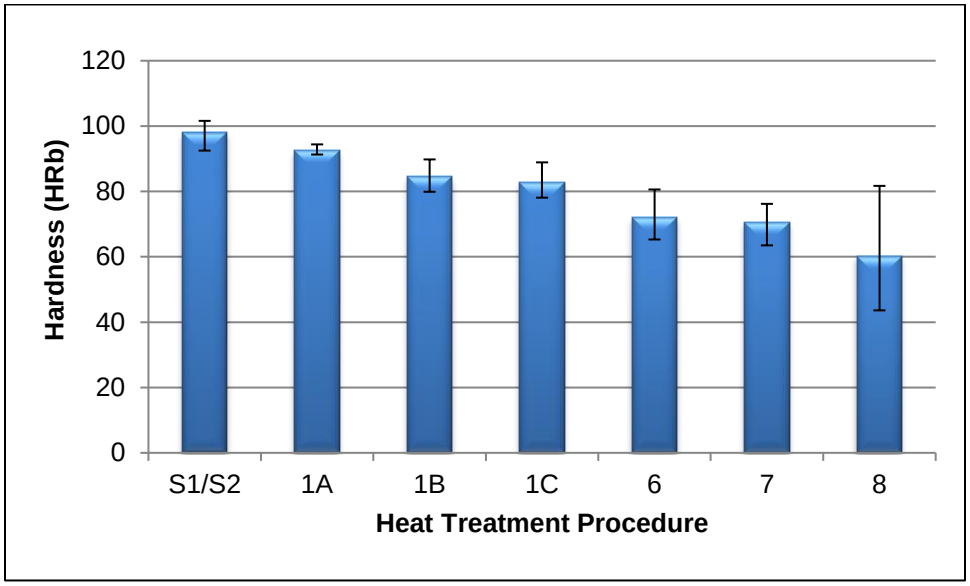

Figure 78. Influence of Different Heat Treatment Cycles on the Hardness of Hastelloy X, Produced by L-PBF

Based on the results, the three HT procedures 1c, 2, and 6 were selected to be the basis for additional heat treat studies on mechanical test walls. These three HT procedures provided significantly different microstructures, as described above.

3.3.2 Advanced HT Procedures

Based on this work, a shorter list of HT procedures was developed. Those processes are shown in Table 26. Another test specimen was defined for advanced studies of creep and LCF. It was called a “mechanical test wall”. Nominal dimensions are 105×15×10 mm (Figure 79).

Table 26. Down-selected HT Procedures for the Hastelloy X

HT Procedure	Solution Annealing			HIP			Solution Annealing		
	Temp. (°F)	Time (hr)	Post Cooling	Temp. (°F)	Pressure (MPa)	Time (hr)	Temp. (°F)	Time (hr)	Post Cooling
R1	2150	1	ArC	---	---	---	---	---	---
R2	---	---	---	2150	100	4	---	---	---
R3	---	---	---	2150	100	4	2150	1	ArC
R4	2150	4	ArC	---	---	---	---	---	---

ArC: Argon cooling

Figure 79. Mechanical Test Walls Produced for the Fabrication of Creep and Fatigue Specimens along the XY Direction

3.3.2.1 HT Specimens Based on Treatments R1-R4

Figure 80 compares the microstructure of HT Hastelloy X along the buildup direction. The black arrow indicates the buildup direction. R1 and R2 show very fine grain sizes, with R2 having a slightly finer grain size. These sizes could be attributed to the induced strain during HIP that could hinder the movement of the grain boundaries. As a result, a smaller fraction of elements could sweep and migrate toward the grain boundaries. R2 showed a dense population of precipitates.

Figure 81 shows higher magnification images of the microstructure. The application of solution annealing for an hour after the HIP process initiated the recrystallization in the microstructure. Based on the previous results, 40 minutes was enough to start the recrystallization at 2150°F, in

addition to the formation of grain boundary precipitates. The increase in annealing time from one hour in R1 to four hours in R4 was accompanied by precipitate dissolution and coarsening. In addition, a significant grain growth was observed.

Grain growth is dependent upon the diffusion process that is influenced by the amount of residual stresses, annealing time, and annealing temperature. At a constant amount of residual stresses and temperature, more time encourages the grain growth.

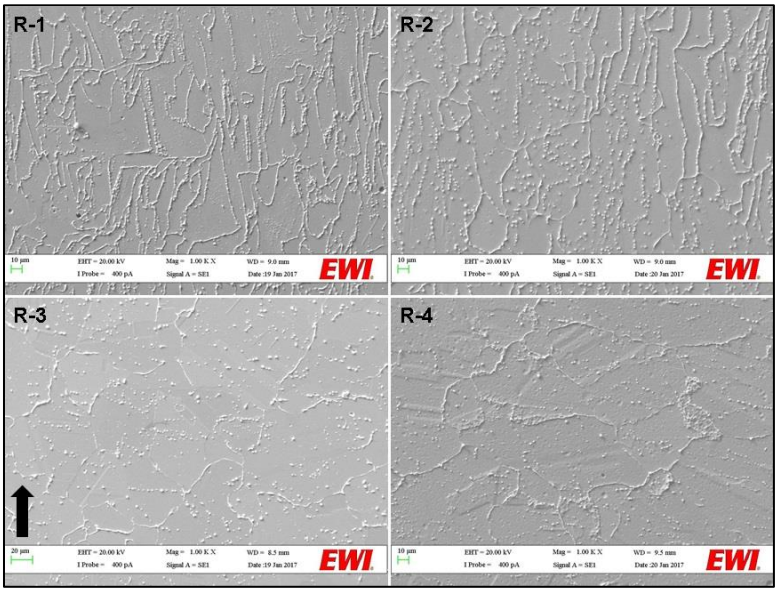

Figure 80. SEM Images of the HT Hastelloy X along the Buildup Direction (black arrow shows the buildup direction)

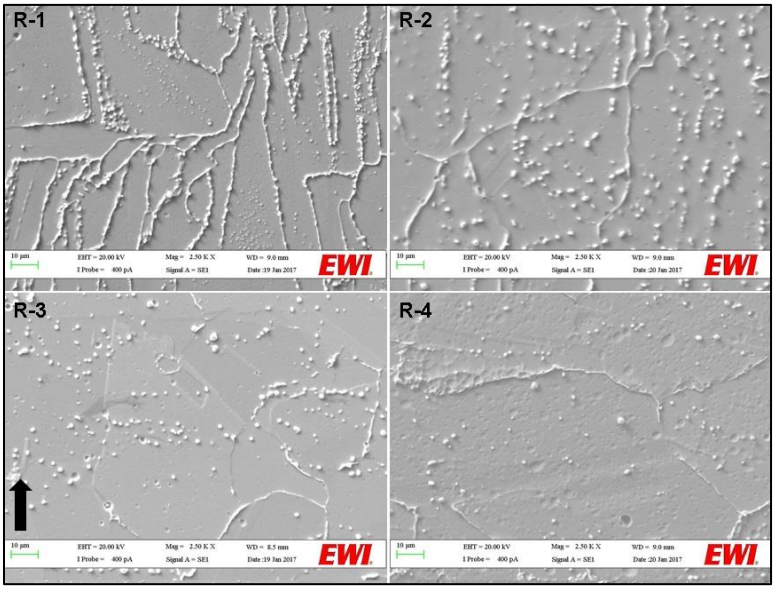

Figure 81. SEM of the HT Hastelloy X along the Buildup Direction (black arrow shows the buildup direction)

3.3.2.2 Room Temperature Tensile Test

The room temperature tensile test was conducted at EWI. Specimens with the gage diameter of 0.25 in. and gage length of 1 in. were machined from the mechanical test walls, per the ASTM E8-09 standard. The extension rate (crosshead speed) was set at 0.05 in./min. Three specimens were prepared and tested from each of the heat treatment conditions per orientation. The results of the room temperature tensile test for all four HT conditions are summarized in Table 27. The minimum tensile requirements for investment cast Hastelloy X (per AMS 5390) are tabulated at the last row of Table 27. The average values of ultimate tensile strength and 0.2% yield strength in both XY and Z orientations were plotted in Figure 82. The average values of elongation (%) and RA (%) in both XY and Z orientations were plotted in Figure 83. The dashed lines on the plots indicate the minimum requirements per AMS 5390.

Table 27. Summary of the Results of the Room Temperature Tensile Test for S1-Fine HT Specimens

Sample ID	Test Temp. (°C)	Test Temp. (°F)	Avg. YS		Avg. UTS		Avg. El. (%)	Avg. RA (%)	Failure Location
			MPa	ksi	MPa	ksi			
R1-Z-1	23	73.4	472.98	68.60	812.89	117.90	34	36	Within gage length
R1-Z-2	23	73.4	464.02	67.30	799.10	115.90	31	32	Within gage length
R1-Z-3	23	73.4	416.44	60.40	799.79	116.00	22	43	Within gage length
R1-XY-1	23	73.4	481.94	69.90	837.02	121.40	23	31	Within gage length
R1-XY-2	23	73.4	492.98	71.50	837.71	121.50	24	25	Within gage length
R1-XY-3	23	73.4	481.25	69.80	823.92	119.50	18	12	Outside gage length
R2-Z-1	23	73.4	341.98	49.60	759.80	110.20	20	16	Outside gage length
R2-Z-2	23	73.4	339.22	49.20	713.61	103.50	21	22	Within gage length
R2-Z-3	23	73.4	335.09	48.60	729.47	105.80	22	25	Within gage length
R2-XY-1	23	73.4	370.25	53.70	749.46	108.70	20	18	Within gage length
R2-XY-2	23	73.4	354.39	51.40	768.77	111.50	25	26	Within gage length
R2-XY-3	23	73.4	378.52	54.90	742.57	107.70	19	22	Within gage length
R3-Z-1	23	73.4	368.18	53.40	797.72	115.70	42	40	Within gage length
R3-Z-2	23	73.4	359.22	52.10	806.00	116.90	41	41	Within gage length
R3-Z-3	23	73.4	366.80	53.20	803.24	116.50	41	33	Within gage length
R3-XY-1	23	73.4	373.70	54.20	815.65	118.30	39	35	Within gage length
R3-XY-2	23	73.4	370.94	53.80	823.23	119.40	38	32	Within gage length
R3-XY-3	23	73.4	365.42	53.00	815.65	118.30	41	39	Within gage length
R4-Z-1	23	73.4	365.42	53.00	751.53	109.00	27	25	Within gage length
R4-Z-2	23	73.4	353.01	51.20	770.83	111.80	26	28	Within gage length
R4-Z-3	23	73.4	368.18	53.40	806.69	117.00	29	28	Within gage length

Sample ID	Test Temp. (°C)	Test Temp. (°F)	Avg. YS		Avg. UTS		Avg. El. (%)	Avg. RA (%)	Failure Location
			MPa	ksi	MPa	ksi			
R4-XY-1	23	73.4	412.31	59.80	822.54	119.30	34	31	Within gage length
R4-XY-2	23	73.4	375.76	54.50	821.17	119.10	42	34	Within gage length
R4-XY-3	23	73.4	380.59	55.20	818.41	118.70	34	25	Within gage length
Reference AMS5390 Investment Cast Ni Alloy X Specification Requirements			241.0	35.0	379.0	55.0	8.0	Not rated	

All specimens showed a significantly higher strength and ductility compared to the AMS 5390 requirements. It should be noted that the AMS 5390 specification is for the investment cast Ni Alloy X material and the comparison to the AM material is only for reference.

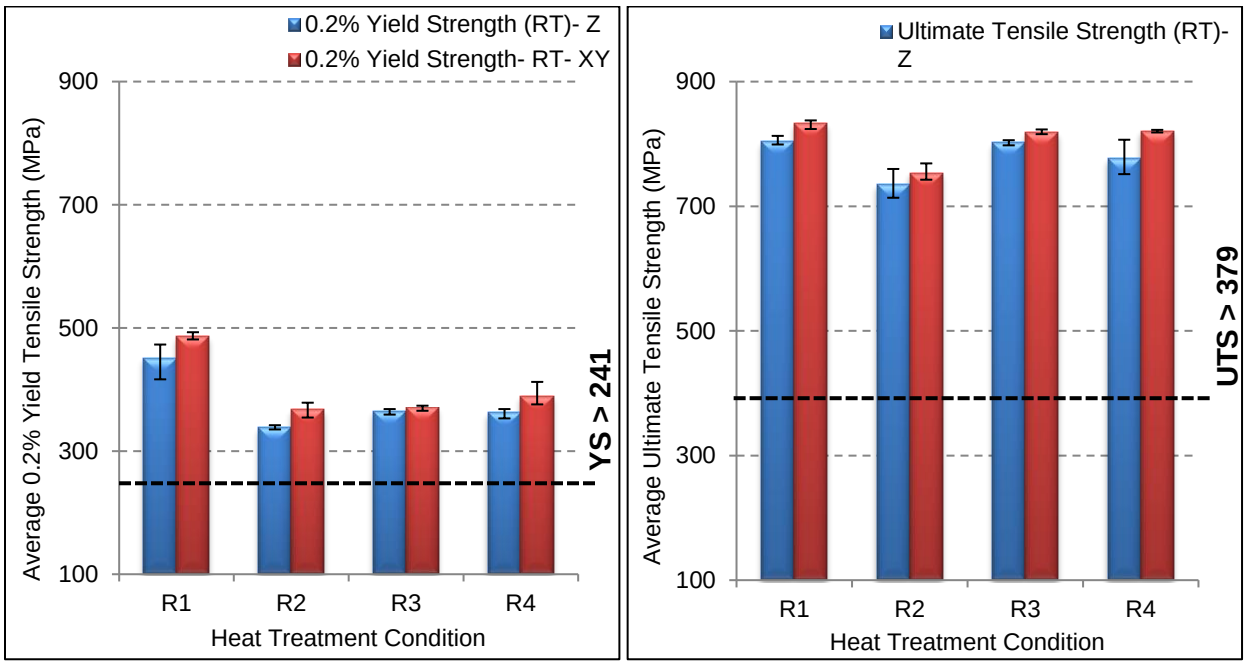

Figure 82. Average Room Temperature Tensile Strength of the S1-Fine Specimens Subjected to the Four HT Procedures

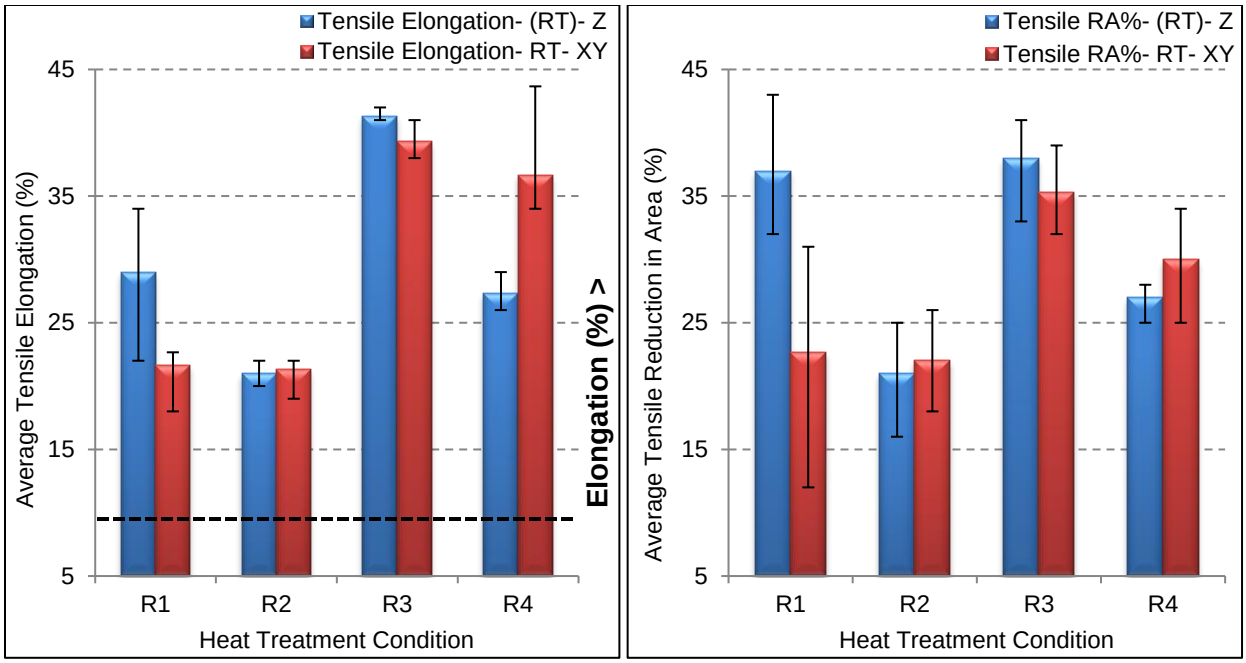

Figure 83. Average Room Temperature Tensile Elongation and RA of the S1-Fine Specimens Subjected to the Four HT Procedures

3.3.2.3 Elevated Temperature Tensile Test

The elevated temperature tensile test was conducted by EWI through a subcontractor. Three specimens were prepared and tested from each of the HT conditions and each of the orientations. The tests were conducted per ASTM E21, at 1500°F (815.5°C), after 20 minutes of soaking time. The results of the elevated temperature tensile test for the four HT conditions are summarized in Table 28.

Table 28. Summary of the Results of the Elevated Temperature Tensile Test for S1-F HT Specimens

Sample ID	Test Temp. (°C)	Test Temp. (°F)	Avg. YS		Avg. UTS		Avg. El. (%)	Avg. RA (%)	Failure Location
			MPa	ksi	MPa	ksi			
1-Z-4	815.5	1500	244.76	32.5	320.61	46.50	32.5	33.0	Middle 50%
1-Z-5	815.5	1500	248.21	35.5	324.05	47.00	35.5	35.0	Middle 50%
1-Z-6	815.5	1500	251.66	40.0	320.61	46.50	40.0	35.0	Middle 50%
1-XY-4	815.5	1500	265.45	18.5	334.40	48.50	18.5	12.5	Outside 2/3 gage
1-XY-5	815.5	1500	268.90	32.0	341.29	49.50	32.0	19.5	Outside 2/3 gage
1-XY-6	815.5	1500	251.66	19.5	337.84	49.00	19.5	14.5	Outside 2/3 gage
2-Z-4	815.5	1500	203.40	25.5	317.16	46.00	25.5	29.0	Middle 50%
2-Z-5	815.5	1500	199.95	27.0	310.26	45.00	27.0	22.0	Outside 2/3 gage
2-Z-6	815.5	1500	203.40	23.0	306.82	44.50	23.0	19.5	Middle 50%

Sample ID	Test Temp. (°C)	Test Temp. (°F)	Avg. YS		Avg. UTS		Avg. El. (%)	Avg. RA (%)	Failure Location
			MPa	ksi	MPa	ksi			
2-XY-4	815.5	1500	206.84	19.0	317.16	46.00	19.0	17.0	In gage punch
2-XY-5	815.5	1500	213.74	20.0	320.61	46.50	20.0	17.5	In gage punch
2-XY-6	815.5	1500	210.29	20.5	320.61	46.50	20.5	20.5	In gage punch
3-Z-4	815.5	1500	210.29	41.0	324.05	47.00	41.0	32.5	Middle 50%
3-Z-5	815.5	1500	220.63	35.0	327.50	47.50	35.0	29.5	Outside 2/3 gage
3-Z-6	815.5	1500	213.74	39.0	334.40	48.50	39.0	33.5	Middle 50%
3-XY-4	815.5	1500	213.74	33.0	334.40	48.50	33.0	29.0	In gage punch
3-XY-5	815.5	1500	213.74	31.0	341.29	49.50	31.0	29.0	In gage punch
3-XY-6	815.5	1500	210.29	35.0	327.50	47.50	35.0	29.5	Middle 50%
4-Z-4	815.5	1500	213.74	29.0	327.50	47.50	29.0	27.5	Outside 2/3 gage
4-Z-5	815.5	1500	220.63	26.5	327.50	47.50	26.5	25.5	Middle 50%
4-Z-6	815.5	1500	224.08	31.5	334.40	48.50	31.5	25.5	In gage punch
4-XY-4	815.5	1500	224.08	25.5	324.05	47.00	25.5	24.5	Middle 50%
4-XY-5	815.5	1500	206.84	33.5	330.95	48.00	33.5	29.0	Middle 50%
4-XY-6	815.5	1500	220.63	32.0	334.40	48.50	32.0	31.0	Middle 50%
Reference AMS5390 Investment Cast Ni Alloy X Specification Requirements			241.0	35.0	n/r	n/r	12.0	Not rated	

The minimum tensile requirements for investment cast Hastelloy X (per AMS 5390) are tabulated at the last row of Table 30. The average values of ultimate tensile strength and 0.2% yield strength in both XY and Z orientations were plotted in Figure 84. The average values of elongation (%) and RA (%) in both XY and Z orientations were plotted in Figure 85. The dashed lines on the plots indicate the minimum requirements per AMS 5390.

While all specimens showed a significantly higher ductility compared to the AMS 5390 requirements, the R1 HT was the only condition that passed the strength requirements of AMS 5390 at 1500°F. It should be noted that the AMS 5390 specification is for the investment cast Ni Alloy X material and the comparison to the AM material is only for reference.

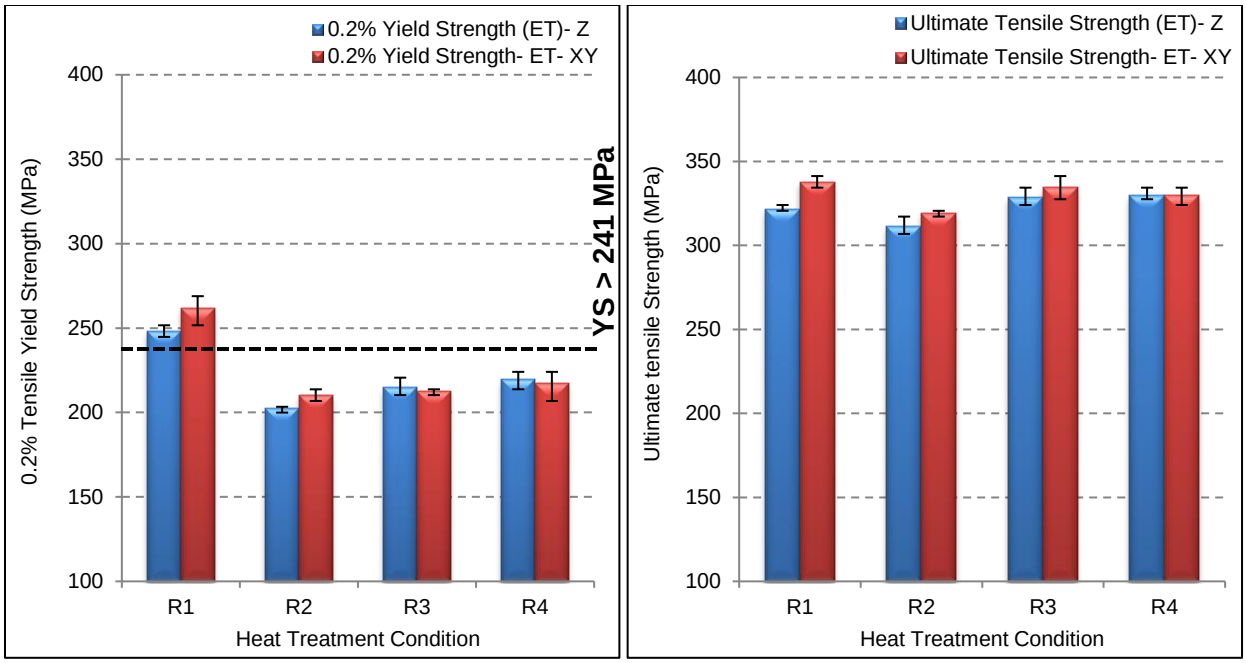

Figure 84. Average Elevated Temperature Tensile Strength of the S1-F Specimens Subjected to the Four HT Procedures

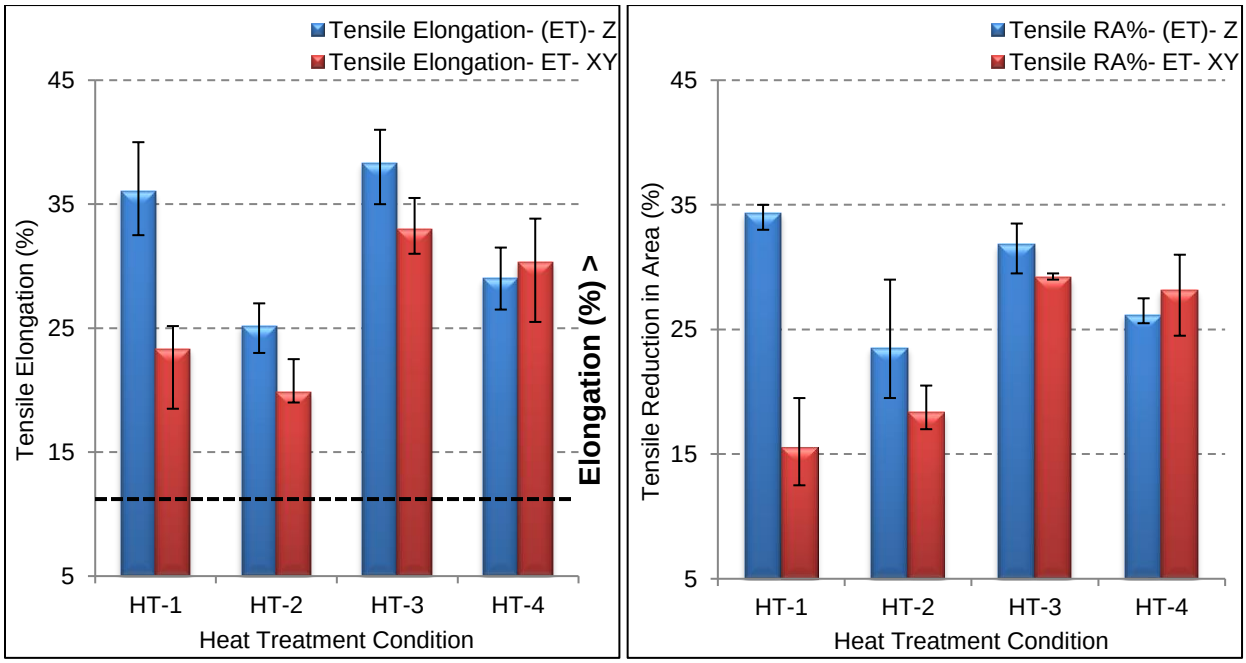

Figure 85. Average Elevated Temperature Tensile Elongation and RA of the S1-F Specimens Subjected to the Four HT Procedures

3.3.2.4 LCF Using Treatments R1-R4

The LCF test was conducted by Solar through Element Cincinnati. Three specimens with a gage diameter of 0.25 in. were tested per HT condition. A sinusoidal waveform was used at the

test temperature of 1000°F (537.8°C). Total strain range and stress ratio were set at 0.6% and -1, respectively. Figure 86 shows the average number of cycles prior to failure for the four HT conditions in both orientations. The HIP'd specimens showed a significantly higher fatigue life in both orientations, compared to solution- annealed samples. Although the R3 specimen showed the highest fatigue life, the largest standard deviation was also observed in this HT condition.

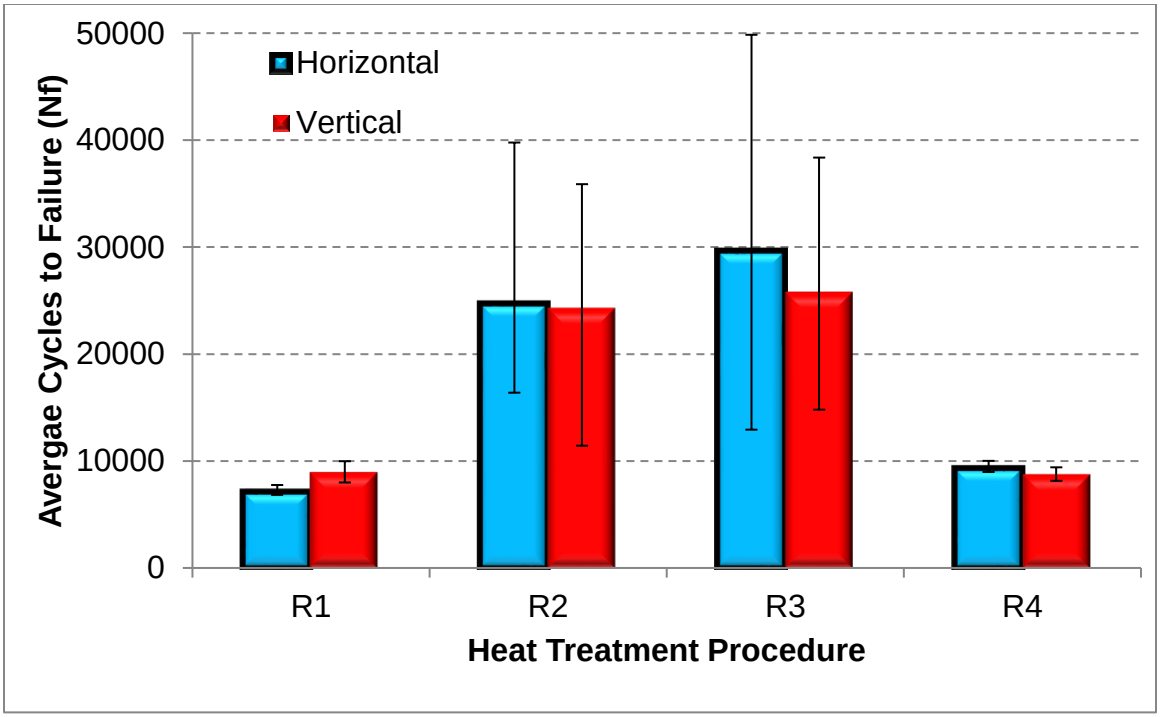

Figure 86. The LCF Test Results of the Four HT Conditions in both Horizontal and Vertical Orientations (HIP'd specimens showed a significantly higher fatigue life in both orientations, compared to solutions annealed samples)

During grain deformation, atomic layers attempt to slide up on each other in a shearing process, known as slip. If the slip displacement is small, the deformation will be reversible (HCF). If the slip is large enough, the plastic deformation will occur along the slip plane and the slip will become irreversible (LCF).

As fatigue cycles accumulate, the number and intensity of the slip bands increase and the microstructural damage concentrates on a few intense slip bands. The process continues until a persistent slip band forms. Eventually a fatigue crack will form along these slip bands. However, the fatigue crack formation occurs much faster in non-homogenous materials containing numerous microscopic discontinuities such as grain boundaries, microscopic pores, carbides, and other hard particles. These discontinuities inhibit slip and act as local stress concentrators based on their sizes and types. These features ultimately become fatigue crack initiation sites. After the initiation phase, crack tips propagate into the structure in response to each cyclic load, until they reach barriers such as precipitates or grain boundaries. Each additional cyclic load

results in the accumulation of stress behind a barrier. At some point, the accumulated stress is high enough to pass through the barrier.

Figure 87 shows the low magnification SEM images from the fracture surfaces of the HT Hastelloy X. Samples R1 and R4 showed multiple nucleation sites at subsurface and interior locations. These sites could explain the cup-cone feature on the fracture surface that is an indication of small scattering in LCF results shown in Figure 6. Conversely, samples R2 and R3 showed defined crack initiation sites at subsurface defects.

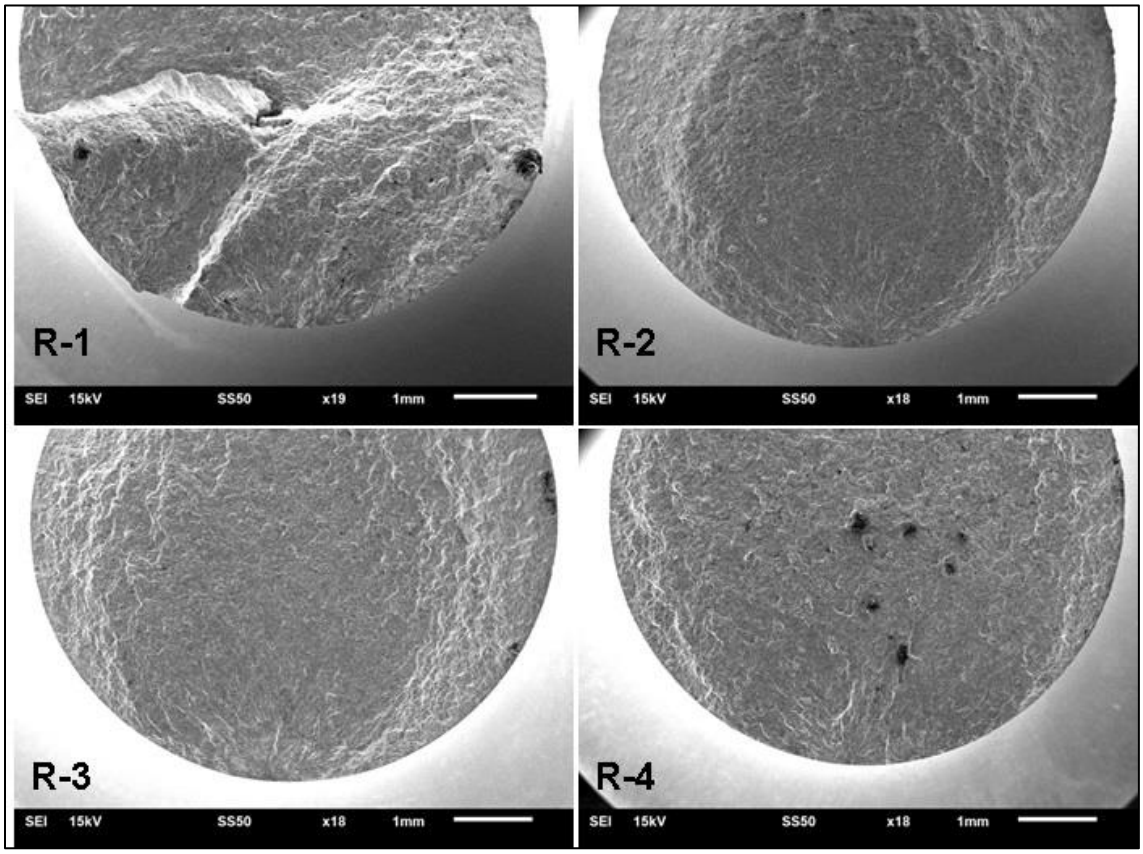

Figure 87. Low Magnification SEM Images of the Fracture Surfaces of the HT Hastelloy X

The HIP process succeeded in decreasing the number of internal defects, such as porosity and micro cracks, but the subsurface defects remained. The presence of such subsurface defects affected the test results and caused large scattering in the obtained results. Figure 88 shows higher magnification images of the crack initiation spots. The crack initiation in R1 and R4 is dominated by the presence of subsurface grains containing un-recrystallized dendritic structures. The dendrites are propagated in the perpendicular direction resulting in localized heterogeneity of plastic strain distribution. The presence of such un-recrystallized grains could again lead to the presence of multiple initiation sites.

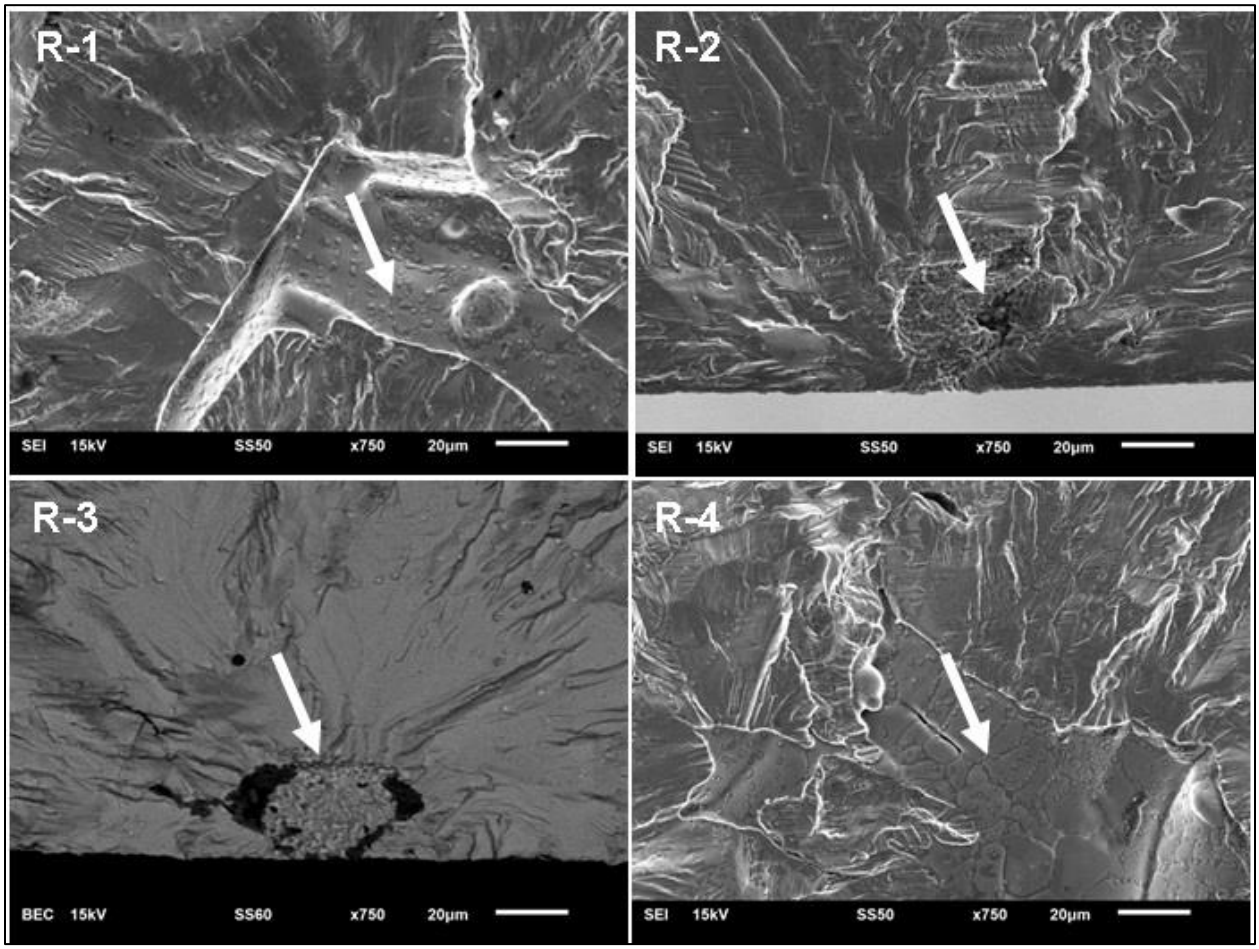

Figure 88. High Magnification SEM Images of the Fatigue Crack Initiation Spots of the HT Hastelloy X

The reduction of internal defects and the higher volume fraction of intergranular precipitates resulting from HIP leads to relatively longer fatigue life; however, the presence of randomly distributed, non-metallic inclusions caused large scattering in the results. Small LOF and solidification crack discontinuities are shown by the white arrows in Figure 88.

The application of HIP was effective in extending the fatigue life in R2 and R3, by closing LOFs and solidification cracking. The white arrow in sample R2 (Figure 88) shows a partially closed opening that was the crack initiation spot. In addition, a higher volume fraction of intragranular precipitates were present in samples R2 and R3. The relatively finer grain size and higher volume fraction of precipitates are the two major mechanisms that prohibited the crack growth under cyclic load and resulted in the longest fatigue life in samples R2 and R3.

A new crack initiation mechanism was observed in sample R3 (white arrow). Further analysis of the observed non-metallic inclusions in this sample showed indications of SiMo and intermetallic

inclusions such as AlMnMg. Figure 89 shows the EDS analysis. These non-metallic inclusions are indicated to be SiMo and intermetallic inclusions to be AlMnMg, as shown in Figure 89.

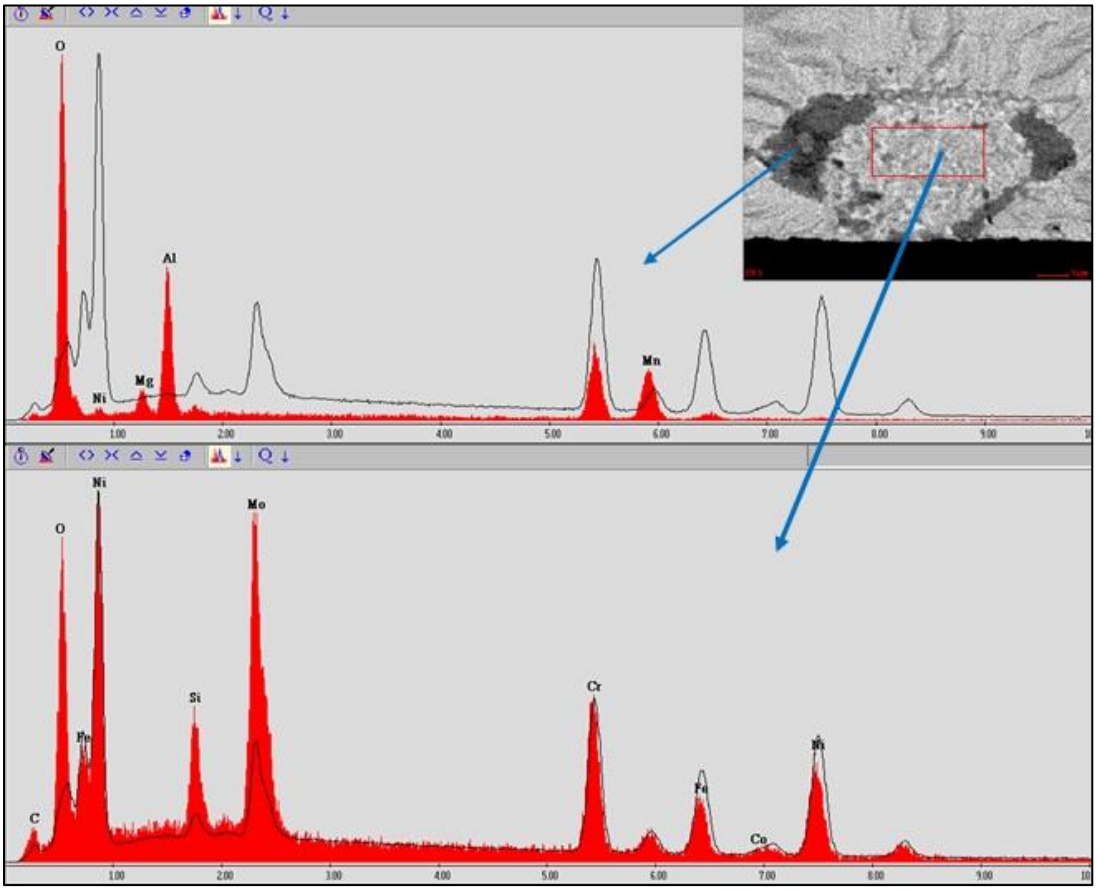

Figure 89. EDS of an Inclusion with a High Concentration of Si, Mo, Al, Mn, and Mg

3.3.2.5 Creep

The creep test was conducted at Solar through Joliet Metallurgical Laboratory. Three specimens per heat treatment were tested at 1500°F (815.5°C), under a 15-ksi stress. The results are summarized in Table 29. In general, the HIP'd specimens showed longer rupture time in both horizontal and vertical orientations.

Table 29. Creep Rupture Properties of AM Nickel Alloy X Material Produced after HT

Sample ID	Orientation	Test Temp. (°F)	Test Stress (ksi)	Hours to Rupture	Elongation at Rupture (%)
R1	Vertical	1500	15	34.20	9.27
R2	Vertical	1500	15	119.20	11.67
R3	Vertical	1500	15	40.00	8.30
R4	Vertical	1500	15	51.27	8.73
R1	Horizontal	1500	15	10.77	4.70
R2	Horizontal	1500	15	20.57	10.83
R3	Horizontal	1500	15	13.90	6.63
R4	Horizontal	1500	15	20.50	5.13
Reference AMS5390 Cast Ni Alloy X Specification Requirements	n/a	n/a	n/a	n/a	n/a
Reference AMS5536 Sheet/Strip/Plate Specification Requirements	n/a	1500	16	15-24	3-8
Reference AMS5754 Bar/Forging/Ring Specification Requirements	n/a	1500	15	24	10

The strain-time plots for the creep rupture testing of the four heat treated conditions are illustrated in Figure 90. It should be noted that these plots only present the initial 5% of the total strain, not the total strain at rupture. Creep deformation generally consists of three chronological stages, including primary, secondary, and tertiary creeps. The results of the creep rupture testing in this study were slightly different, as the primary fatigue was eliminated for most of the specimens.

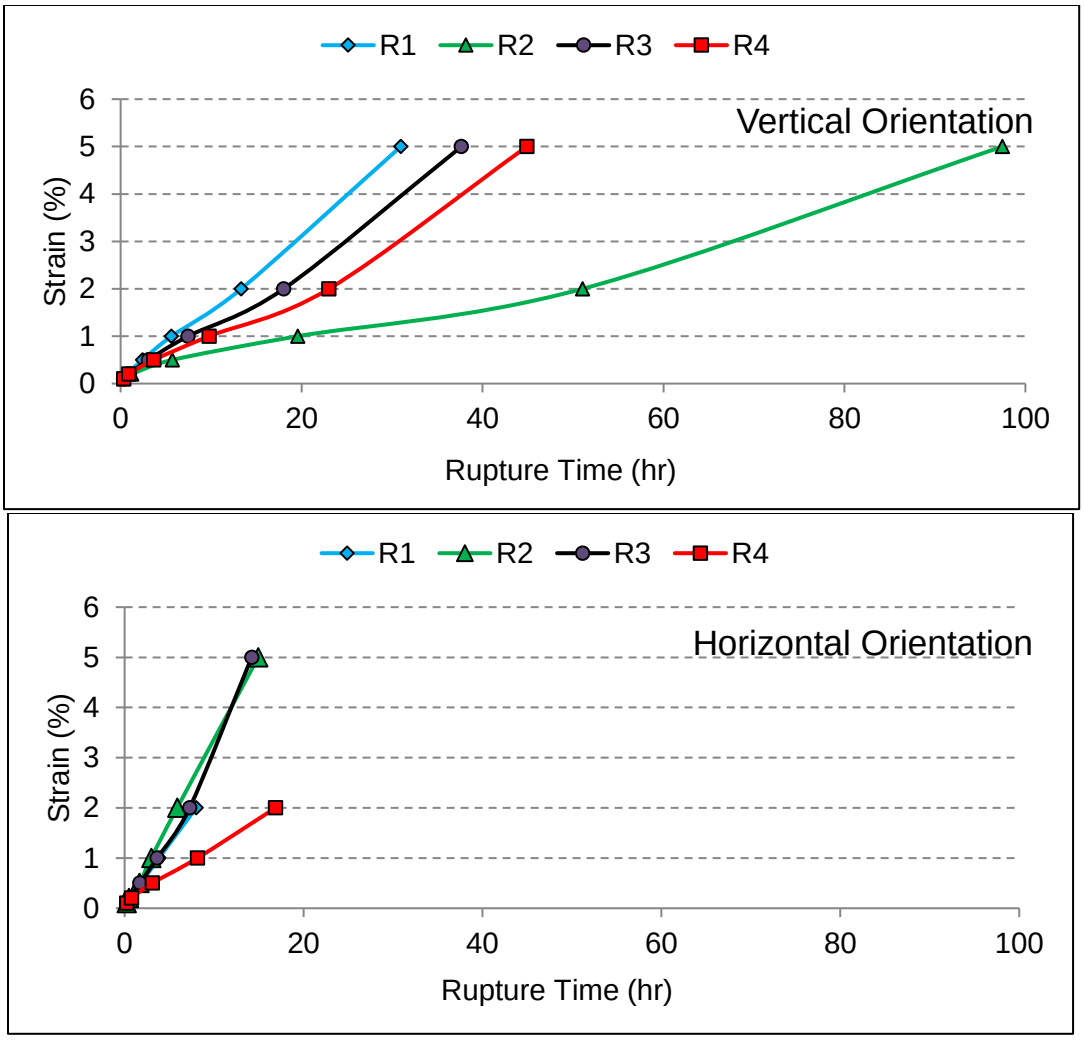

Figure 90. Strain-Time Plots of the HT Specimens in both Vertical (top) **and Horizontal** (bottom) **Orientations**

At high temperatures, the absence of primary creep is not uncommon, with secondary creep or, in extreme cases, tertiary creep following immediately upon loading. The HIP and R4 HT were the only two procedures that showed a slight indication of the primary creep. The accelerating strain in tertiary creep is caused by the reduction of load-bearing cross-sectional area, due to necking or cracking. In the case of AM materials, the presence of flaws such as LOF result in the reduction of cross-sectional area and consequently could accelerate creep failure.

A better presentation of the creep rupture time and elongation is illustrated in Figure 91 and Figure 92, respectively. Although both aforementioned HTs increased the creep rupture time, the influence of HIP is significantly higher along the buildup direction (vertical specimens).

Similarly, the vertical specimens showed a higher elongation under an elevated temperature creep load. Both R2 and R3 HT procedures resulted in high elongations in both orientations, compared to those of the solution annealed specimens.

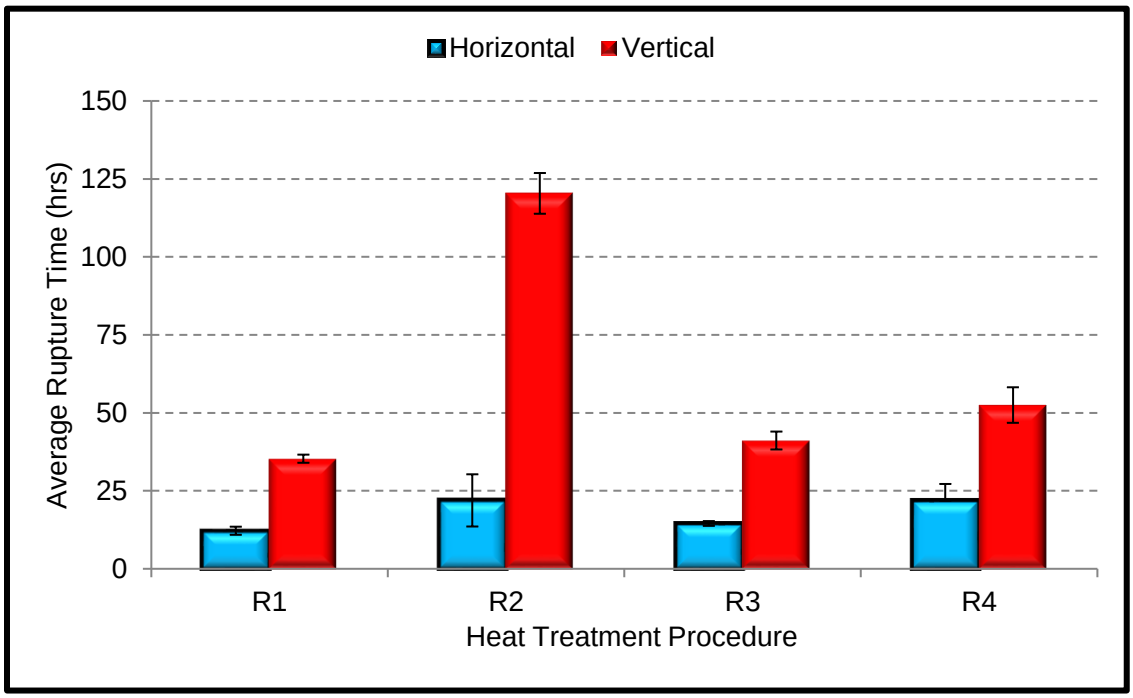

Figure 91. Average Creep Rupture Time of the HT Specimens in both Orientations

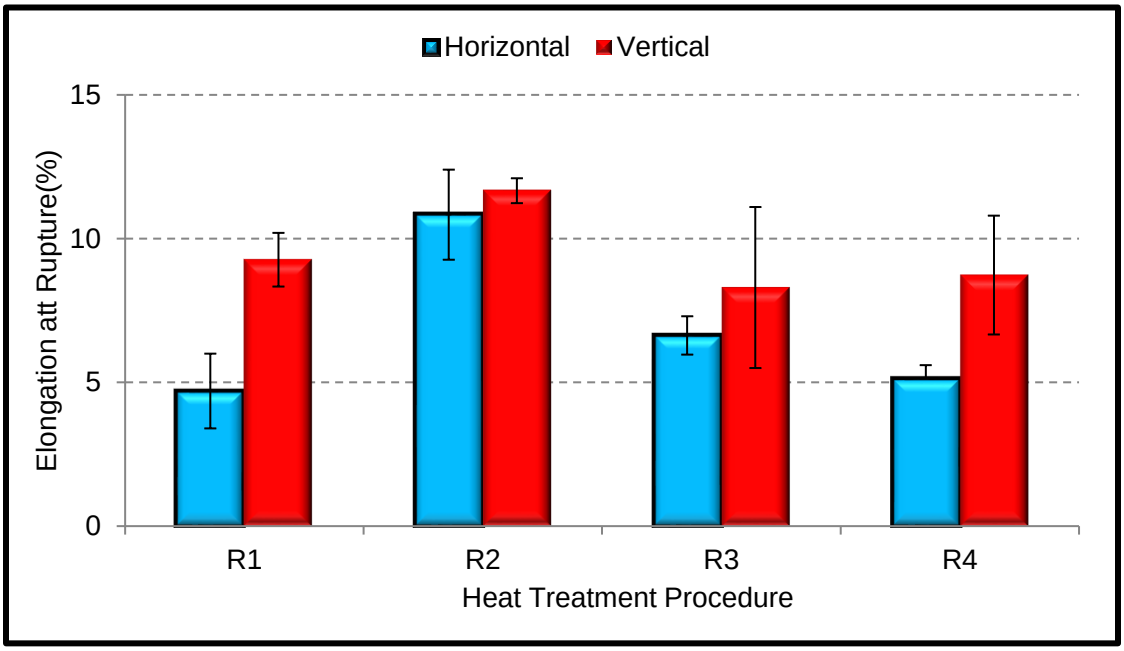

Figure 92. Average Elongation at Creep Rupture of the Heat-Treated Specimens in both Orientations

Figure 93 and Figure 94 show the SEM images from the fracture surfaces of the HT samples. There are four different regimes describing the creep mechanism for Ni-based super alloys:

- A dislocation climb regime that is characterized by the movement of dislocations through both the austenite matrix and the precipitates. This mechanism of creep rupture takes place at low temperatures (below approximately 1470°F).
- A deformation of austenite regime that is restricted to the austenite channels between the precipitates at low strains and temperatures ranging from 1470 to 1650°F. At this temperature range, the dislocations will have high mobility and instead of entering the precipitates, they slip across the matrix forming a sessile “Kear-Wilsdorf lock” configuration that cannot glide.
- A precipitate shearing regime that occurs in the temperature range of 1470 to 1650°F, but at higher strain. In this case, the dislocation density will be increased dramatically, initiating sufficient localized stresses to push the defects into the strengthening particles, causing them to shear as well.
- A dislocation pileup regime that could be observed at high temperatures (above approximately 1650°F). Above this temperature, the dislocations will start to pileup at the matrix/precipitate interfaces affecting the coherency and promote coarsening of precipitates.

Based on these definitions and the time of each creep stage, the creep mechanism that took place in this case is consistent with dislocation climb.

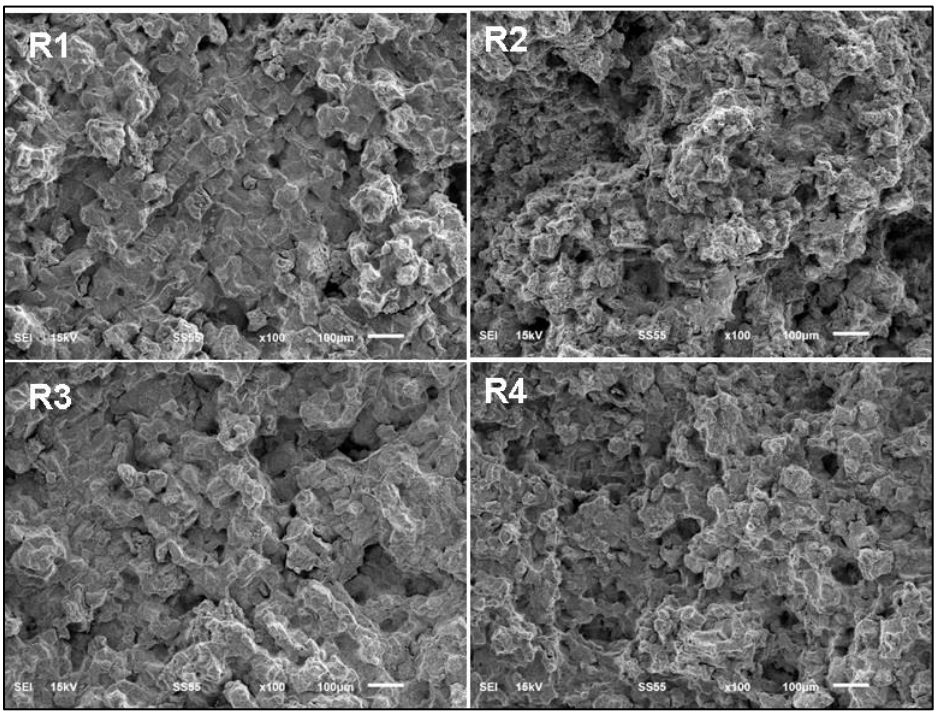

Figure 93. Low Magnification SEM Images of the Creep Fracture Surfaces of the Heat Treated Hastelloy X

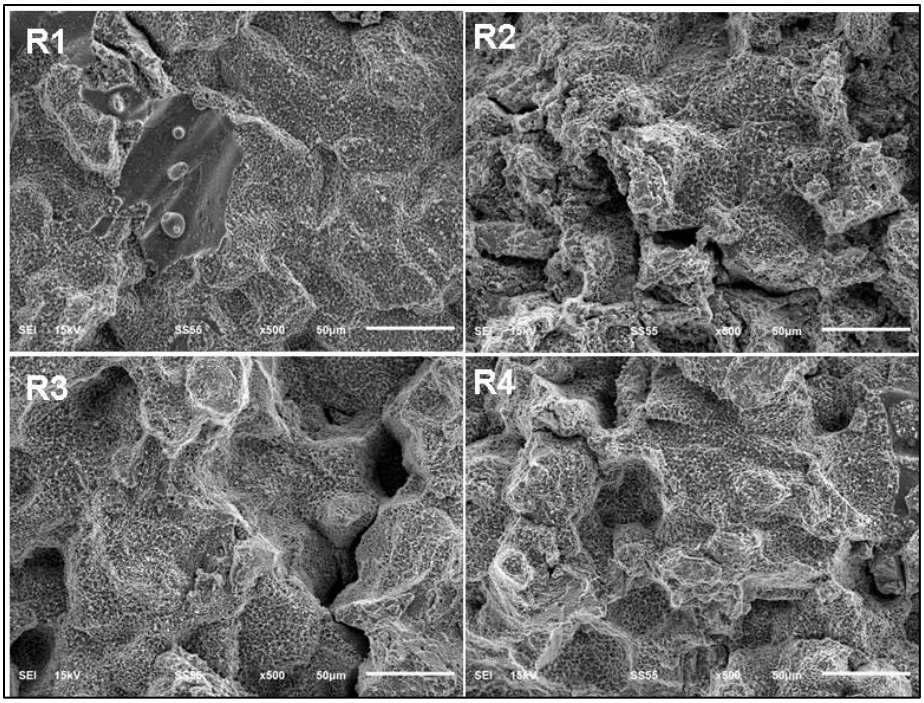

Figure 94. High Magnification SEM Images of the Creep Fracture Surfaces of the Heat Treated Hastelloy X

The fracture surfaces revealed different modes of failure. Intergranular creep fracture with micro-void formation at the grain boundary was observed. There is no clear fracture mode observed in these samples because:

- The test temperature lies within the equi-cohesive temperature (ECT) range of Ni-based super alloys. At the ECT range, the strength of the grain boundaries is equal to the strength of grains. Generally, if the test temperature is higher than the ECT range, the fracture mode will be an intergranular fracture and if the test temperature is lower than the ECT range, the fracture mode will be a transgranular fracture.
- Both strain rate and stress magnitude, also affect the fracture mode at certain grain sizes. At lower strain rates and stress magnitude, the tendency to form intergranular fractures increases. Increasing both increases the tendency for ductile fracture.
- In this test, the strain rate is low, while the magnitude of stress is high and that could lead to the observed mixed-fracture mode.

Intergranular creep fracture depends on the nucleation, growth, and subsequent linking of voids on grain boundaries to form two types of cavities: wedge-type cavities and isolated, rounded-type cavities.

The main feature of the failure mode is intergranular creep fracture with grain boundary micro-void formation. The observed difference in the time to rupture could be attributed to the difference in grain size and amount of precipitates between the tested samples. With the larger grain size, more dislocation will accumulate at the grain boundaries for a given applied stress,

leading to increases in the magnitude of localized stress concentrations and formation of micro voids.

3.3.3 Final Heat Treat Down-select and Mechanical Properties

Followed by the down-selection of one HT procedure (R2), three builds were produced at Solar, using S1-F powder, with each build containing four test walls. R2 (HIP) was selected based on an improvement to LCF and creep while maintaining decent ductility. R3 was also attractive, but the creep performance was poor.

Samples were all treated per HT scheme R2 – HIP'ing at 2150°F and 100 MPa (14.5 ksi) for four hours.

All test specimens were machined normal to the buildup direction. Table 30 contains the test conditions and number of samples produced to generate the test data curves of the AM Hastelloy X.

Table 30. Summary of the Test Plan Designed to Generate the Test Data Curves of Hastelloy X Produced with AM

Tensile Test		Low Cycle Fatigue Test				Creep Test	
Sample ID	Test Temp. (°F)	Sample ID	Test Temp. (°F)	R Ratio	$\Delta\varepsilon$	Sample ID	Test Temp. (°F)
T-1	RT	LCF-1	850	-1	0.6	2-1-1	1600
T-2	RT	LCF-2	850	-1	0.6	2-1-2	1600
T-3	RT	LCF-3	850	-1	0.6	2-1-3	1600
T-4	RT	LCF-4	850	-1	0.8	2-1-4	1600
T-5	RT	LCF-5	850	-1	0.8	2-1-5	1600
T-6	400	LCF-6	850	-1	1.0	2-2-1	1500
T-7	400	LCF-7	850	-1	1.0	2-2-2	1500
T-8	400	LCF-8	850	-1	2.0	2-2-3	1500
T-9	600	LCF-9	850	-1	2.0	2-2-4	1500
T-10	600	LCF-10	850	-1	2.0	2-2-5	1500
T-11	600	LCF-11	1000	-1	0.6	2-3-1	1400
T-12	800	LCF-12	1000	-1	0.6	2-3-2	1400
T-13	800	LCF-13	1000	-1	0.6	2-3-3	1400
T-14	800	LCF-14	1000	-1	0.8	2-3-4	1400
T-15	1000	LCF-15	1000	-1	0.8	2-3-5	1400
T-16	1000	LCF-16	1000	-1	1.0	2-4-1	1300

Tensile Test		Low Cycle Fatigue Test				Creep Test	
Sample ID	Test Temp. (°F)	Sample ID	Test Temp. (°F)	R Ratio	$\Delta\varepsilon$	Sample ID	Test Temp. (°F)
T-17	1000	LCF-17	1000	-1	1.0	2-4-2	1300
T-18	1200	LCF-18	1000	-1	2.0	2-4-3	1300
T-19	1200	LCF-19	1000	-1	2.0	2-4-4	1300
T-20	1200	LCF-20	1000	-1	2.0	2-4-5	1300
T-21	1500	---	---	---	---	---	---
T-22	1500	---	---	---	---	---	---
T-23	1500	---	---	---	---	---	---

RT: Room temperature

$\Delta\varepsilon$: Total strain range

3.3.3.1 Room Temperature Tensile Test – Mechanical Test Wall, HT R2

Five specimens were tested at room temperature. The results of the room temperature tensile test are summarized in Table 31. The minimum tensile requirements for investment cast Hastelloy X (per AMS 5390) are presented in the last row. The average values of ultimate tensile strength, 0.2% yield strength, elongation (%), and RA (%) were plotted in Figure 95. The dashed lines on the plots indicate the minimum requirements per AMS 5390. All specimens showed a significantly higher strength and ductility compared to the requirements of AMS 5390, with negligible standard deviations.

Table 31. Summary of the Results of the Room Temperature Tensile Test for the Horizontal S1-F Specimens after the HIP HT

Sample ID	Test Temp. (°C)	Test Temp. (°F)	Avg. YS		Avg. UTS		Avg. El. (%)	Avg. RA (%)	Failure Location
			MPa	ksi	MPa	ksi			
XY-1	23	73.4	389.55	56.50	744.63	108.00	39.0	44.0	Within gage length
XY-2	23	73.4	393.00	57.00	744.63	108.00	40.0	41.0	Within gage length
XY-3	23	73.4	409.55	59.40	738.43	107.10	39.0	44.0	Within gage length
XY-4	23	73.4	395.07	57.30	743.94	107.90	40.0	42.0	Within gage length
XY-5	23	73.4	395.76	57.40	743.94	107.90	40.0	41.0	Within gage length
Reference AMS5390 Investment Cast Ni Alloy X Specification Requirements			241.0	35.0	379.0	55.0	8.0	n/r*	

**n/r – not rated*

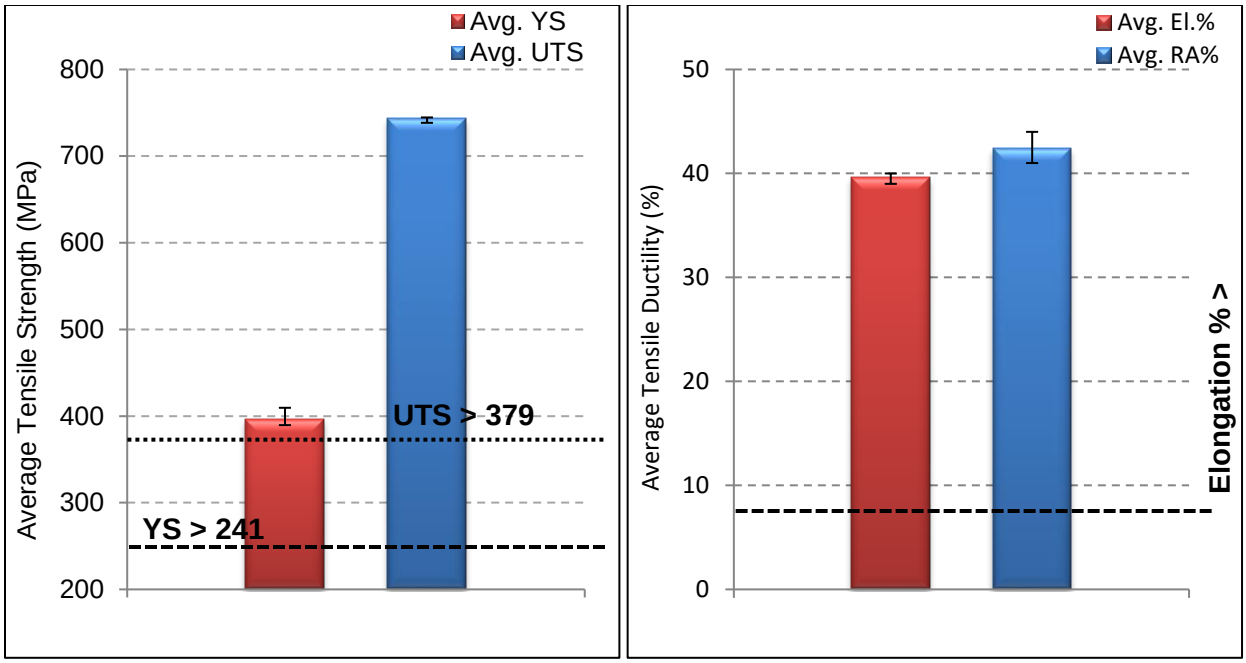

Figure 95. Average Room Temperature Tensile Strength and Ductility of the S1-F Specimens after the HIP HT

3.3.3.2 Elevated Temperature Tensile Tests – Mechanical Test Wall, HT R2

All test specimens were machined normal to the buildup direction (*a.k.a.* "horizontal" orientation or XY-plane). Table 32 contains the test conditions and number of samples produced to generate the test data curves of the AM Hastelloy X.

Table 32. Summary of the Test Plan Designed to Generate the Test Data Curves of HIP Heat Treated AM Hastelloy X Produced with L-PBF Process

Tensile Test					
Sample ID	**Test Temp. (°F)**	**Sample ID**	**Test Temp. (°F)**	**Sample ID**	**Test Temp. (°F)**
T-6	400	T-12	800	T-18	1200
T-7	400	T-13	800	T-19	1200
T-8	400	T-14	800	T-20	1200
T-9	600	T-15	1000	T-21	1500
T-10	600	T-16	1000	T-22	1500
T-11	600	T-17	1000	T-23	1500

The intent of this investigation was to develop an elevated-temperature tensile curve between room temperature and 1500°F, with properties measured in XY-planes. Three specimens were prepared and tested at each temperature. The test was conducted per ASTM E21, after 20

minutes of heat soaking time. The results of the elevated temperature tensile test are summarized in Table 33.

Table 33. Summary of the Results of the Room Temperature Tensile Test for the Horizontal S1-F AM Hastelloy X Specimens after the HIP HT

Sample ID	Test Temp. (°F)	Avg. YS (ksi)	Avg. UTS (ksi)	Avg. El. (%)	Avg. RA (%)	Failure Location
T-6	400	44.0	94.5	36.5	38.0	Within gage length
T-7	400	46.0	94.0	40.0	36.0	Within gage length
T-8	400	45.0	94.0	39.0	38.0	Within gage length
T-9	600	46.0	91.0	42.5	36.5	Within gage length
T-10	600	43.0	91.0	41.0	36.0	Within gage length
T-11	600	41.0	91.0	42.5	37.0	Within gage length
T-12	800	38.5	90.0	44.5	39.0	Within gage length
T-13	800	39.0	90.0	44.5	38.0	Within gage length
T-14	800	42.5	89.0	46.0	39.0	Within gage length
T-15	1000	38.5	87.5	45.5	40.5	Within gage length
T-16	1000	38.0	87.5	45.5	40.0	Within gage length
T-17	1000	35.5	88.0	47.0	38.0	Within gage length
T-18	1200	37.0	76.5	36.5	31.5	Within gage length
T-19	1200	38.0	77.0	33.0	29.5	Within gage length
T-20	1200	38.5	76.5	36.0	36.0	Within gage length
T-21	1500	31.5	43.5	24.0	22.5	Within gage length
T-22	1500	30.5	44.5	22.0	22.5	Within gage length
T-23	1500	31.5	44.5	21.0	22.5	Within gage length

Figure 96 shows the UTS and YS results and Figure 97 shows the elongation percentage and RA as a function of test temperature. Both UTS and YS measured values decrease with increasing temperature. However, after 1200°F, the UTS is dramatically decreased. The same behavior was observed in the elongation and RA.

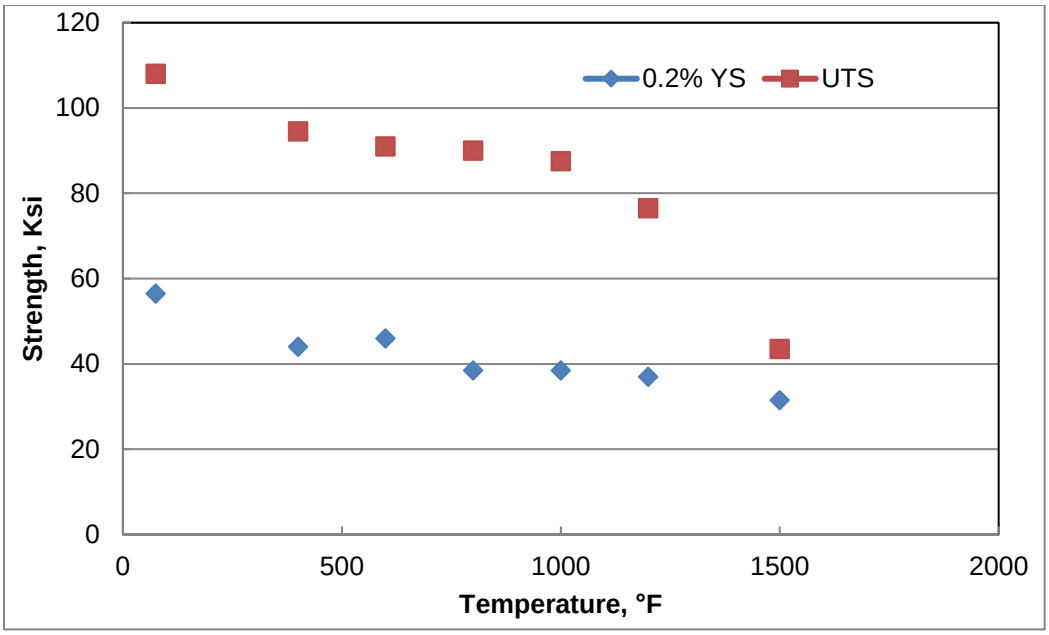

Figure 96. UTS and YS of HIP'd L-PBF AM Hastelloy X between RT and 1500°F (specimens tested were extracted from the horizontal build orientation)

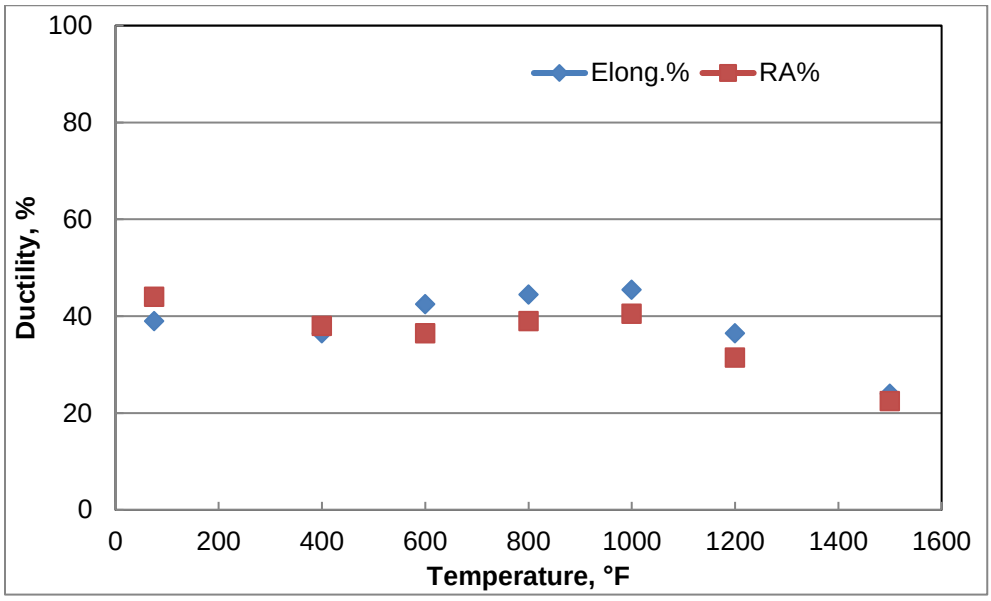

Figure 97. Elongation % and RA of HIP'd L-PBF AM Hastelloy X between RT and 1500°F (specimens tested were extracted from the horizontal build direction)

3.3.3.3 LCF Test – Mechanical Test Wall, HT R2

The LCF test was conducted by EWI through a subcontractor. Specimens with a gage diameter of 0.25 in. were tested using a sinusoidal waveform, at various temperatures and strain ranges. A fixed stress ratio of -1 was used for all specimens. The results of the LCF test for all

specimens are summarized in Table 34. It should be noted that the LCF test of the sample LCF-17 failed due to the specimen slipping at the beginning of the test.

Table 34. Summary of the Results of the Elevated Temperature LCF Test for the Horizontal S1-F Specimens after the HIP HT

Sample ID	Test Temp. (°F)	Total Strain Range (%)	Cycles to Failure	Note
LCF- 1	850	0.6	41,163	Fractured
LCF- 2	850	0.6	26,603	Fractured
LCF- 3	850	0.6	1,170,617	Runout
LCF- 4	850	0.8	8,296	Fractured
LCF- 5	850	0.8	11,598	Fractured
LCF- 6	850	1	5,154	Fractured
LCF- 7	850	1	3,952	Fractured
LCF- 8	850	2	909	Fractured
LCF- 9	850	2	769	Fractured
LCF-10	850	2	580	Fractured
LCF-11	1000	0.6	21,461	Fractured
LCF-12	1000	0.6	20,894	Fractured
LCF-13	1000	0.6	19,180	Fractured
LCF-14	1000	0.8	5,705	Fractured
LCF-15	1000	0.8	6,275	Fractured
LCF-16	1000	1	3,253	Fractured
LCF-17	1000	1	3	Slip at start/fractured
LCF-18	1000	2	623	Fractured
LCF-19	1000	2	472	Fractured
LCF-20	1000	2	62	Fractured

Figure 98 shows SN curve at two test temperatures of 850°F and 1000°F. Wide ranges of standard deviations were achieved at all temperatures and strain ranges. This could be related to the presence and uneven distribution of AM imperfections, such as lack of fusion in these samples. Further analysis of fracture surfaces will provide additional information to better analyze LCF results.

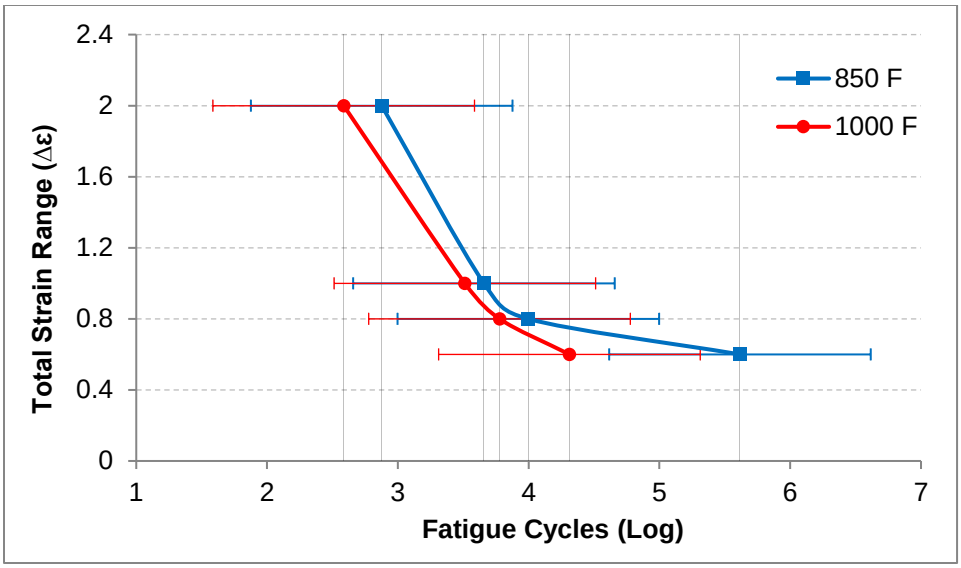

Figure 98. LCF Data Curve of Hastelloy X at Various Test Temperatures and Strain Ranges

3.3.3.4 Creep Test – Mechanical Test Wall, HT R2

The creep test was conducted at EWI through a subcontractor. Five specimens were tested at each of four temperatures, under various levels of stresses. The results of the creep test are summarized in Table 35. The creep rupture time is plotted against the stress at various temperatures in Figure 99.

The AMS 5390 standard does not provide any requirements for the elevated temperature creep properties of investment cast Hastelloy X. The other two standards including AMS 5536 and AMS 5754 only provided requirements for a stress of 15 ksi at 1500°F, which are not applicable to the DOE used in this study. The AMS standards are provided in the last row of Table 35 for reference.

Table 35. Summary of the Results of the Elevated Temperature Creep Test for the Horizontal S1-F AM Hastelloy X Specimens after the HIP HT

Sample ID	Test Temp. (°F)	Test Stress (ksi)	Test Stress (MPa)	Hours to Rupture	Elongation at Rupture (%)
2-1-1	1600	7.00	48.26	71.4	5.8
2-1-2	1600	5.40	37.23	98.3	3.4
2-1-3	1600	4.75	32.75	168.6	3.5
2-1-4	1600	4.30	29.65	363.5	5.9
2-1-5 *	1600	4.00	27.58	862.5	3.9
2-2-1	1500	11.50	79.29	81.3	5.9

Sample ID	Test Temp. (°F)	Test Stress (ksi)	Test Stress (MPa)	Hours to Rupture	Elongation at Rupture (%)
2-2-2	1500	9.50	65.50	106.8	4.9
2-2-3	1500	8.50	58.61	266.1	3.8
2-2-4	1500	7.90	54.47	326.9	4.5
2-2-5	1500	7.60	52.40	634.8	3.5
2-3-1	1400	18.00	124.11	64.7	11.3
2-3-2	1400	15.00	103.42	243.1	7.3
2-3-3	1400	13.80	95.15	306.1	5.9
2-3-4	1400	13.00	89.63	380.4	3.8
2-3-5 *	1400	12.30	84.81	524.4	4.8
2-4-1	1300	30.00	206.84	60.6	19.6
2-4-2	1300	25.00	172.37	156.8	17.1
2-4-3	1300	22.50	155.13	273.1	7.9
2-4-4	1300	20.50	141.34	438.7	6.2
2-4-5 *	1300	19.00	131.00	1230.8	9.5
Reference AMS5390 Cast Ni Alloy X Specification Requirements	n/a	n/a	n/a	n/a	n/a
Reference AMS5536 Sheet/Strip/Plate Specification Requirements	1500	16	110.3	15-24	3-8
Reference AMS5754 Bar/Forging/Ring Specification Requirements	1500	15	103.4	24	10

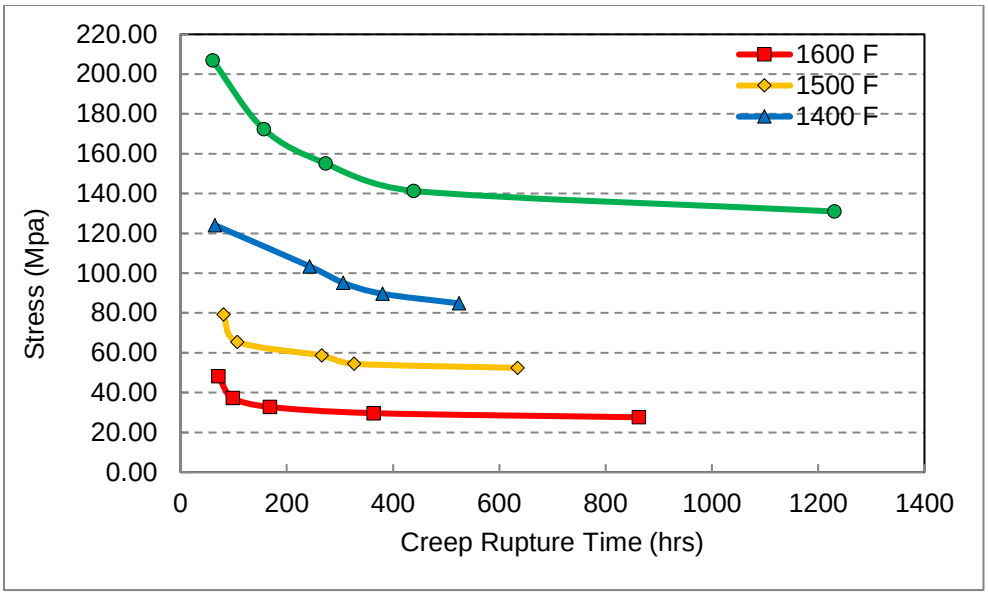

Figure 99. Creep Data Curve of Hastelloy X at Various Stresses and Test Temperatures

3.3.4 Post-process Finishing

Figure 100 shows specimens produced with the S1-F powder. Three inclination angles of 0, 20, and 45 degrees were used to reproduce the actual complexity of the fuel injector design.

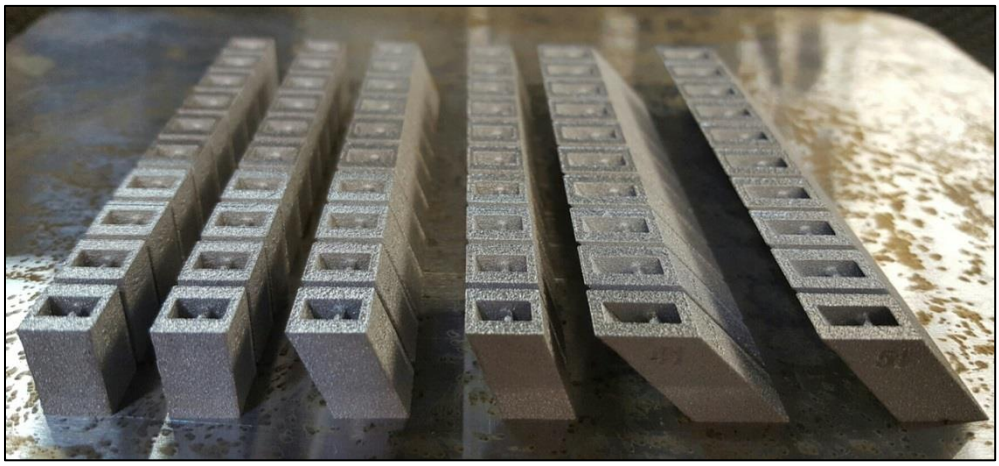

Figure 100. Specimens Produced with Three Inclination Angles of 0, 20, and 45 Degrees for the Analysis of Surface Roughness and Dimensional Accuracy

3.3.4.1 Post-process Finishing Techniques

After the measurement of the as-built surface roughness, the same specimens underwent different post-finishing techniques. It should be noted that the team expanded this effort to

include more post-finishing techniques by using newly developed techniques introduced to the AM industry. Following is a list of post-finishing techniques used in this study:

- Grit blasting
- Tumbling
- Extrude hone/abrasive flow machining
- Micro-machining process technology
- Hybrid DECI duo
- Electropolish

An important lesson learned during this activity was the competitive nature of the finishing methods technologies. Many parameters and specifics have been considered proprietary and were not reported to the team. The following contains a brief description of each technique and applied parameters, if available.

3.3.4.1.1 Grit Blast – Solar. Grit blasting is a relatively common finishing technique in a variety of industries. In this technique, an abrasive media is typically directed using compressed gas and impinges a component surface. The impacts smooth the surface and can introduce a layer of compression depending on the media and blasting parameters. Media types range from walnut shell particles to alumina and silicon carbide. For this work, the media was Barton HPA 80 Garnet), with an air pressure of 105 psi. It was done manually, in an industrial grit-blast cabinet.

3.3.4.1.2 Tumbling – Solar. Tumbling is another common surface finishing technique that rolls components in a horizontal barrel along with a dry media and, in some cases, a liquid or a chemical compound. Both the wet and dry versions of this technique employ gravity-driven impacts between components and media to smooth the surface of the components. As with grit blasting, a compression layer typically forms during this process. Unlike many of the techniques evaluated, this technique can process multiple parts simultaneously, with relatively low effort from an operator. The tumbling equipment used was a Burr King VibraKing Chamber Model 25. The media employed was Tristar (AC3s) Ceramic with a tumbling time of four hours.

3.3.4.1.3 Abrasive Machining – Extrude Hone/Abrasive Flow Machining (AFM). AFM utilizes abrasive particles suspended in a media, typically with the consistency of clay, but available over a large range of viscosity, to wear down and smooth surfaces. Custom tooling is typically designed for each component and the abrasive media is pushed through and around the various component features. Media flow rate, pressure, temperature, and viscosity, and abrasive particle size and particle concentration can be altered to tune the technique to a specific application. This process is commonly used for internal passages, but exterior surfaces are possible with appropriate tooling. One set of demonstration parts each was processed using

high and low media flow rates. The vendor report from this method was not included with the parts.

3.3.4.1.4 MMP Technology® – MicroTek Finishing. MMP Technology® is a proprietary technique described as a mechanical-physical-catalyst surface treatment. The technique utilizes a small-scale mechanical cutting process that takes place in a tank and is reported to selectively remove those frequent ranges of roughness identified by the customer. The process parameters and finishing details were not provided by the vendor and the process is considered proprietary.

3.3.4.1.5. Hybrid DECI Duo – PostProcess Technologies. The hybrid DECI Duo system utilizes a combination of user-operated and automated surface finishing methods to improve the surface finish of a component. Patent-pending “agitation algorithms” are used in combination with detergents and media in this system. Process parameters and finishing details were not provided, as the technique is considered proprietary.

3.3.4.1.6 Electropolish – Able Electropolishing. Electropolishing is accomplished by attaching the component to the positive side of a power source via a rack made of titanium, copper, or bronze. The rack and separate, negative side of the power source are immersed in a chemical bath. Metal ions leave the part and are drawn toward the cathode, effectively removing material and polishing the component surface. The process parameters and finishing details were not provided, as the technique is considered proprietary.

3.3.4.2 Execution of Post-processing Methods

The tumbling and grit blasting processes were carried out at Solar. Figure 101 shows the SEM images of the Hastelloy X coupons in the as-built condition and after being tumbled and grit blasted. The angle of inclination of the analyzed surfaces is indicated as: 0, 20, and 45 on the images. Tumbling removed some of the loose powder particles and smoothed the larger solidified beads, whereas, grit blasting not only removed all the powder particles from the surface, but also significantly changed the surface topology. EWI measured surface roughness of the three sets of samples.

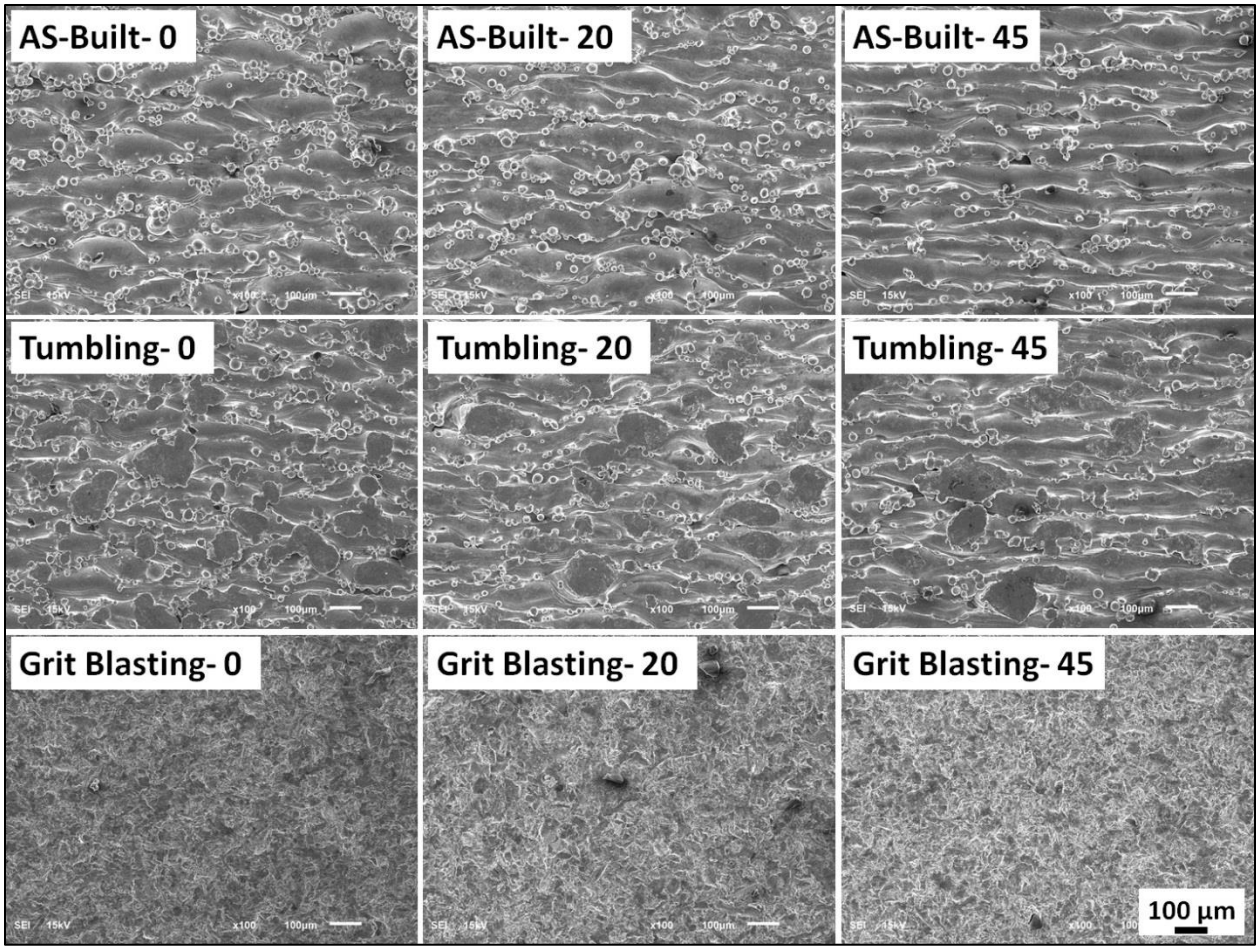

Figure 101. SEM Images of the Top Surface of Hastelloy X Specimens in the As-built Condition and after Being Tumbled and Grit Blasted

3.3.4.3 Finishing Method Performance – Roughness Measurements

Surface area roughness measurements were taken on the outer sides of the vertical demonstration parts (Figure 102).

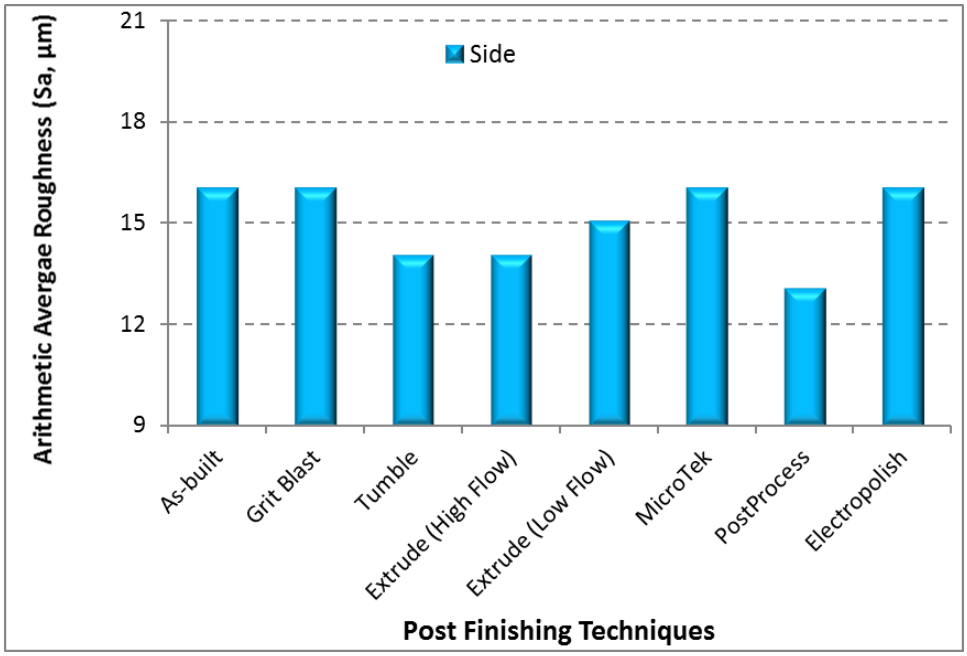

Figure 102. Side Wall Surface Roughness Comparison on Demonstration Parts Built Vertically

Surface roughness measurements were taken on the upward-facing and downward-facing walls for both the 20-degree off vertical and 45-degree off vertical demonstration parts. The results for the upward- and downward-facing surfaces are shown in Figure 103 and Figure 104, respectively.

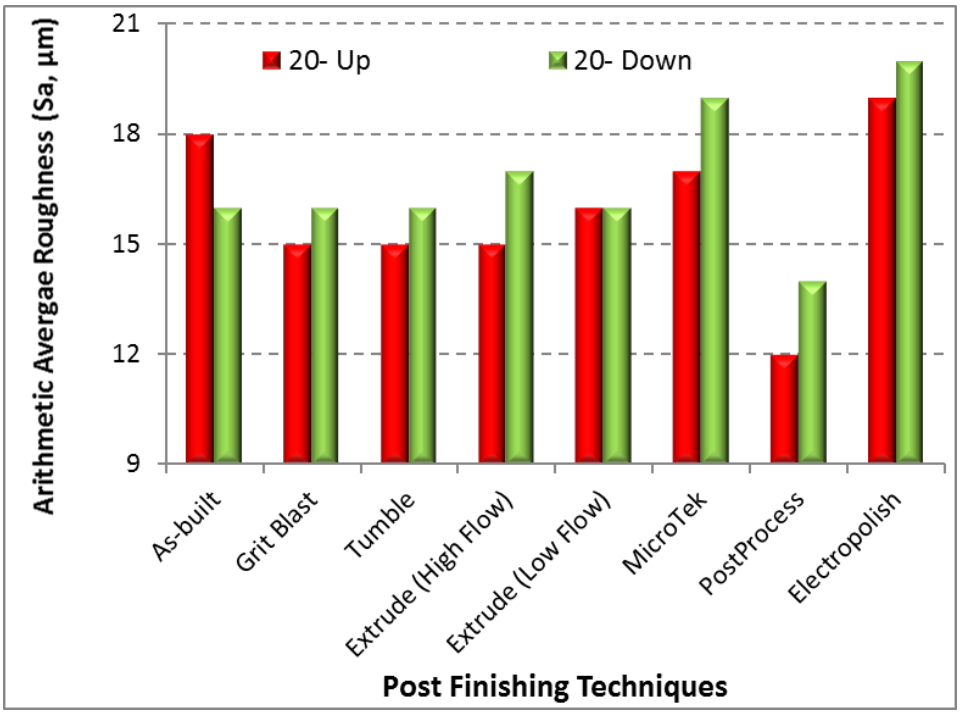

Figure 103. Exterior Upward- and Downward-facing Wall Surface Roughness for the 20-degree Demonstration Parts

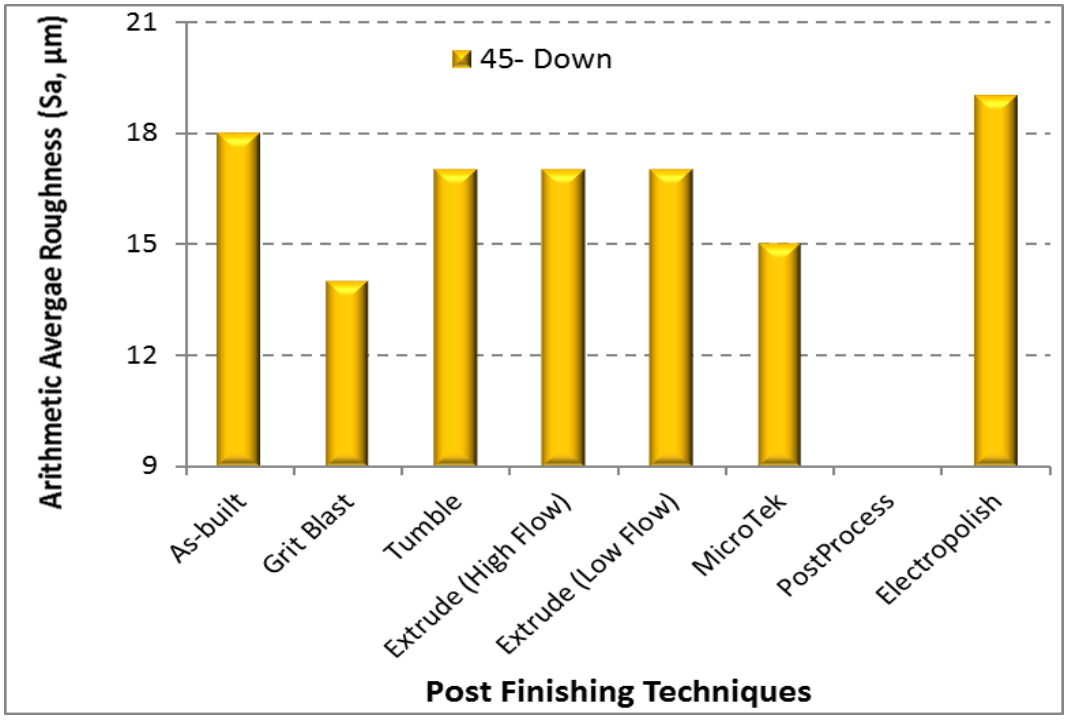

Figure 104. Exterior Upward- and Downward-facing Wall Surface Roughness for the 45-degree Demonstration Parts

3.3.4.4 Computed Tomography to Assess Post-finishing Methods

Surface roughness could only be measured on external surfaces, where a beam or probe could touch the surface. However, it was visually obvious that the different finishing techniques remove different levels of material from internal features. In addition, dimensional accuracy and appearance of sharp edges and corners were different in specimens processed by the aforementioned techniques. To better understand the influence of polishing techniques, computed tomography (CT) was conducted on the 45-degree demonstration parts. The average deviation from thickness is another tool that could be used to compare general performance of different finishing techniques. Figure 105 compares the thickness deviation distribution of the 45-degree samples processed using the tumbling and Hybrid DECI Duo techniques. Initial results show a higher level of material loss in the sample processed by the Hybrid DECI Duo technique.

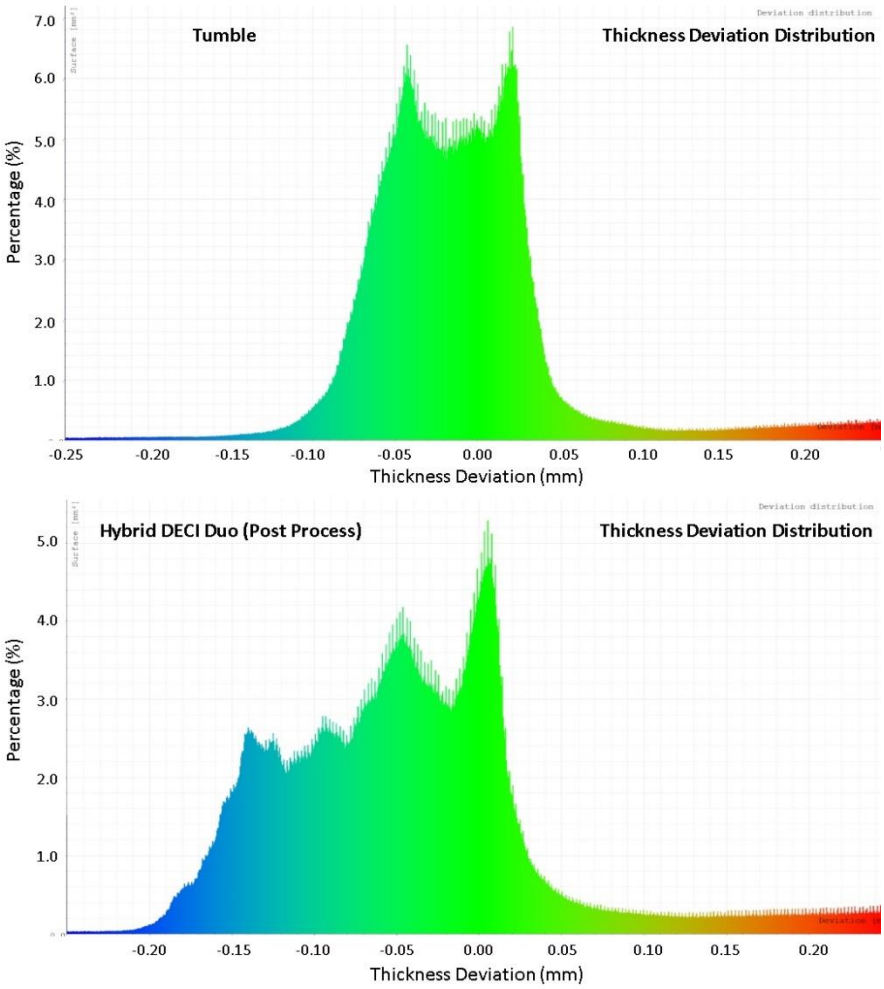

Figure 105. Comparison of the Thickness Deviation Distribution in 45-degree Coupon Processed by Tumbling and Hybrid DECI Duo

The comparison of 3D CAD with computed tomography (CT) reconstructed geometry can provide detailed information about thickness variation at different locations and could be used to investigate the influence of design on material loss. Figure 106 illustrates the comparison of the reconstructed CT geometry of a 45-degree sample with its original CAD design. The white arrow indicates a localized material loss at the beginning of the internal channel. Based on results, the interaction between the abrasive materials and the sample in this spot followed a different regime than the rest of the sample, which resulted in a significant material loss.

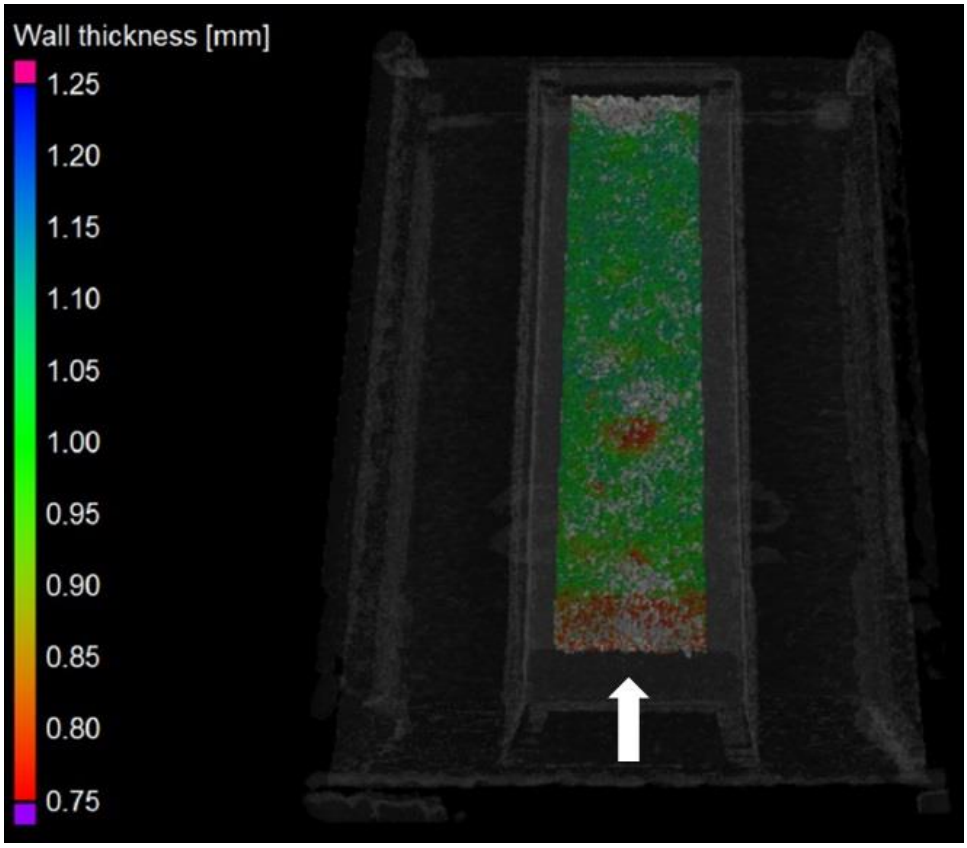

Figure 106. Comparison of the Reconstructed Geometry of a 45-degree Sample with Its 3D CAD

Results showed that a larger set of samples are needed to better understand the influence of each post-finishing technique on surface roughness. In some cases, measured surface roughness was higher than that of the as-built surface. For example, all the electropolished samples showed an *increase* in surface roughness compared to those of the as-built specimens. The lack of insight about parameters and settings used in each of the techniques made it more challenging to interpret results.

4.0 Summary and Conclusions

4.1 Summary

Solar teamed with EWI on a joint two-and-a-half-year project with the goal of developing a production L-PBF AM process capable of consistently producing AM Nickel Alloy X material suitable for high-temperature gas turbine engine fuel injector components. Throughout the execution of the four planned project tasks, key AM process risks were identified and corresponding process solutions were developed.

The process and properties knowledge gained through this project has played a significant role in Solar's journey from the AM prototyping paradigm to AM component serial production. Implementation of the process controls identified in this project have contributed to Solar's capability to produce high quality AM material for high-temperature gas turbine fuel injector components.

4.1.1 Task 2 – Powder Metal Input Stock

Four high nickel alloy powders from two suppliers were used to fabricate test articles using L-PBF. The four powder compositions fell within the commercially available Hastelloy X compositional range;[7] however, S1 produced a high silicon variant and S2 produced a low silicon variant. Each supplier produced a powder with a fine (5-38 µm) and coarse (16-45 µm) PSD. The AM articles from each powder were characterized for dimensional accuracy, void content, microstructure, and surface roughness. Test articles were also produced to measure tensile, LCF, and creep mechanical properties.

The PSD of the powders had no apparent effect on dimensional accuracy of the AM test articles; however, PSD did play a significant role in AM machine compatibility and mechanical properties. The powders with the finer PSD (5-38 µm) proved compatible with the ProX300 AM machine used for this program; whereas, the powders with the coarser PSD were not free flowing and incompatible with the subject AM machine powder seal design. The powders with the finer PSDs displayed superior LCF properties; however, the creep properties were reduced.

While both the high silicon and low silicon powder chemistry variants were capable of producing material with mechanical properties meeting published specifications for cast Hastelloy X, significant differences in mechanical properties and material microstructural quality were identified. The high silicon variant resulted in higher tensile yield strength; however, ductility was reduced. The AM material made with the low silicon variant displayed high levels of micro-cracking likely to be detrimental to long-term mechanical properties.

With these powder characteristic trade-offs identified, the high silicon alloy variant with a fine PSD was down-selected for additional process parameter development trials.

4.1.2 Task 3 – Process Parameters

The evaluation of the effects of global laser parameters (laser power, scan speed, hatch spacing) on geometric capability revealed that at slower speeds, the hole diameters were significantly reduced. Additional fine tuning of geometric settings would have been required to meet intended geometries, accordingly, the high-speed settings developed by the AM machine vendor were down-selected for subsequent HT optimization trials.

Multiple HT times, temperatures, and pressures were evaluated for their effects on mechanical properties. Significant improvements to material ductility and LCF properties were achieved with a HIP HT at 2150°F/4.5 hrs/14.5 ksi. Tensile and fatigue properties were similar in both the vertical (Z-Y) and horizontal (X-Y) directions.

Based on these results, the post-print HIP HT of 2150°F/4.5 hrs/14.5 ksi were down-selected for the subsequent task of generation of mechanical properties data curves.

4.1.3 Task 4 – AM Nickel Alloy X Material Properties

With these optimized process parameters identified, final test articles were produced for the generation of mechanical properties tensile, LCF, and creep curves suitable for design analysis activities. Tensile curves were generated from room temperature to 1500°F. LCF properties curves were generated at 850°F and 1000°F, under fully reversed conditions (HT R-1) from strain ranges of 0.6 to 2.0. Creep rupture properties curves were generated from 1300 to 1500°F with rupture times nominally ranging between 100 to 1000 hrs.

4.2 Material and Process Specifications

Based on the work foregoing, the materials and process specifications giving the best overall results are listed in Tables 36 through 38 below.

Table 36. Material Specification

Particle Size		
-5 µ	**-5 µ -> 38 µ**	**+38 µ**
<0.15%	>98.85	<1%

Table 37. Process Specification

HIPing	
Temp	1175°C (2150°F)
Pressure	100 MPa (14.5 ksi)
Time	4.5 hours

Table 38. Nominal Performance Specifications

Recommended Mechanical Performance*		
Property or Test [7,8]	**RT**	**870°C (1500°F)**
Tensile (X,Y) (MPa)	380	280 (min or as agreed)
Tensile (Z) (MPa)	380	280 (min or as agreed)
0.2% Yield (X,Y) (MPa)	240	200 (min or as agreed)
0.2% Yield (Z) (MPa)	240	200 (min or as agreed)
Elongation (X,Y) %	8	12 (or as arranged)
Elongation (Z) %	8	12 or (as arranged)
LCF (0.6% Strain)	15,000 cycles average	>2500 cycles average (538°C (1000°F))
Creep Rupture (105 MPa (15 ksi))		>18 hr
Rupture Elongation (105 MPa (15 ksi))		>4%

**After HIP at 1175°C (2150°F)/100 MPa (14.5 ksi)/4 hr.*

Additional guidelines for qualification on a case-by-case basis can be patterned after those found in ASTM F3056, Standard Specification for Nickel Alloy (UNS N06625) with Powder Bed Fusion[8] and in ASTM E8, Test Methods for Tension Testing of Metallic Materials[9].

4.3 Deliverables

The deliverables for this program were:

- Task 1 – Periodic reports prepared and submitted – Deliverable met.
- Task 2 – CMM data gathered from measurement of NIST Test Artifact builds – Deliverable met.
- Task 3 – Optimized post-process HT parameters, finalized L-PBF parameters for Task 4, selection of optimized process parameters for post-finishing – Deliverable met.
- Task 4 – Results of testing for tensile creep and LCF on final specimens – Deliverable met.
- Task 5 – Powder specification and process specification – Deliverable met.

5.0 References

1. Moylan, S., Slotwinski, J., Cooke, A., Jurrens, K., and Donmez, M.A., “An additive manufacturing test artifact”, *Journal of Research of the National Institute of Standards and Technology*, Vol. 119, pp. 429-459, 2014.
2. Zhao, K., Ma, K.H., and Low, L.H., “Improvement of creep rupture strength of a liquid metal cooling directionally solidified nickel-base superalloy by carbides”, *Journal of Alloy and Compounds*, Vol. 475, pp. 648-651, 2009.
3. Qin, Z.N., Guo, J.T., Yuan, C., Chen, C.L., Hou, J.S., and Ye, H.Q., “Decomposition of primary MC carbide and its effects on the fracture behaviors of a cast Ni-base superalloy”, *Material Science Engineering: A*, Vol. 485, pp.74-79, 2008.
4. Guanghai, B., Jinshan, L., Rui, H., Tiebang, Z., Hongchao, K., and Hengzhi, F., “Effect of thermal exposure on the stability of carbides in Ni-Cr-W based superalloy”, *Material Science Engineering: A*, Vol. 528, pp. 2339-2344, 2011.
5. Baek, E.R., Eung-Ryul, B., Park, S.-S., Sihotang, R.S., and Choi, S.K., “Heat treatment of the degraded Hastelloy-X for high cycle fatigue properties”, *In Proc. 9th International Conference on Fracture and Strength of Solid*, Jeju Island, Republic of Korea, Vol. 91, June 6-13, 2013.
6. Chang, K., Lai, H., and J. Hwang, “Existence of Laves phase in Nb-hardened superalloys – Superalloys 718,625,706 and various derivatives”, Edited by E.A. Loria, *The Minerals, Metals & Materials Society*, pp. 683 – 694, 1994.
7. AMS 5390, Nickel Alloy, Corrosion and Heat Resistant, Investment Castings, 47.5Ni, 22Cr, 1.5Co, 9Mo, 0.6W, 18.5Fe (N-12mv) As-Cast.
8. ASTM F3056, Standard Specification for Nickel Alloy (UNS N06625) with Powder Bed Fusion.
9. ASTM E8, Test Methods for Tension Testing of Metallic Materials.